UNIVERSITÀ
degli STUDI
di CATANIA

Dipartimento
di Fisica
e Astronomia
"Ettore Majorana"

PhD programme in physics

Dr. Giuseppe Emanuele Capuano

Diagnostics of the solar corona expansion through Metis coronagraph observations

PhD thesis

Supervisors:
Prof. Francesca Zuccarello
Dr. Daniele Spadaro

---

academic year 2021/2022

Contents

Summary

This work aims to give a contribution to the investigation of the solar wind plasma acceleration mechanisms. To reach this purpose, the main coronal diagnostics techniques are described, with the aim to estimate physical parameters such as the coronal electron density distribution and the solar wind outflow velocity. These diagnostics techniques are applied to observational data, such as those obtained with the instruments onboard the SOHO and STEREO spacecraft, and, currently, to high resolution data provided by the Metis coronagraph, onboard the Solar Orbiter spacecraft. Metis is able to perform observations of the solar corona until a minimum distance of 0.28 au, providing detailed images important for a deep investigation of the solar wind sources, highlighting their fine structure, as well as of the plasma acceleration mechanisms. The results reported in this PhD thesis take into account the Metis first light detailed analysis, performed to infer the electron density and the outflow velocity of the expanding corona at relatively low heliocentric distances, clearly discriminating the separation between fast and slow solar wind regimes and linking the plasma properties with the coronal magnetic field configuration. The results coming from the first quadrature between Solar Orbiter and the Parker Solar Probe spacecraft allow to extend the detailed investigation of the aforementioned parameters from about 3.5 $R_\odot$ to 22 $R_\odot$, also inferring other fundamental parameters (such as the radial component of the magnetic field and the plasma flux energy). Finally, the results obtained from the analysis of the first CME observed with Metis, complemented with observations performed with the STEREO-A/COR 2, SOHO/LASCO-C2, Solar Orbiter/EUI-FSI, and STEREO-A/EUVI instruments, provide the detailed structure of the transient event and information relative to its kinematics and its source region. The results here

reported are important in view of space weather applications, concerning the development of forecasting tools for severe events potentially dangerous for the human activity and safety.

Chapter 1

The heliosphere and its origin

Space plasma that fills the heliosphere originates mainly from a continuous flow coming from the Sun. Such a plasma propagates with increasing velocities until it reaches the local interstellar medium (ISM) at distances of tens of billions of kilometers, where the pressure achieves values comparable with those typical of the ISM. This continuous plasma flow takes the name of "solar wind", and the factors that contribute to its origin are currently debated, as well as whether the solar magnetic field plays a fundamental role in the acceleration and propagation of the solar wind. In the following sections, the main points concerning the solar atmosphere and how the solar magnetic field contributes to its dynamics will be described.

1.1 The solar atmosphere and its environment

The structure and configuration of the solar atmosphere is regulated by the solar magnetic field and by its activity cycle. It has been observed that the magnetic field changes from simple configurations (minima phase of activity), in which the magnetic field assumes a typical dipole structure, to more complex configurations (maximum phase of activity). The time interval between a minimum of activity and the successive is 11 years, where an inversion of polarity can be observed. This means that the magnetic polarity cycle has a duration of 22 years, that is the time range between the formation of two solar magnetic configurations that show

the same polarity at the minimum. The magnetic evolution is underlined by the presence of atmospheric structures and the occurrence of energetic phenomena. The increase of the temperature with altitude in the solar atmosphere, as it will be seen in the following, is an indicator of the presence of non-thermal mechanisms which contribute to the solar atmosphere heating, strictly linked with the solar magnetic activity and to the inner atmosphere dynamics.

The solar atmosphere is composed of three main regions: the photosphere, the chromosphere, and the corona. The photosphere is the inner part of the atmosphere that can be observed. In this region the mean free path of the photons increases remarkably, so that the radiation starts to be free to travel in the surrounding space. The photosphere has an effective temperature of about 5700 K and a mean density of the order of 10^{20} cm^{-3}. The photospheric magnetic field manifestation is centered on the sunspots. The duration of sunspots is of the order of some weeks, and these structures are grouped to form active regions (ARs). Their quantification can be used as a proxy for the determination of the magnetic activity phase: the increase of the Sun activity can be highlighted by the more frequent appearance of ARs, while the solar minimum phase is characterised almost by the absence of these features.

The chromosphere, above the photosphere, is characterised by lower density, less visible emission with respect to the photosphere, and higher temperatures (10^4 - 10^5 K). In the chromosphere, plages, spicules, and prominences can be observed, and their presence and evolution is dictated by the solar magnetic field. In particular, the plages show higher temperatures and luminosity, and are the chromospheric manifestation of the intense magnetic fields emerging from the ARs. The spicules extend for thousands of kilometers and are sustained by the local magnetic field that emerges from the photospheric granulation. They have a duration of some minutes and show higher values of density with respect to the surrounding plasma. Prominences are arch-like structures visible on the limb of the solar disc (called "filaments" if they are observed on the disc), which form on the neutral line that separates two regions with opposite magnetic polarity, and show the presence of relatively cold gas ($\approx 10^4$ K) and high density values (10^{11} - 10^{12} cm^{-3}). The transition region, a thin layer between the chromosphere and the solar corona, shows a remark-

able gradient of temperature, which ranges from about 10^4 K to about 10^6 K. High energy events can be observed in the inner atmosphere (flares), the occurrence of which is due to local magnetic field reconfigurations, caused by magnetic reconnection phenomena mainly related to instabilities and magnetic flux emergences. The high amount of magnetic energy released during these events is converted into particle energy, electromagnetic radiation and plasma heating.

The solar corona extends through the interplanetary space, as far as the ISM zone is reached, and shows density values of $10^8 - 10^9$ cm^{-3} at low heliocentric distances, decreasing moving away from the Sun, and temperatures over 10^6 K. The coronal emission is almost absent in correspondence of the coronal holes (CHs), while the emission is particularly high in the bright regions, where loop-like structures underlining the emergence of the magnetic field over the ARs can be observed. The magnetic field configuration in the extended corona is observed in the streamers, which are quasi-stationary large-scale structures that show loop-like magnetic field features, and in open and almost radial configurations characterising the CHs (see Fig. 1.1). The streamers can be separated in "helmet" streamers, which separate CHs of opposite polarity, and unipolar "pseudo"-streamers, which separate CHs with the same polarity. During the minimum phase of solar activity, the streamers are located at low and quasi-equatorial latitudes, as the evidence of a three-dimensional (3D) structure called "streamer belt", while the CHs are observed in the polar regions. In this case, there is a dominant quasi-steady fast solar wind that originates in open-field polar CHs, and a variable, slow solar wind originating around the equatorial streamer belt (McComas et al., 1998, 2008). When the solar activity increases and evolves toward the maximum of solar cycle, this configuration of the corona and solar wind breaks down. Thus, polar holes shrink, and the solar magnetic field becomes tangled due to magnetic flux emergence underlined by the presence of ARs, equatorial CHs, and coronal streamers at higher latitudes (streamer belt widening). In this case, a mixture of fast and slow wind appears at all latitudes (see McComas et al., 2003, and Fig. 2.1). The solar wind features will be described in Chapter 2.

Over a heliocentric distance of about 2.5 $R_\odot$, it is possible to define the so-called "source surface", over which the kinetic plasma pressure

dominates over the magnetic pressure and, then, the coronal magnetic field approaches a radial open-field configuration at all latitudes, with a "frozen-in" behaviour of the expanding plasma. The sprawling surface where the polarity of the Sun's extended (heliospheric) magnetic field (HMF) changes from north to south identifies the heliospheric current sheet (HCS, see Fig. 1.2).

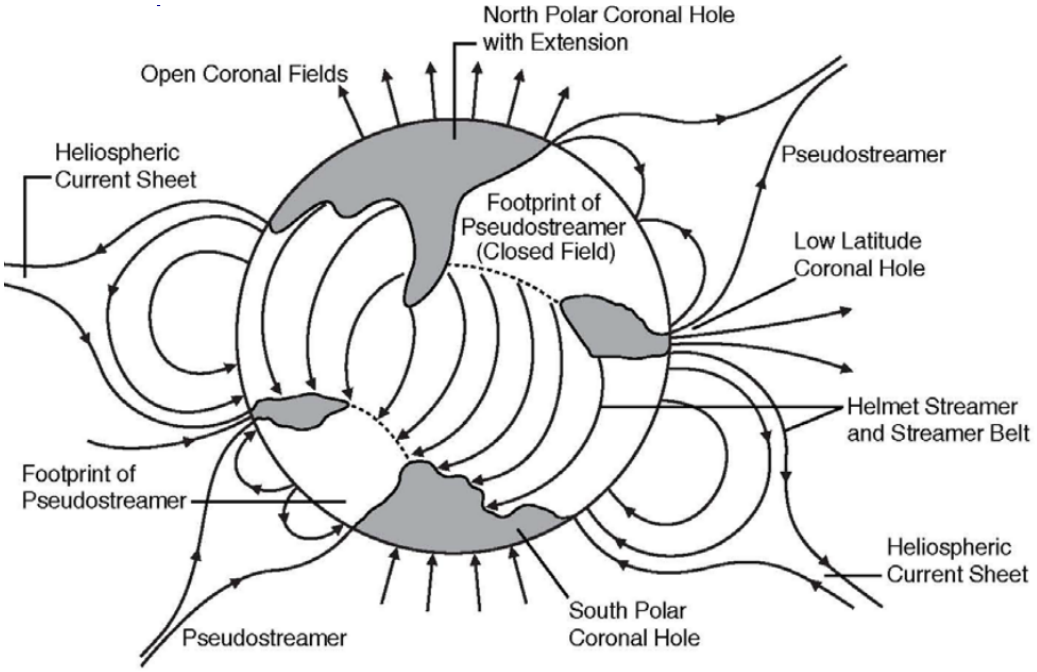

Figure 1.1: Scheme of the configuration of the coronal magnetic field, highlighted by helmet and unipolar pseudo-streamers, and by coronal hole open magnetic field.

The expected configuration of the HMF has been proposed by Parker (1958). Let consider a radially symmetric HMF. If the Sun did not rotate, the magnetic field configuration would be radial, with a radial coronal expansion. However, the rotation of the Sun has to be taken into account. Then, assuming the radial velocity component of the flowing plasma v_r to be equal to a constant value, the velocity azimuthal (v_ϕ) and latitudinal (v_θ) components in a system rotating with the Sun are done by:

$$v_\phi = -\omega r \sin\theta$$

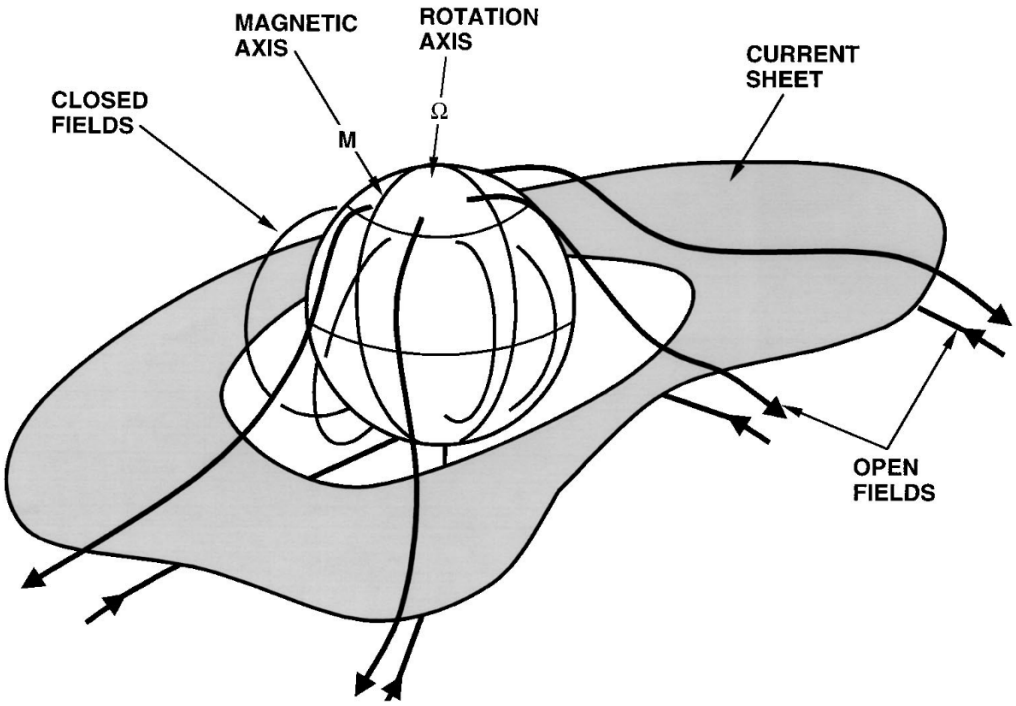

Figure 1.2: Scheme of the HCS. The shaded surface separates regions with opposite polarity. See Smith (2001)

$$v_\theta = 0$$

where ω is the mean angular velocity module, r and ϕ are the radial and azimuthal coordinates, and θ is the colatitude (see Fig. 1.3). The $\sin\theta$ term takes into account the differential rotation of the Sun. In fact, at the equator the Sun rotates with an angular velocity larger than that measured going toward the polar regions, and the aforementioned term considers the increasing speed, as a function of the colatitude θ, of a given source area which remains fixed in the rotating reference system. The path followed by the plasma from such a source area is returned by the following differential equation:

$$\frac{1}{r}\frac{dr}{d\phi} = \frac{v_r}{-\omega r \sin\theta} = \frac{v_r}{v_\phi} = \frac{B_r(r,\phi,\theta)}{B_\phi(r,\phi,\theta)} \tag{1.1}$$

with θ = constant. Therefore, in the reference system corotating with

the Sun, the plasma streamlines and the frozen magnetic field lines are coincident, and the so-called "Archimedes-Parker spiral" for the magnetic field is generated. Finally, the Maxwell equation $\nabla \cdot \mathbf{B} = 0$ leads to the following expression for the magnetic field:

$$B_r(r, \phi, \theta) = B_r(r_0, \phi_0, \theta) \left(\frac{r_0}{r} \right)^2$$

$$B_\phi(r, \phi, \theta) = -B_r(r_0, \phi_0, \theta) \frac{\omega r_0^2}{r v_r} \sin\theta$$

$$B_\theta(r, \phi, \theta) = 0$$

In Fig. 1.4 the Archimedes-Parker spiral is traced for three different latitude values: 0°, 30°, 60°.

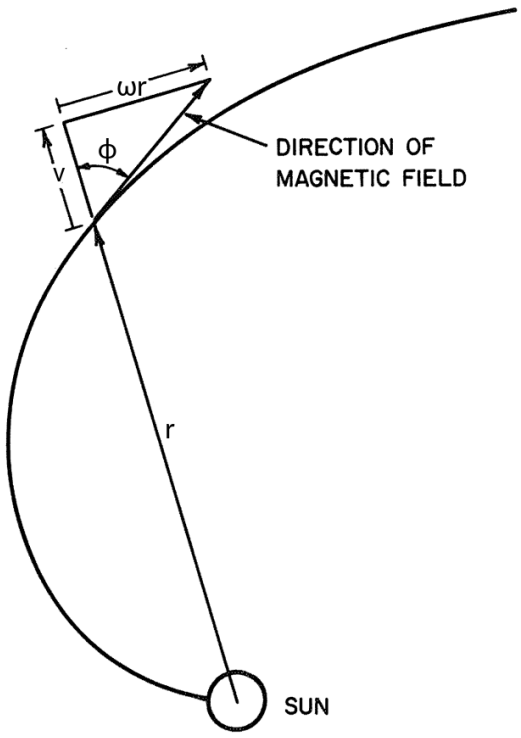

Figure 1.3: Configuration of the magnetic field lines in the Parker model. The radial velocity v_r=V is assumed to be constant. See Hundhausen (1972).

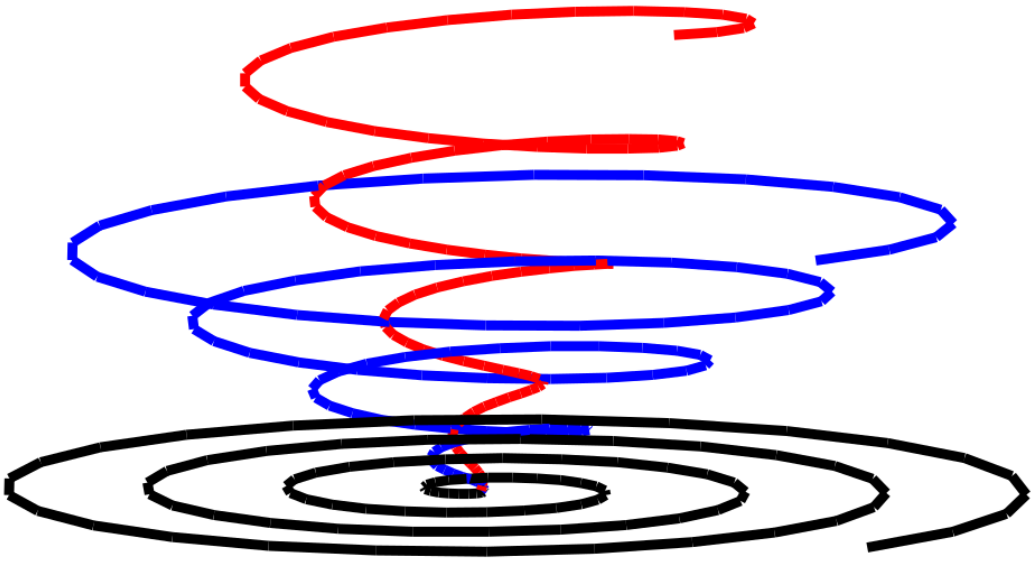

Figure 1.4: A representation of the Archimedes-Parker spiral magnetic field lines for an outflow speed of 450 km s^{-1} and between 0 and 25 au. Black, blue and red spirals correspond to 0°, 30°, and 60° in latitude, respectively. Image adapted from Owens & Forsyth (2013).

1.2 Why Parker Solar Probe and Solar Orbiter?

Two fundamental questions are currently open: how does the Sun create and control the heliosphere? Why does solar activity change with time? Concerning these points, two main areas have to be explored in detail: the inner heliosphere, in which the heliospheric structures have origin and the solar wind evolves, and the polar regions, which could give information to understand the solar dynamo processes related to the Sun's activity cycle. The results of past and present solar and heliospheric missions have laid the foundations of our understanding of the Sun and the heliosphere. However, to reach the aforementioned aims, two recent space missions have been designed: Solar Orbiter (SolO; Müller et al., 2013, 2020) and the Parker Solar Probe (PSP; Fox et al., 2016). The SolO mission activity will contribute to answer these questions by reaching a minimum distance from the Sun equal to 0.28 au (the latter unit is the "astronomical unit", which corresponds to the mean Sun - Earth distance, equal to about 1.5×10^{11} m), combining high spatial and temporal reso-

lution observations from six remote-sensing and four in-situ instruments, concerning observations of the solar corona at a given distance and measurements of the coronal plasma performed on site, respectively. SolO will provide the first out-of ecliptic (up to 25° and 33° in latitude during the nominal and extended mission phases, respectively) and outside Sun-Earth line magnetograms, which will improve the models of the extended solar magnetic field, with important space weather applications, and will add new constraints on solar dynamo models. Moreover, the out-of-ecliptic view will allow for the first time transient events observations outside the ecliptic (such as the Coronal Mass Ejections - CMEs), strictly linked with the Sun magnetic activity and with remarkable effects in local configurations of the HMF. Further results can be obtained by the synergistic activity between the Solar Orbiter and the Parker Solar Probe missions. The latter will be the first spacecraft to reach the very inner corona (under 10 $R_\odot$), until a maximum distance of about 0.25 au ($\approx$ 54 $R_\odot$). The main aims of this mission are the determination of the structure and dynamics of the magnetic field of the Sun, the understanding of how the expanding corona is accelerated and heated, how the solar magnetic activity is regulated, and what processes accelerate the energetic particles. The spacecraft will orbit the Sun in the ecliptic plane; this means that it will not sample the solar wind coming from polar CHs, but will measure the wind from equatorial CHs or the equatorial extension of high latitude CHs. Furthermore, the two spacecraft have been designed to be in quasi-corotation with the Sun. These capabilities allow to obtain detailed information on the spatial and temporal dependence of structures in the solar wind, and to understand how they merge in the inner heliosphere. In order to reach the aforementioned aims, the results coming from the instruments onboard the two spacecraft will be coupled with those returned by past and current space missions, and to data coming from future projects dedicated to the heliophysics, such us Proba-3 (Lamy et al., 2010; Renotte, 2014), the Advanced Space-based Solar Observatory (ASO-S; Gan, 2015), and Aditya-L1 (Seetha & Megala, 2017).

Chapter 2

The solar corona and the solar wind

The solar corona is the external and more extended part of the solar atmosphere, where the temperatures reach values over 10^6 K. This region is characterised by a constant flow of plasma that moves away until the ISM is reached, filling the heliosphere. The presence of this flow, the solar wind, was suspected by observations of the comet tails, and its presence was invoked to explain cosmic ray modulation, geomagnetic activity and polar auroras. Afterwards, space missions, such as Mariner and Ulysses, confirmed its existence. In the next sections, the main sources of the solar wind, the acceleration mechanisms of the coronal plasma and the role played by the magnetic field, based on more recent observations and on theoretical results, will be discussed.

2.1 Sources and structure of the solar wind

A first theoretical explanation for the solar wind source and acceleration was given by Eugene Parker (see Parker, 1958). He proposed a model based on the simple concept for which the observed flow must be present and accelerated as a consequence of the high temperatures in the corona, for which such a region is not in hydrostatic equilibrium, and a pressure gradient allows the plasma to flow outward. Assuming an isothermal corona, the mass and momentum conservation equations can be consid-

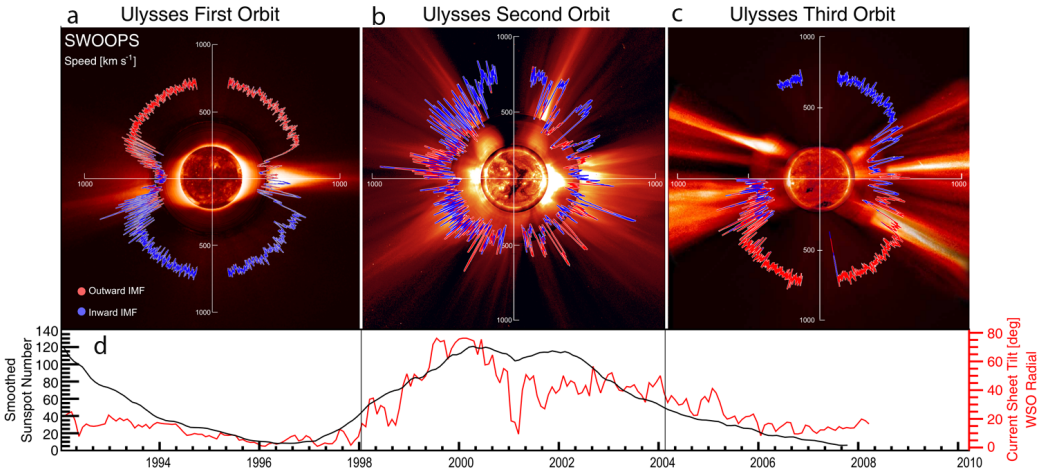

Figure 2.1: Plots of the solar wind speed obtained from Ulysses observations, along with the smoothed number of solar sunspots and the tilt angle of the modelled current sheet, both as a function of time. Image adapted from McComas et al. (2008).

ered:

$$\frac{d}{dr}(r^2 nv) = 0 \tag{2.1}$$

$$-2K_B T\frac{dn}{dr} - nm_p\frac{GM_\odot}{r^2} = nm_p v\frac{dv}{dr} \tag{2.2}$$

where m_p is the proton mass (the principal component of the solar wind), n is the proton density, G is gravitational constant, K_B is the Boltzmann constant, T is the coronal temperature, $M_\odot$ is the solar mass, and r is the radial coordinate. By combining the two equations, Parker obtained six solutions. In particular, four of them are unphysical, while one of them returns the "solar breeze" solution, with a decreasing velocity trend as a function of the heliocentric distance; however, the latter solution has not been observed until now. Then, the following expression is the approximated and only acceptable solution:

$$v(r,T) \approx \sqrt{\frac{8K_B T}{m_p}\ \ln(r)} \tag{2.3}$$

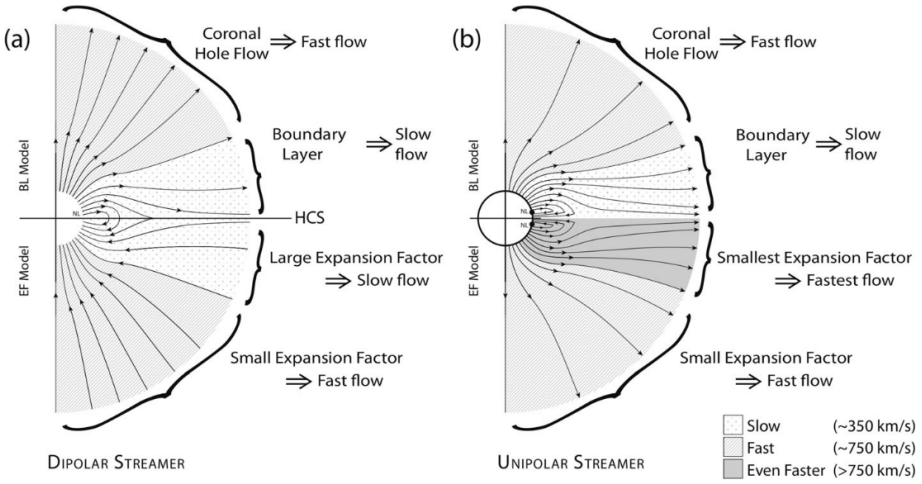

Figure 2.2: Main characteristics of the magnetic divergence (expansion factor) and boundary layer models for a) dipolar and b) unipolar streamers. Image adapted from Abbo et al. (2016).

where the solar wind velocity is characterised by an increasing trend as the distance from the Sun and the temperature increase. Furthermore, this solution provides a solar wind density decreasing trend, reaching asymptotic values comparable with those of the ISM.

However, in-situ measurements performed with the Ulysses spacecraft at different latitudes and solar magnetic activity phases confirmed that the measured flux velocities can not be explained only considering the Parker theory, and that other mechanisms must be invoked. Ulysses observations, performed between 1.4 au and 5.4 au, highlighted the presence of different regimes of solar wind (McComas et al., 1998, 2008): "slow" (until about 300 - 500 km s^{-1}) and "fast" (until about 500 - 800 km s^{-1}). The observed regimes characterise the solar wind during an entire solar activity cycle, and a link between the solar wind regimes evolution and the solar activity, highlighted by the number of sunspots over the photosphere, has been found (see Fig. 2.1). This suggests that the sources, acceleration, and evolution of the solar wind are highly dominated by the solar magnetic activity.

In fact, coronal observations coming from the UltraViolet Coronagraph Spectrometer (UVCS; Kohl et al., 1995) at the solar minimum proved

the interdependence of the geometry of the magnetic flux tubes, channeling the outflows in the solar atmosphere, and the solar wind velocity, confirming what proposed by Wang & Sheeley (1990), who showed that the magnetic field lines divergence is anticorrelated with the wind speed measured in-situ at 1 au. That is, the divergence of the open magnetic field lines rooted in the polar CHs at the solar minimum rapidly increases from the core, where the fast wind is emanated, to the boundaries, meaning that as the areal expansion of the magnetic flux tubes increases the wind outflow velocity decreases. This can be explained by the fact that the energy flux and momentum in the inner corona rapidly spread over the increasing areas of magnetic flux tubes, returning lower wind speed values. This means that, during the solar minimum, the large polar CHs are not only sources of the fast wind, emanating from their core, but they remarkably contribute to the slow wind, originating at lower latitudes by their peripheral regions. Under this scenario, the momentum transfer from turbulence, MHD waves or shocks can be important.

Interchange reconnection phenomena between open field lines in CHs and closed coronal streamer loops can occur, allowing the closed-field plasma to propagate along the open field lines, and contributing to the acceleration of the slow solar wind. MHD models predict the existence of closely connected or isolated open field regions in corona that form a web of separatrix and quasi-separatrix layers (S-Web) separating opposite polarity regions. The photospheric dynamics stress these separatrix layers and give origin to current sheets and to associated processes of interchange reconnection and coronal plasma release that contribute to the acceleration of the slow wind (for example, see Antiochos et al., 2012).

The expansion of the plasma in the heliosphere as slow solar wind can receive a contribution from thermal diffusion, instabilities or magnetic reconnections in the weak magnetic field at the streamer cusps. Confirmations of the remarkable contributions coming from this scenario are given by white light observations performed with the Large Angle and Spectrometric COronagraph (Brueckner et al., 1995), aboard the Solar and Heliospheric Observatory (SOHO Domingo et al., 1995), and the COR1 and COR2 coronagraphs onboard the twin Solar Terrestrial Relations Observatory (STEREO; Howard et al., 2008). These observations show that outflows can be connected to large-scale "streamer blowout"

structures, that are coronal mass ejections closely associated with magnetic reconnection at the current sheet above the streamer cusps, and to small-scale inhomogeneities (blobs) linked to quasi-periodic emission of plasma from cusps, accelerated by the combined effects of the tearing mode and Kelvin-Helmholtz instabilities triggered by magnetic reconnections in the current sheet above the streamers (Sheeley et al., 1997; Wang et al., 1998; Song et al., 2009; Viall & Vourlidas, 2015). The aforementioned inhomogeneities characterise the dipolar helmet streamers, which separate CHs of opposite polarity and extend to form current sheets. These structures are different from the unipolar pseudo-streamers, which, indeed, separate the CHs of like polarity and form plasma sheets, and for which the emission of blobs is not observed, although interchange reconnections can occur, contributing to the slow solar wind propagation. In particular, pseudo-streamers boundaries can show small magnetic field divergence, thus contributing in part to the fast solar wind acceleration (see Fig. 2.2). For the sake of completeness, magnetic field reversals, called "switchbacks", have been observed with Helios, Ulysses and PSP missions, and it is though that some features in the data acquired with the Metis coronagraph (Antonucci et al., 2020), onboard SolO, could be linked to the onset of these structures. It is though that switchbacks are the result of interchange reconnection processes, representing a further element contributing to the slow solar wind (Telloni et al., 2022). A representative scheme of the main described scenarios is reported in Fig. 2.3.

After this discussion on the main sources and structure of the solar wind, it is clear the reason for which, during minima phases, the quasi-steady fast wind is principally observed in the polar regions, while the more variable slow wind is observed close to the equatorial regions. Approaching the maximum of activity, the slow and fast solar wind, along with CHs and streamers, can be observed at all latitudes, highlighting the more complex configuration of the magnetic field.

2.2 Current issues

Once described the main solar wind sources and the currently accepted acceleration mechanisms, it is fundamental to better investigate how the

solar properties at the source regions characterise the properties of the solar wind, in order to infer likely mechanisms and processes responsible for the solar wind formation, and to find out further constraints for solar wind models. In this context, a remarkable contribution will be returned by the Metis coronagraph, which is the first instruments capable to simultaneously observe the visible light polarised brightness (VL pB) and the H I UV Lyα radiation in a wide field of view (FoV) and at high temporal and spatial resolution (see Chapter 4 for more details), enabling to measure the main physical parameters and dynamics of the electron and H I expanding plasma components, and to diagnose with detail the structures and dynamics of the full corona. Furthermore, its features, along with the support given by the other instruments onboard Solar Orbiter and PSP, can further address open and crucial issues of solar physics, such as the problem of the heating and acceleration of the fast and slow wind, the origin and driving of transient events and their evolution into heliosphere, and, thus, the understanding of how the Sun and the heliosphere are connected.

In the next chapters the principal coronal diagnostics techniques will be described, currently used to obtain information on the physical parameters that characterise the solar corona, along with the SolO/Metis coronagraph design, performances, data handling, and the results concerning the first data acquired with this instrument, also in synergy with data coming from the PSP spacecraft.

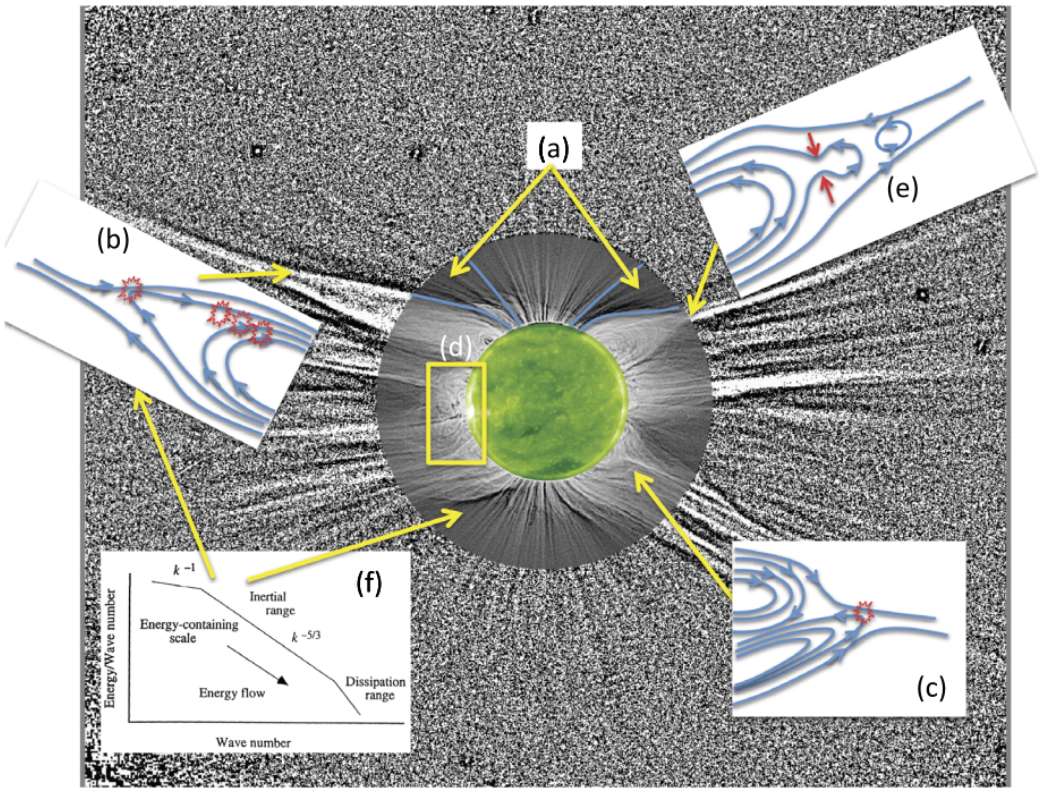

Figure 2.3: Scenarios for slow solar wind formation. The image is the composition of a white light image concerning the solar eclipse of March 29, 2006, a coronal SOHO/LASCO image and an EUV image acquired with SOHO/EIT. These scenarios consider a) the curvature of the magnetic field lines relative to a helmet streamer; b) interchange reconnection in a helmet streamer; c) interchange phenomena relative to open and closed field lines in a pseudo-streamer; d) complex magnetic structure that favors the presence of reconnection phenomena (S-Web); e) emission of blobs due to reconnection of field lines at the cusps of helmet streamers; f) heat and acceleration of the solar wind due to turbulence and waves, important in open field structures. Image adapted from Abbo et al. (2016).

Chapter 3

Diagnostics of the solar corona

The diagnostics of the solar corona has been developed in the last decades through the use of more and more complex tools, taking into account observational data from ground and space based instruments. Important missions, fundamental to obtain information about the extended corona and its surroundings, are, for example, SOHO, STEREO, and, today, Solar Orbiter and PSP. The tools developed until now allow to extract accurate information on coronal parameters, such as the electron density and the solar wind velocity. In particular, the diagnostics of the solar wind velocity can be performed by the measurements of in-situ instruments or by using simultaneous remote sensing observations of the UV radiation emitted by a specific coronal ion or atom species and of the coronal visible light radiation. In the next sections, the main coronagraphic techniques and diagnostics tools will be introduced and described.

3.1 Coronagraphic techniques

In this chapter, the main coronagraphic techniques concerning the observation of the polarised visible light and of the H I coronal Lyα used to successfully estimate the coronal electron density and the solar wind velocity are described.

3.1.1 VL pB observations

The detailed observation of the coronal visible light has been performed, during these years, by several space instruments, such as SOHO/LASCO and STEREO/COR coronagraphs (see Lamy et al., 2020, 2021, and citations therein). The polarised brightness (pB) observations allow to identify the K corona, due to the Thomson scattering of the photospheric photons by coronal free electrons. Then, the inversion method based on the work of Van De Hulst (1950) (see also Hayes et al., 2001; Quémerais & Lamy, 2002; Inhester, 2015) can be considered to infer the electron density distribution in the corona starting from pB data, as will be described later.

SolO/Metis is the most recent coronagraph able to acquire the coronal visible light radiation with high spatial and temporal resolution.

3.1.2 H I Lyα observations

The observation of the UV H I Lyα coronal radiation, centered at 121.6 nm, has been performed by the SOHO/UVCS spectrocoronagraph in the previous decades. This was the first spectrocoronagraph to observe the solar wind propagating in the atmosphere of the Sun and to characterise the wind physical properties in its early development, collecting data at different times and in a narrow instantaneous FoV.

The observed UV Lyα radiation is mainly due to the scattering of chromospheric photons by neutral coronal hydrogen atoms, although a minor (negligible) part is given by the collisional mechanism between coronal neutral hydrogen atoms and electrons. Given the not-stationary coronal conditions, the scattered Lyα photons are affected by the *Doppler dimming*, a phenomenon for which the coronal flowing hydrogen atoms are less efficient in resonantly scattering the chromospheric exciting Lyα UV radiation, due to the shift of the inner atmosphere photons to higher wavelength as seen by the flowing atoms (Withbroe et al., 1982; Noci et al., 1987). A technique based on this phenomenon and on the simultaneous acquisition of the coronal H I Lyα photons and of the coronal pB radiation, currently provided by the Metis coronagraph, allows to perform a diagnostics of the solar wind velocity.

3.2 Electron, proton, and H I densities

The determination of the coronal electron density is a problem first addressed by Minnaert (1930) and Van De Hulst (1950). The latter proposed a method based on the observation of polarised brightness (pB) in the K corona, due to the Thomson scattering of the photospheric photons by free coronal electrons, to infer the electron density trend as a function of the heliocentric distance. The first attempts to derive two-dimensional maps of the electron density were performed by assuming that pB and electron density can be represented by the product of separate functions, one of the heliocentric distance and another one of the latitude (see, for example, Saito et al., 1970; Munro & Jackson, 1977). More general solutions have been sought by expressing the electron density as a sum of Legendre polynomial functions (see Altschuler & Perry, 1972; Gabryl et al., 1999). These methods give global information on the electron density, where spherical or cylindrical symmetry hypothesis are needed. However, when transient events take place (such as CMEs), these methods are not adequate, and other diagnostics techniques must be considered (see Moran & Davila, 2004; Pagano et al., 2015; Thernisien et al., 2006; Thernisien, 2011).

The method used to infer the electron density in this thesis work is the one developed by Van De Hulst (1950), described in the following. In the spherical or cylindrical symmetry approximation, where it is assumed that, set a latitude, the electron density n_e is a function of the heliocentric distance only, the pB on the plane of the sky (POS) can be expressed as follows:

$$pB(\rho) = 2\frac{B_\odot}{1-\frac{u}{3}}\frac{3\sigma_T}{16\pi}\int_\rho^{+\infty} n_e(r)[(1-u)A(r)+uB(r)]\frac{\rho^2}{r^2}\frac{rdr}{\sqrt{r^2-\rho^2}} \quad (3.1)$$

where ρ is the heliocentric distance on the POS, r is the radial coordinate, $B_\odot$ is the mean solar brightness in the spectral band in which the pB is observed, $u = 0.63$ is the limb darkening coefficient, $\sigma_T = 6.65 \times 10^{-29}$ m^2 is the Thomson scattering cross section for electrons, and $A(r)$ and $B(r)$ are geometric factors:

$$A(r) = \cos\gamma \sin^2\gamma \tag{3.2}$$

$$B(r) = -\frac{1}{8}\left[1 - 3\sin^2\gamma\left(\frac{1+3\sin^2\gamma}{\sin\gamma}\right)\ln\left(\frac{1+\sin\gamma}{\cos\gamma}\right)\right] \tag{3.3}$$

where $\sin\gamma = R_\odot/r$.

The inversion technique developed by Van De Hulst (1950) allows to relate the electron density with the Thomson-scattered polarised brightness and to express the latter through a polynomial expression:

$$pB(\rho) = \sum_i c_i \left(\frac{\rho}{R_\odot}\right)^{-d_i} \tag{3.4}$$

where the coefficients c_i and d_i are selected through a χ^2 minimisation technique.

A polynomial formulation can also be used for the following expression

$$n_e(r)[(1-u)A(r) + uB(r)] = \sum_i a_i \left(\frac{r}{R_\odot}\right)^{-b_i} \tag{3.5}$$

The quantity in Eq. 3.1 permits to write

$$\sum_i c_i \left(\frac{\rho}{R_\odot}\right)^{-d_i} = 2KR_\odot \sum_i a_i \left(\frac{\rho}{R_\odot}\right)^{-b_i+1} \int_1^{+\infty} x^{-b_i-1} \frac{dx}{\sqrt{x^2-1}} \tag{3.6}$$

with $r = \rho x$, $b_i = d_i + 1$, and

$$K = \frac{3\sigma_T B_\odot}{16\pi(1-\frac{u}{3})} \tag{3.7}$$

Therefore,

$$\sum_i c_i = 2KR_\odot \sum_i a_i \int_1^{+\infty} x^{-b_i-1} \frac{dx}{\sqrt{x^2-1}} \tag{3.8}$$

The integral can be solved by considering the table of integrals of Gradshteyn & Ryzhik (1996):

$$\int_1^{+\infty} x^{m-1}(x^p-1)^{\nu-1}dx = \frac{1}{p}\beta\left(1-\nu-\frac{m}{2},\frac{1}{2}\right) \tag{3.9}$$

with p > 0, Re(ν) >0, Re(m) < p < (1-Re(ν)). The term β indicates the Eulero beta function:

$$\beta(y,z) = \beta(z,y) = \frac{\Gamma(y)\Gamma(z)}{\Gamma(y+z)} \tag{3.10}$$

where Γ is the gamma function. If $p = 2$, $\nu = \frac{1}{2}$, and $m = -d_i - 1$, the β function returns

$$\beta\left(\frac{d_i+2}{2},\frac{1}{2}\right) = \frac{\Gamma\left(\frac{d_i+2}{2}\right)\Gamma\left(\frac{1}{2}\right)}{\Gamma\left(\frac{d_i+3}{2}\right)} \tag{3.11}$$

where $\Gamma\left(\frac{1}{2}\right) = \sqrt{\pi}$

Finally, the a_i coefficient depends on c_i through the following expression:

$$a_i = \frac{1}{\sqrt{\pi}KR_\odot}\frac{\Gamma\left(\frac{d_i+3}{2}\right)}{\Gamma\left(\frac{d_i+2}{2}\right)}c_i \tag{3.12}$$

and the electron density is given by

$$n_e(r) = \frac{\sum_i a_i\left(\frac{r}{R_\odot}\right)^{-b_i}}{[(1-u)A(r)+uB(r)]} \tag{3.13}$$

An example of electron density map, calculated by the author of this thesis through the analysis of the Metis pB first light (May 15, 2020), is shown in Fig. 3.1. In this case, the tool reported in Appendix A has been used, based on the van de Hulst inversion method described above. This tool has been developed by the author of this manuscript, by Dr. Luca Zangrilli (INAF-OATO) and by Dr. Silvio Matteo Giordano (INAF-OATO); in particular, the author has given a remarkable contribution to its optimisation and to make it robust.

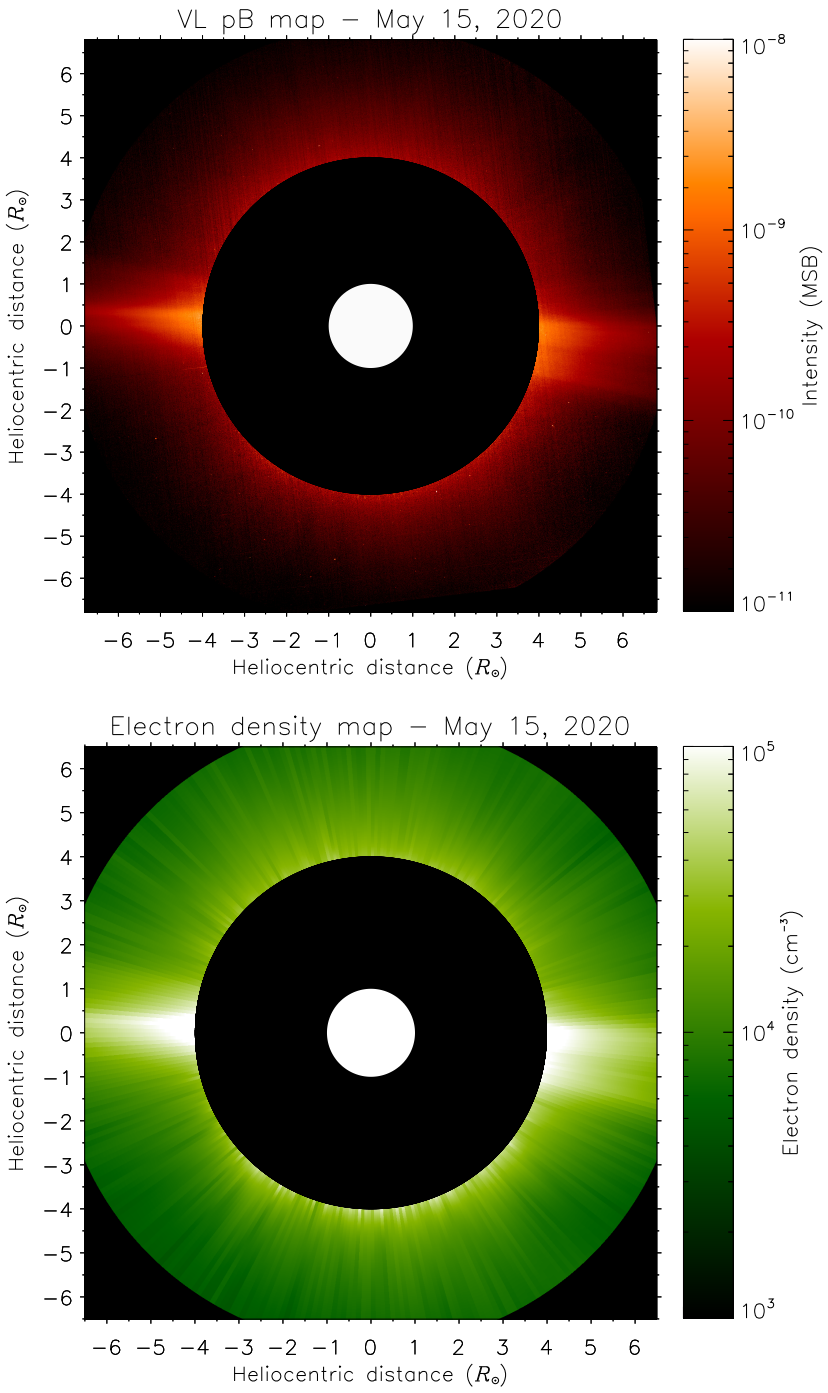

Figure 3.1: An example of pB image acquired with Metis on May 15, 2020 (first light; top panel) and the coronal electron density map obtained by applying the inversion method developed by Van De Hulst (1950) to the pB image (bottom panel).

Typical values of electron density have been given recently by Romoli et al. (2021), where the analysis of the aforementioned Metis pB first light is also reported (see Chapter 5). The density values go from about 4.0 $\times$ 10^4 cm^{-3} at 6.1 $R_\odot$ to 1.3 $\times$ 10^5 cm^{-3} at 4.1 $R_\odot$ along a streamer, and from about 5.0 $\times$ 10^3 cm^{-3} to 2.0 $\times$ 10^4 cm^{-3} outside the streamer region and in the same radial range, in agreement with the values reported in Spadaro et al. (2007). In the work of Telloni et al. (2021) the author of this thesis analysed Metis pB data concerning measurements performed on January 17, 2021 in a streamer region between 3.5 $R_\odot$ and 6.3 $R_\odot$, along with PSP data obtained at 21.4 $R_\odot$ about 16 hours later. The returned values vary from $\approx$ 2.4 $\times$ 10^3 at 21.4 $R_\odot$ to $\approx$ 4.0 $\times$ 10^4 at 3.5 $R_\odot$ (see Chapter 5).

More recent methods have been developed, based on the pioneering work of Van De Hulst (1950). Hayes et al. (2001) proposed a diagnostics technique where it is possible to use the total VL brightness (tB) to determine the coronal electron density spatial distribution. The authors implemented a way to model the F corona (due to the scattering of photospheric photons by interplanetary dust, that is the Mie scattering; for example, see Dolei et al., 2015; Lamy et al., 1997) to be subtracted from the tB and to use this one to derive the electron density. A similar approach has been followed by Quémerais & Lamy (2002). Indeed, Inhester (2015) reformulated the classical scattering calculations, taking into account the effect due to relativistic electrons. For the sake of completeness, Parenti et al. (2000) proposed a method based on the dependence on the electron density of the ratio of the radiative and collisional components of the O VI 1032 Å line. However, this technique works under the condition of a nearly static plasma, scenario that can be reached in the core of the streamer regions (for example, see Antonucci et al., 2005; Spadaro et al., 2007).

Known n_e, in order to estimate the proton density, as first approximation the presence of electrons coming from full ionised hydrogen and helium has to be considered and the following expression can be used:

$$n_p = f\ n_e \tag{3.14}$$

where the f parameter, which is the ratio between proton and electron densities, is determined for a plasma composed of hydrogen and a given

percentage of helium, both full ionised. A concentration of 10% of helium ($f = 0.83$) can be considered as an upper limit, and lower values can be adopted. For example, Telloni et al. (2021) used a value of helium abundance corresponding to 2.5% ($f = 0.95$) along a streamer, relative to a particular minimum occurred on 2009 (see Moses et al., 2020).

The neutral hydrogen density n_{HI} is much lower than proton density, and the two parameters are related by the ionisation fraction $R_{HI}(T_e) = n_{HI}/n_p$:

$$n_{HI} = R_{HI}(T_e)\ n_p = R_{HI}(T_e)\ f\ n_e \tag{3.15}$$

The $R_{HI}(T_e)$ parameter, that is only dependent on the electron temperature under the hypothesis of local ionisation equilibrium, will be described, along with the T_e parameter, in the Subsection 3.3.3

These expressions are useful when in-situ measurements are performed, such as those coming from the Solar Wind Electrons Alphas and Protons (SWEAP; Kasper et al., 2016) and the Solar Wind Analyser (SWA; Owen, 2020) instruments onboard PSP and SolO, respectively.

3.3 Solar wind outflow velocity

The pioneering works of Eugene Parker gave a first theoretical description of the nature of the expanding corona (for example, see Parker, 1958). The diagnostics of the solar wind outflow velocity has been developed during the last decades through methods that have been refined more and more. The only way to directly measure the solar wind velocity is through in-situ measurements, such as done with the Ulysses/SWOOPS (Bame, 1992) and PSP/SWEAP instruments. Important works giving the first observational information obtained with the Ulysses spacecraft are, for example, those of McComas et al. (1998, 2008), where typical velocities of about 500-800 km s^{-1} from CHs and velocities of about 300-500 km s^{-1} mainly related to the streamer belt regions have been found. A useful technique used to estimate the solar wind outflow velocity is given by the simple application of the equation of mass conservation (see Parker, 1958):

$$\frac{d}{dr}(r^2 \rho v) = 0 \tag{3.16}$$

where r is the radial coordinate, ρ is the plasma density, and v is the plasma expanding velocity. This expression means that the product between the density, the outflow velocity and the square of the radial distance is constant under stationary conditions. Therefore, known the value of the velocity in a given point and the density distribution (see Section 3.2), the outflow velocity can be inferred along the relative radial direction.

Remote sensing determination of the wind velocity can be performed through inversion techniques based on the observation of several coronal quantities, along with the use of parameters coming from models or reported in literature. The more recent and complex (and refined) one is the Doppler dimming technique, based on the simultaneous observation of coronal visible light and of coronal UV lines (such as those relative to the H I Lyα and O VI emissions). Metis is the first coronagraph designed to obtain simultaneously H I Lyα and VL data in a wide FoV, through an UV channel centered on the Lyα central wavelength (121.6 nm) and through a visible light channel designed to acquire photons in the spectral band 580 - 640 nm. This means that the Metis observations are useful to provide, for the first time, detailed maps of the coronal solar wind velocity, obtaining information about its onset and acceleration.

3.3.1 Doppler Dimming technique for the Lyα line

The coronal intensity is mainly due to two mechanisms: collisions of atoms and ions with free electrons and resonant scattering of the chromospheric radiation. However, in the case of the H I Lyα emission, the collisional term contributes only to a small and negligible fraction of the total coronal emission (Gabriel, 1971; Raymond et al., 1997, Degli'Innocenti; private communication quoted in Noci et al., 1987), given the low-density conditions present in the outer corona and the stronger dependence of the collisional component $\mathcal{I}_{col}$ of the coronal intensity on the electron density n_e (i.e., $\mathcal{I}_{col} \propto n_e^2$) with respect to the resonant one $\mathcal{I}_{rad}$ (i.e., $\mathcal{I}_{rad} \propto n_e$; see Withbroe et al., 1982).

The resonant scattering process is maximum if the coronal scattering elements are not flowing, that is a scenario of static corona. However, when the more realistic scenario of not-static corona is considered and the atoms and ions flow out as solar wind, the scattered chromospheric Lyα photons are affected by the Doppler dimming phenomenon (which will be described later). Under the hypothesis of low-density plasma in the solar corona, the radiance $\mathcal{I}_{rad}$ (in units of erg cm^{-2} s^{-1} sr^{-1}) coming from H I atoms along the $\mathbf{n}$ direction, corresponding to the light-of-sight (LOS), can be expressed as:

$$\mathcal{I}_{rad}(\mathbf{n}) = \frac{f\ h\ B_{12}}{4\pi\lambda_0} \int_{-\infty}^{+\infty} n_e\ R_{HI}(T_e)$$

$$\times \int_{\Omega} \frac{11 + 3(\mathbf{n}\cdot\mathbf{n}')^2}{12}\ F(\mathbf{n}', v_w, \theta)\ d\Omega\ dl \tag{3.17}$$

where f has been introduced in Eq. 3.14, concerning the helium abundance, h is the Planck constant, $\lambda_0 = 121.567$ nm is the central wavelength of the Lyα transition, B_{12} is the Einstein coefficient for the Lyα transition, $\mathbf{n}'$ is the direction along which the chromospheric radiation reaches the generic coronal scattering point P on the $\mathbf{n}$ direction (see Fig. 3.2), Ω is the solid angle under which the point P subtends the solar disc, $p(\Omega) = [11 + 3(\mathbf{n}\cdot\mathbf{n}')^2]/[12\ (4\pi)]$ is a geometrical factor, giving the angular dependence of the scattering process (see Beckers & Chipman, 1974), dl is the infinitesimal path along the LOS, and

$$F(\mathbf{n}', v_w, \theta) = \int_{-\infty}^{+\infty} I(\lambda - \lambda_0 - \delta\lambda, \mathbf{n}')\ \Phi(\lambda - \lambda_0)\ d\lambda \tag{3.18}$$

is the convolution between the chromospheric specific intensity $I(\lambda - \lambda_0 - \delta\lambda, \mathbf{n}')$ and the normalised coronal absorption profile $\Phi(\lambda - \lambda_0)$, where λ is the wavelength. The term

$$\delta\lambda = \frac{\lambda_0}{c}\mathbf{v}\cdot\mathbf{n}' = \frac{\lambda_0}{c} v_w \cos\theta \tag{3.19}$$

is the Doppler shift seen along $\mathbf{n}'$ by the scattering flowing hydrogen atoms with the velocity $\mathbf{v}$ (assumed radially oriented), where v_w is the module of $\mathbf{v}$, θ is the angle between $\mathbf{v}$ and $\mathbf{n}'$, and c is the speed of the electromagnetic radiation in vacuum.

A clear description of the geometry of the scattering process is reported in Fig. 3.2.

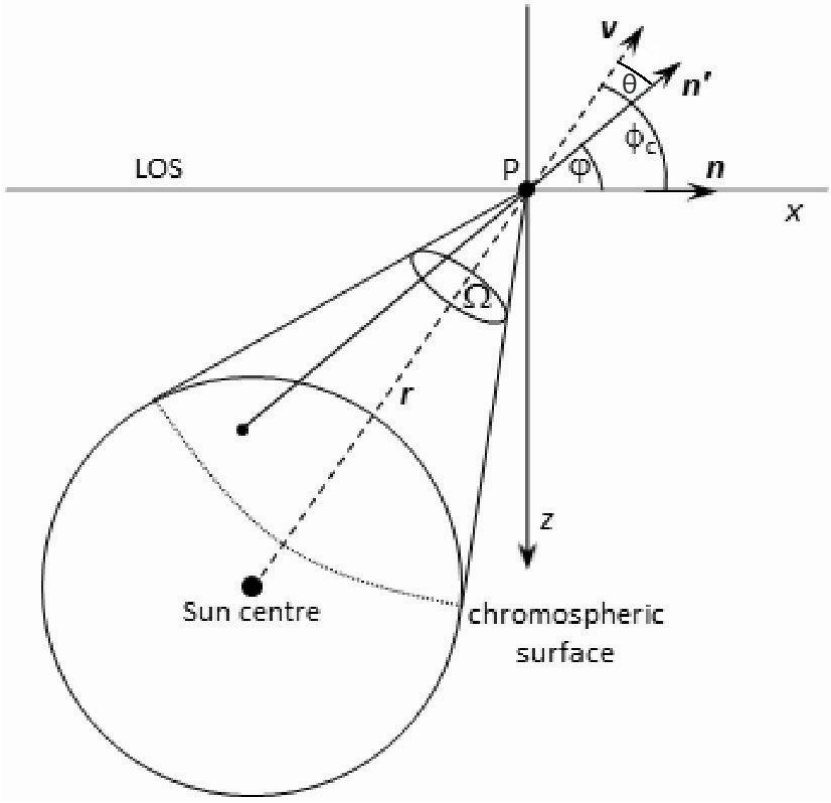

Figure 3.2: Geometry for the coronal resonant scattering process in the point P. The Cartesian y-axis points outwards from the plane of the page. Image adapted from Dolei et al. (2015).

The specific chromospheric intensity $I(\lambda - \lambda_0 - \delta\lambda, \mathbf{n}') = I(\mathbf{n}') \cdot \Psi(\lambda - \lambda_0 - \delta\lambda)$ is the product between the radiance $I(\mathbf{n}')$ (in units of erg cm^{-2} s^{-1} sr^{-1}) and the exciting profile $\Psi(\lambda - \lambda_0 - \delta\lambda)$ (in units of Å^{-1}) of the chromospheric Lyα line. Then, $F(\mathbf{n}', v_w, \theta)$ gives information about the dependence of the radiative excitation efficiency by chromosperic radiation on the H I atoms velocity. If the velocity distribution of the absorbing H I coronal atoms is assumed to be a Maxwellian, the normalised coronal absorption profile $\Phi(\lambda - \lambda_0)$ has a width that depends on the thermal motion only, neglecting all contributions coming from non-thermal phe-

nomena (such as turbulence, waves, and oscillations):

$$\Delta\lambda_D = \frac{\lambda_0}{c}\sqrt{\frac{2\ K_B\ T_{HI}}{m_H}} \tag{3.20}$$

where T_{HI} is the H I temperature, and m_H is the mass of hydrogen atoms.

It is possible to define the "Doppler factor" $D(v_w)$:

$$D(v_w) = \frac{\int_\Omega\ F(\mathbf{n}', v_w, \theta)p(\Omega)\ d\Omega}{\int_\Omega\ F(\mathbf{n}', v_w = 0, \theta)p(\Omega)\ d\Omega} \tag{3.21}$$

which accounts for the overlapping between the coronal absorption profile and the exciting chromospheric one as a function of v_w. The behaviour of this parameter helps to understand how the dimming depends on the outflow velocity of scattering atoms (see Fig. 3.3). Let us consider the Doppler redshift of the chromospheric radiation with respect to a reference system integral with the scattering point P. When the corona is in a static condition, the profile of the chromospheric Lyα is centred at λ_0 and, then, the overlapping between the exciting and absorption profiles has the highest value, causing the maximum intensity of the scattered Lyα radiation ($D = 1$). However, when the corona is expanding, the scattered Lyα is dimmed because of the Doppler shift of the chromospheric exciting profile seen by the outflowing coronal H I atoms, so that the overlapping with the absorption profile decreases. The intensity of the scattered radiation tends to vanish when the outflow velocity reaches high values, because the chromospheric and coronal profiles no longer overlap ($D \approx 0$).

A numerical tool has been developed, where the synthetic and observed UV intensities are compared and the value of the outflow velocity (the only free parameter) is determined by iteratively changing it until a satisfactory match between the two intensities is reached (see Dodero et al., 1998; Dolei et al., 2015, 2018, 2019; Romoli et al., 2021; Capuano et al., 2021; Telloni et al., 2021; Antonucci et al., 2023; Telloni et al., 2023). Such a tool, used to obtain the HI solar wind velocity results described in Chapter 5, is reported in Appendix B, where the author of this thesis work has given a remarkable contribution to its optimisation and to make it robust, such as done for the tool reported in Appendix A.

3.3.2 Comparison with the use of other coronal lines

In the previous paragraph the Doppler dimming technique has been explained in the case of the Lyα emission. However, this is not the only spectral line that can be considered in order to apply this method for the determination of the solar wind outflow velocity. The O VI doublet can be used (Noci et al., 1987), characterised by lines centered at 1032 Å (2s $^2S_{1/2}$ -2p $^2P_{3/2}$ transition) and 1037.6 Å (2s $^2S_{1/2}$ -2p $^2P_{1/2}$ transition). When the oxygen ions flow out, the photons coming from the transition region are seen red-shifted by the flowing ions (as explained in the previous paragraph), and the O VI 1037.6 Å transition region exciting line profile no longer overlaps the absorption coronal profile. However, the C II line centered at 1037 Å can be Doppler shifted to higher wavelength, such that, at reasonable solar wind velocities, this line can approach the O VI 1037.6 Å central wavelength and can excite the O VI atoms. This results in an increase of the scattered intensity as the outflow velocity increases (see Fig. 3.4). This does not happen in the case of the Lyα line, because close to the line there are not spectral lines capable to pump the Lyα line as the velocity increases, so the coronal intensity is a decreasing function of velocity.

For what concerns the emissivity of the O VI , the population of the 2p $^2P_{3/2}$ level is twice that of the 2p $^2P_{1/2}$ level. Since the transition region is effectively thin in the 1032 Å and 1037.6 Å lines, all photons emitted in these spectral lines in a volume element within the transition region escape from this region (Pottasch, 1964). Therefore, the intensity of the 1032 Å line will be twice that of the 1037.6 Å line. The outflow velocity of the ions, thus, can be inferred by performing the ratio between the O VI coronal 1032 Å and 1037.6 Å lines intensities. This one remains constant until the pumping due to the C II line does not show any effect. However, when the pumping starts, the ratio value increases as the velocity increases. Then, by comparing the synthetic ratio computed through appropriate models with the experimental one derived from observations, it is possible to infer the outflow velocity. Furthermore, the introduced ratio is independent of the lines calibration, reducing the uncertainties in the measurements. This method allows to reach a good sensitivity up to velocities of about 450 km s^{-1}, while with the dimming of the Lyα line

the sensitivity is high between about 100 - 350 km s^{-1} (Noci et al., 1987).

(Vernazza & Reeves, 1978) revealed that other resonance doublets in the solar EUV spectrum are expected to have one or both lines enhanced via Doppler-shift phenomena. Those which belong to the most abundant coronal ions are the 335.407 Å and 360.798 Å of Fe XVI and 609.76 Å and 624.93 Å of Mg X .

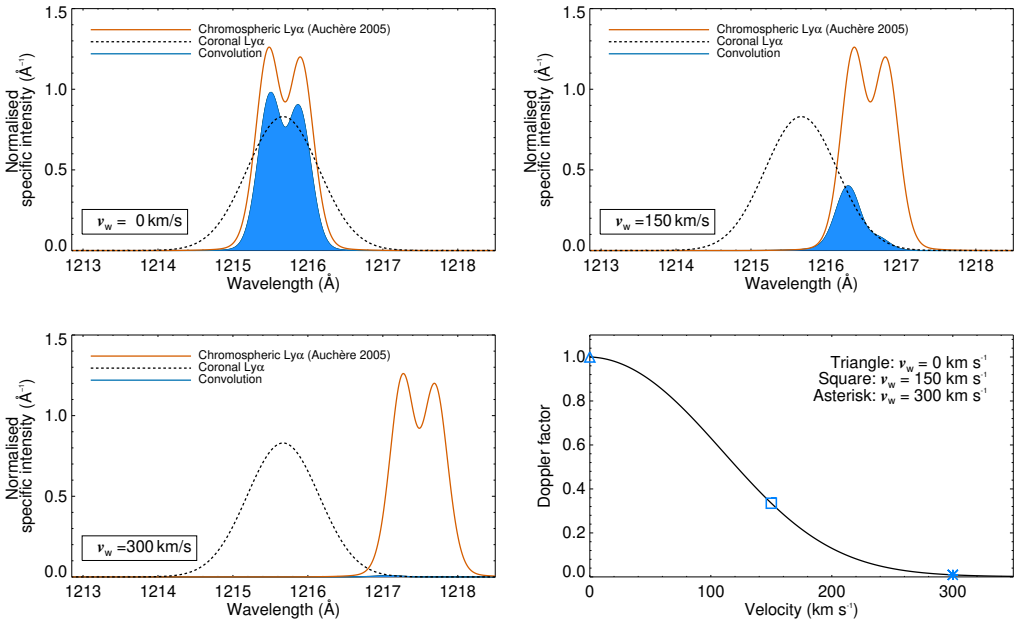

Figure 3.3: Panels a-b-c: overlap between the normalised coronal and chromospheric Lyα line profiles (chromospheric - solid red line; coronal - dotted black line). The analytical model of chromospheric Lyα line profile reported in Auchère (2005) and a Gaussian coronal profile with a thermal width obtained by setting an isotropic T_{HI} = 1.6 × 10^6 K have been considered. The following cases have been taken into account: v_w = 0 km s^{-1}, v_w = 150 km s^{-1}, and v_w = 300 km s^{-1}. The blue area indicates the convolution between the two profiles. Bottom panel: Doppler factor as a function of v_w. The triangle, square, and asterisk refer to v_w = 0 km s^{-1}, v_w = 150 km s^{-1} and v_w = 300 km s^{-1}, respectively.

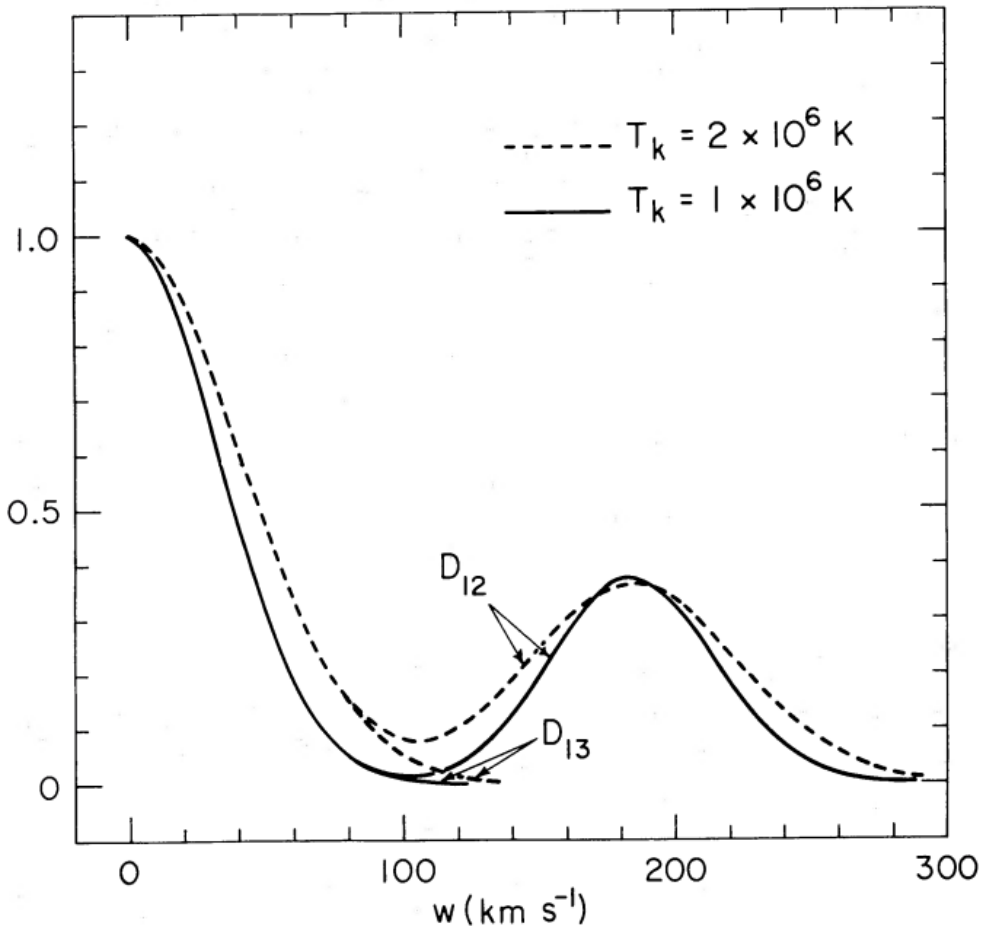

Figure 3.4: Doppler dimming of coronal O VI ions for an heliocentric distance equal to 2 $R_\odot$ and for two different neutral coronal temperatures (1×10^6 K - solid line - and 2×10^6 K - dashed line). D_{12} and D_{13} are the normalised emissivities for the 1037.6 Å and 1032 Å lines, respectively (see Fig. 2 of Noci et al., 1987).

3.3.3 Parameters on which the Doppler Dimming technique depends

Once reported the expression for the synthetic coronal intensity in the case of the Lyα line emission (Eq. 3.17), in this paragraph the parameters on which the intensity depends will be described. The electron density parameter, from the observational and diagnostics point of view, has been

introduced in Section 3.2. The details concerning the other parameters will be described in the following.

Electron temperature

The electron temperature can be extracted by theoretical models. An example is done by Gibson et al. (1999), where the authors estimated the electron density with the inversion method of Van De Hulst (1950) applied to observation of white light and used the inferred density to deduce the electron temperature in a streamer region. In particular, they assumed that the plasma in the streamers is in hydrostatic equilibrium (see also Raymond et al., 1997; Li et al., 1998). This means that significant dynamic or magnetic forces can be negligible and the total thermal pressure is exactly balanced by gravity:

$$\nabla P = -\frac{1+4\alpha}{1+2\alpha}\frac{GM_{\odot}m_p n_e}{r^2} \tag{3.22}$$

where α is the helium number density relative to the hydrogen, and the other parameters have been introduced previously. By integrating this expression, the thermal pressure can be extracted and the ideal gas law can be considered to obtain the electron temperature:

$$T = \frac{1+2\alpha}{2+3\alpha}\frac{P}{n_e K_B} \tag{3.23}$$

The temperature calculated in this way has a maximum value of about 1.50×10^6 K at 1.5 $R_{\odot}$ and a value of about 0.2×10^6 K at 10 $R_{\odot}$.

Another method for inferring the electron temperature is the use of spectral line intensities ratios of two lines of the same ion. For example, Wilhelm et al. (1998) used Mg IX line intensities at 706 nm and 750 nm measured with the Solar UV Measurement of Emitted Radiation (SUMER; Wilhelm et al., 1995), aboard the SOHO spacecraft, to estimate the electron temperature in CHs between 1.03 $R_{\odot}$ and 1.6 $R_{\odot}$, where values of about 10^6 K have been found. In particular, the authors suggest that near the minimum of solar activity the electrons in the polar regions are cooler than the ions (see also Landi et al., 2001). A similar approach has been followed by Boe et al. (2022) by using Fe X (637.4 Å), Fe XI (789.2 Å) and

Fe XIV (530.3 Å) lines; in particular, the Fe XIV/Fe X and Fe XIV/Fe XI ratios have been employed. The analyses performed with both ratios return the same electron temperature, with the streamers having values of about 1.65×10^6 K at the core, and closer to 1.5×10^6 K at their border; the CHs reach temperatures going from about 1.25×10^6 K to 1.4×10^6 K. Similar values have been found by Cranmer (2020), who performed an analysis through Monte-Carlo simulation under momentum conservation hypothesis. In a balloon-borne investigation of a coronal streamer within 4 $R_\odot$ and 7 $R_\odot$, Gopalswamy et al. (2021) found electron temperatures with values of $1.0 \pm 0.3 \times 10^6$ K, close to the value of $1.1 \pm 0.3 \times 10^6$ K found for streamers by Fineschi et al. (1998) at 2.7 $R_\odot$.

Measurements of the solar wind charge state performed in-situ can be used to estimate the coronal electron temperature. Ko et al. (1997) derived polar electron temperature profiles from observations with the Ulysses/SWICS instrument (Gloeckler et al., 1992), and their results can be expressed as a combination of two power laws (see also Cranmer et al., 1999):

$$T_e(r) = 10^6(0.35r^{1.1} + 1.9r^{-6.6})^{-1}K \tag{3.24}$$

Vasquez et al. (2003) give a generalisation of the previous expression, in order to describe the radial dependence of the electron density in equatorial and polar regions (also in this case assuming the hydrostatic equilibrium):

$$T_e(r) = T_0\frac{a+1}{a + br^{\alpha} + (1-b)r^{-\beta})} \tag{3.25}$$

where T_0 is the temperature at the coronal base (r = 1 $R_\odot$) and the values of a, b, α, and β are listed in Table 1 of Vasquez et al. (2003). As can be deduced, the electron temperature in the polar regions is lower than that corresponding to streamer regions. However, it is possible to note that the temperature inferred, for example, by Vasquez et al. (2003) (see Fig. 2 of the cited paper) in the equatorial regions is remarkably higher that that proposed by Gibson et al. (1999).

The electron temperature plays a fundamental role in the determination of the time-steady neutral hydrogen concentration. As said in Section 3.3, the neutral hydrogen density is computed under the assumption

of local coronal ionisation equilibrium, for which the local ratio $\frac{n_{HI}}{n_p}$ is a function of only the electron temperature. In order to determine this ratio, equilibrium tables from the CHIANTI atomic database can be used (see, for example, Dere et al., 1997; Landi et al., 2013), where this ratio as a function of T_e is listed for temperatures values going from 10^4 K to 10^9 K. Cranmer (2020) reports an analytical expression inferred by fitting the equilibrium curve between 10^6 K to 10^8 K with a 10% of accuracy:

$$\frac{n_{HI}}{n_p} = \left(\frac{0.59}{T_e}\right)^{1.063} \tag{3.26}$$

where n_p is given by Eq. 3.14 and the electron temperature is expressed in kelvin. This means that the higher is T_e, the lower is the fraction of neutral hydrogen available to scatter the chromospheric photons. At large heliocentric distances, where the density is lower and the corona is far to be static, the coronal ionisation equilibrium is not always a valid assumption.

Neutral coronal hydrogen kinetic temperature

This parameter can be inferred by measurements of the thermal width of the considered dimmed line along the LOS, perpendicular to the assumed radial magnetic field. However, the obtained temperature along the LOS not only contains the effects of thermal mechanisms, but it is also characterised by non-thermal contributions, coming from the solar wind outflow velocity component along the LOS, and from turbulence, waves, and oscillations, which release energy across the magnetic field lines and can induce the plasma to show higher temperatures in the direction perpendicular to the magnetic field lines. This means that the temperature measured along the LOS ($T_{HI_\perp}$), the latter assumed perpendicular to the magnetic field lines, can be different from the temperature parallel to the magnetic field lines ($T_{HI_\parallel}$), deviating from the isotropic scenario. The anisotropy is remarkable where the density is lower (for example, at high heliocentric distances and in the polar regions when the Sun is near the minimum phase of activity), due to deviations from thermal equilibrium.

A good approach for the evaluation of $T_{HI_\parallel}$ is to set this parameter equal to the isotropic electron temperature (see Vasquez et al., 2003; Ro-

moli et al., 2021), where this assumption is reasonable by the confirmation given by in-situ measurements, showing that $T_{HI_\perp} > T_e$ in polar regions (for example, see Marsh et al., 1982; Pilipp, 1987).

Kohl et al. (1998) and Cranmer et al. (1999) analysed H I Lyα line profiles observed in polar CHs during the minimum centered around 1996–1997. They returned perpendicular temperatures up to 6×10^6 K.

Vasquez et al. (2003) proposed an analytical expression for the perpendicular proton temperature $T_{p_\perp}$ as a function of the heliocentric distance, obtained by UVCS data relative to observations performed on 1996 (Raymond et al., 1997):

$$T_{p_\perp} = T_0 \frac{a+1}{a + br^\alpha + (1-b)r^{-\beta}} + T_1 \frac{(r-1)^2 \; e^{-(r-1)/\Delta r}}{(r_{max}-1)^2 \; e^{-(r_{max}-1)/\Delta r}} \tag{3.27}$$

where the parameters are listed in Table 1 of Vasquez et al. (2003). This expression can be applied to infer the perpendicular H I temperature $T_{HI_\perp}$ when thermal equilibrium is present and the charge exchange mechanism is efficient, since the proton temperature can be used as a proxy for the H I temperature.

Dolei et al. (2016) released a database with H I temperature spatial distributions by analysing UVCS data for polar, mid-latitude and equatorial regions for different solar phases, from 1996 (minimum) to 2004 (declining phase after maximum), obtaining for the first time a global mapping of the neutral hydrogen temperature in the solar corona. In particular, the perpendicular temperatures measured by Dolei et al. (2016) reached values up to 3.35×10^6 K, 1.45×10^6 K, 2.30×10^6 K at the minimum, intermediate and maximum phase of solar cycle, respectively. The authors also estimated the parallel temperatures starting from the measured perpendicular temperatures and using the values of anisotropy inferred by Cranmer et al. (1999) and Spadaro et al. (2007).

Cranmer (2020) gives values similar to those reported in Dolei et al. (2016), in particular subtracting a power-law modelled turbulence contribution from the kinetic temperature.

For the sake of completeness, it is worth to note that other elements, such as O VI and Mg X, can reach higher temperatures. For example, Cranmer et al. (2008) found temperatures up to about 3×10^8 K for the

O VI , while Kohl et al. (1999) reported temperatures of about 7×10^7 K for the Mg X .

Chromospheric radiance

The chromospheric intensity enters in the expression of the synthetic intensity as a fundamental parameter for the pumping of the corresponding coronal line. Solar disc values can be obtained by observations, such as those concerning the SOLar STellar Irradiance Comparison Experiment (SOLSTICE Rottman & Woods, 1994) aboard the Upper Atmosphere Research Satellite (UARS Reber, 1990), as explained, for example, in Lemaire et al. (1998, 2002, 2015).

Another possibility is to use Carrington maps of chromospheric intensity concerning Carrington rotations that include a given time interval relative to a solar rotation. Then, a Carrington map is built by taking intensity profiles along the central meridian, as seen from Earth, of full-disc images over 27 consecutive days and placing them next to each other after correcting for the cosine distortion with latitude (Dolei et al., 2019). Unfortunately, a Carrington map neglects the temporal evolution of solar features and transient events, such as flares and CMEs, although it provides a satisfying distribution map of the chromospheric Lyα radiance over the entire solar disc. Because of the lack of systematic full-disc Lyα observations in the past years, Auchère (2005) proposed a correlation function between the H I Lyα line radiance at 121.6 nm ($I_{121.6}$) and the He II line radiance at 30.4 nm ($I_{30.4}$) on the solar disc:

$$I_{121.6} = 436[1 - 0.955 \exp(-0.0203 I_{30.4})] \tag{3.28}$$

Then, this expression, obtained by comparing the two full-disc lines, can be used to convert He II images into H I Lyα images.

The Extreme Ultraviolet Imager (Rochus et al., 2020), onboard Solar Orbiter, could provide Lyα data with high temporal and spatial resolution from the chromosphere to the low corona. The instrument is also capable to observe the 30.4 nm He II line, such that the expression reported in Auchère (2005) could be revisited.

The ASO-S mission, the first Chinese space solar mission launched on October 9, 2022 and characterised by a polar Earth orbit, will provide

high quality Lyα disc and coronal data.

Dolei et al. (2019) showed that the use of a single value applied over the entire solar disc (uniform scenario) and the application of a built Carrington map to account of structures such as ARs and CHs (non-uniform scenario) returns remarkable differences in the velocity determination. The uniform scenario gives overestimated values in the polar and mid-latitude regions (up to 60 km s^{-1} in velocity), while at the lower latitudes the values are underestimated of a similar quantity, because the presence of ARs is neglected. These effects are remarkable at low heliocentric distances, but at higher distances from the Sun the ARs and CHs illuminate equally the corona, reducing the differences between the two considered scenarios.

Chromospheric exciting profile

An important parameter that plays a fundamental role in the calculation of the synthetic Lyα coronal intensity is the chromospheric exciting Lyα profile. A particular feature of the chromospheric Lyα profile is the characteristic reversal at its center, with the formation of two generally asymmetric "peaks", where the reddest one has a lower intensity with respect to the bluest one (see Fig. 3.5). The effects of the variation of the chromospheric exciting Lyα profile shape on the Doppler dimming technique and, then, on the determination of the solar wind outflow velocity have been studied by Capuano et al. (2021). The details of the last cited work, of which the author of this thesis is the first author, are reported in the following.

For this study, full-disc Lyα line profiles were taken into account, provided by Lemaire et al. (2015). These data, consisting of 43 profiles, do not give information on the variations of the chromospheric Lyα profile relative to different regions on the solar surface, although they cover an entire solar cycle, and the shape could be affected by the solar activity. In order to consider all the possible chromospheric regions that emit the exciting radiation, quiet sun (QS) and CHs observations of the chromospheric Lyα line profiles were taken into account considering the SUMER/SOHO observations during the solar activity cycle 23, along with ARs and QS profiles carried out by the Ultraviolet Spectrometer and Polarimeter (UVSP;

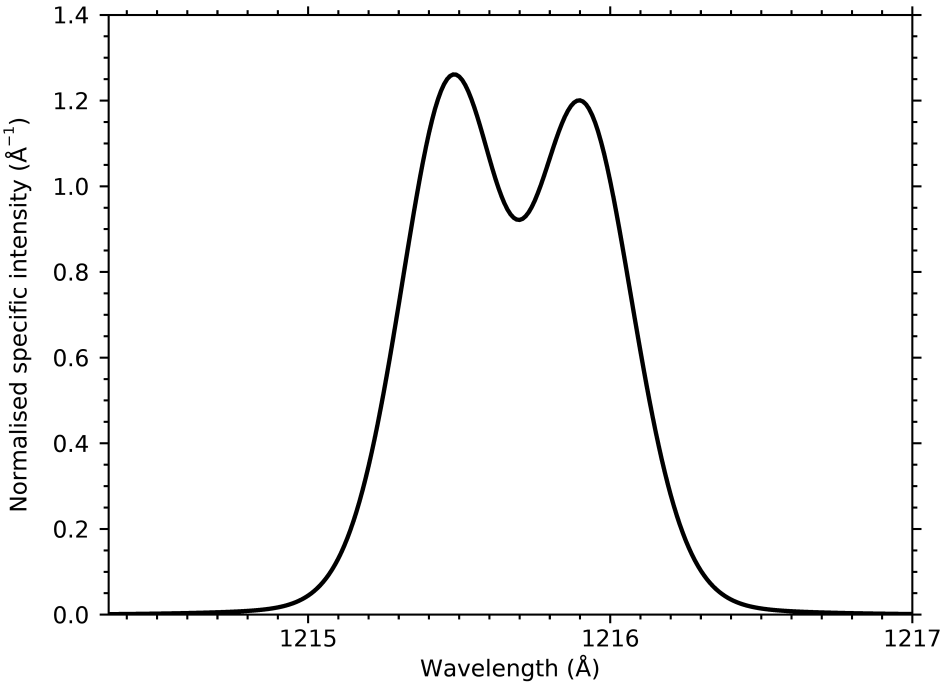

Figure 3.5: Chromospheric exciting Lyα profile obtained following the analytic expression proposed by Auchère (2005).

Miller et al., 1981) aboard the Solar Maximum Mission (SMM; Woodgate et al., 1980), and profiles of an equatorial CH and a flare acquired by the Laboratoire de Physique Stellaire et Planetaire (LPSP; Artzner et al., 1977; Bonnet et al., 1978) aboard the Eight Orbiting Solar Observatory (OSO-8) spacecraft.

In particular, two profiles observed on September 23, 2008 (QS) and on April 17, 2009 (CH) were considered from SUMER observations (Tian et al., 2009a,b). The UVSP profiles, reported by Fontenla et al. (1988) in their Figs. 3, 5, 6, and 12, were corrected for the absorption contribution due to the neutral hydrogen in the geocorona, that is the outermost part of the Earth exosphere. The profiles observed with the OSO-8/LPSP instrument were acquired in an equatorial CH at the central meridian, as seen from Earth, between 27 and 29 November, 1975 (Bocchialini & Vial, 1996), and

in a faint flare that occurred in an AR observed on April 15, 1978 (Lemaire et al., 1984).

For the sake of completeness, the Chromospheric Lyman Alpha Spectropolarimeter (CLASP) observed the Sun in H I Lyα during a suborbital rocket flight in 2015 Schmit et al. (2017). These observed profiles were in agreement with the early measurements of Gouttebroze et al. (1978). However, they were affected by geocoronal absorption and water vapor contamination, and then they were not considered for the present analysis.

Of all the considered profiles, only four couples were selected to study the velocity determination effects linked to each parameter on which the chromospheric profile depends: line width, reversal depth, asymmetry of the peaks, and separation of the peaks. Each selected profile, shown in Fig. 3.6 (top panel), represents an extreme case for the considered profile parameters.

For what concerns the line width investigation, the full width at half maximum (FWHM) of each Lyα chromospheric profile was determined once these were normalised to the corresponding radiance. Given the two characteristic peaks, the mean of their maximum value was adopted as the maximum intensity of the Lyα line profile, and its half value was used to determine the FWHM of the lines. For the profile without reversal, relative to the AR 2340 and reported in Fig. 12 of Fontenla et al. (1988), the FWHM was calculated by performing a Gaussian fit. The two line profiles that exhibit the largest difference between their FWHMs correspond to that observed on April 17, 2009 (polar CH) and that reported in Fig. 12 of Fontenla et al. (1988) (AR 2340), respectively (see fig. 3.7, top panel). A maximum difference between the line widths of about 50% has been found with respect to the smallest width value.

The shallowest and the deepest profiles in terms of reversal depth are those shown in Fig. 12 and Fig. 6a (QS) of Fontenla et al. (1988), respectively (see Fig. 3.8, top panel). The depth was calculated by considering the minimum central intensity value of each profile and dividing this by the mean value between the maximum intensities of the peaks. The reversal depth variation of the deepest profile is equal to about 69% with respect to the shallowest one.

The peak-to-peak asymmetry between the peaks of each profile was

measured by considering the ratio $I_{peak-blue}/I_{peak-red}$ between the intensity of the blue and red peaks. The profile with the largest ratio is that observed on October 28, 1996, relative to the full disc, which is characterised by the highest blue asymmetry ($I_{peak-blue}/I_{peak-red}$ = 1.16). To study the effects induced by the asymmetry of the peaks on the estimate of the outflow velocity of the coronal neutral hydrogen, the synthetic and reddest asymmetric profile ($I_{peak-blue}/I_{peak-red}$ = 1/1.16 = 0.86) was considered, obtained by taking the opposite of the bluest asymmetric profile (see Fig. 3.9, top panel).

The line profiles with the largest and smallest peak wavelength separations are those observed on April 17, 2009 (polar CH) and in the equatorial CH at the central meridian, as seen from Earth, on 27-29 November, 1975, respectively; the separation variation is equal to about 50% with respect to the smallest separation value (see Fig. 3.10, top panel).

Two further different profiles relative to ARs were compared. The first one, reported in Fig. 5a of Fontenla et al. (1988) (AR 2363), shows a remarkable reversal, while the second one is characterised by a negligible reversal, shown in Fig. 12 of Fontenla et al. (1988), concerning the AR 2340 (see Fig. 3.11, top panel).

The characteristic Lyα profile of a faint flare observed in an AR, reported in Fig. 2e of Lemaire et al. (1984), was also took into account, comparing it with the profile observed on AR 2340 (see Fig. 3.12, top panel).

Furthermore, the analytic expression for the Lyα irradiance profile proposed by Auchère (2005) was considered in this analysis, along with two cases of the parameterised profile reported in (Kowalska-Leszczynska et al., 2018, hereafter referred to as IKL). The first one consists of a sum of three Gaussian components (one of which is reversed to account for the profile reversal), introduced to reproduce the mean Lyα observed profile during a solar minimum. The other theoretical profile is built by taking into account the sum of a k-function, a reversal Gaussian function reproducing the line reversal, a straight line that simulates the background, and the disc irradiance. Then, the IKL profile were calculated for the maximum and minimum irradiance values reported in Table A of Lemaire et al. (2015) (see Fig. 3.13).

The velocity differences inferred by the adopted profiles have been

obtained by comparing their Doppler factor curves (see bottom panels in Figs. 3.7, 3.8, 3.9, 3.10, 3.11, 3.12, and 3.13). The obtained values are within about 22 km s^{-1} when the extreme observed cases are considered (excluding the flare profile). In the case of the parameterised profiles, the differences are within 30 km s^{-1}, except for values of Doppler dimming factor $D(v_w)$ close to zero, where the uncertainties in the outflow velocity are much higher. In both cases of observed and parameterised profiles consideration, for the latter excluding the range where the outflow velocity uncertainties are high, the Doppler factor curves do not differ remarkably, and the relative velocity differences are below about 9% and 12%, respectively. Taking into account the AR profiles with and without reversal, and the profile observed during a flare and that without reversal, the velocity differences are under 10 km s^{-1} for the former case, while they reach values of about 100 km $^{-1}$ in the latter case. In fact, in the former case the Doppler factor curves differences are very negligible, while in the latter case the differences are significant, and both cases show relative velocity differences values of about 3% and 21%, respectively. The main properties of the selected observed profiles and the provided velocity differences for observed and parameterised profiles are listed in Table 3.1.

The performed analysis suggests that even the largest variations actually observed in the parameters on which the chromospheric Lyα profile depends, related to the solar magnetic activity and to different disc regions, return small differences in the neutral hydrogen outflow velocity determination. Only when the flare profile is considered, the differences are significant.

The effects induced by considering different values of the angle between the plasma flow and the chromospheric photons directions, which is indicated by θ, were also investigated. It was found that if $\theta > 0^\circ$, the Doppler factor curve has a smoother trend than for $\theta = 0^\circ$. In particular, the case of $\theta = 30^\circ$ was studied (see Fig. 3.14). This means that, fixed a value of the Doppler factor, the corresponding velocity value is greater when $\theta > 0^\circ$. However, the velocity differences remain below about 70 km s^{-1} in this case ($\theta = 30^\circ$), with a relative value equal to $\approx$14%. It is important to mentioning that such a value for θ can be obtained only for very close distances from the Sun (about 2 $R_\odot$), and, then, its contribution

Table 3.1: Four couples of selected observed profiles representing the extreme cases of the considered profile parameters, along with the main information about their features. The inferred relative velocity differences are reported in the bottom.

Line width	
Narrowest (AR 2340) 0.58Å	Broadest April 17, 2009 (CH) 0.87Å
Reversal depth	
Shallowest (AR 2340, no reversal) –	Deepest (QS, Fig. 6a in Fontenla et al., 1988) 69% with respect to the shallowest one)
Asymmetry of the peaks	
$I_{peak-blue}/I_{peak-red} = 1.16$ October 28, 1996 (full disc)	$I_{peak-blue}/I_{peak-red} = 0.86$ (see text)
Separation of the peaks	
Smallest separation (Equatorial CH) 0.38Å	Largest separation April 17, 2009 (polar CH) 0.57Å
Velocity differences	
Observed profiles < 22 km s^{-1} (for those listed above) 100 km s^{-1} (if the flare profile is considered)	Parameterised < 30 km s^{-1} (Auchère, 2005, and IKL)

in the calculation of the H I outflow velocity is limited.

The results reported reveal how little effects the shape of the exciting chromospheric Lyα profile has on the determination of the solar wind H I outflow velocity with respect to the other parameters characterising the Lyα coronal line originating from the resonant scattering mechanism. Therefore, a unique shape of the Lyα chromospheric profile can be adopted all over the solar disc and for an entire solar cycle. Moreover, analytical chromospheric profiles can be used, such as those proposed by Auchère (2005) and Kowalska-Leszczynska et al. (2018), without significantly affecting the solar wind H I velocity estimate.

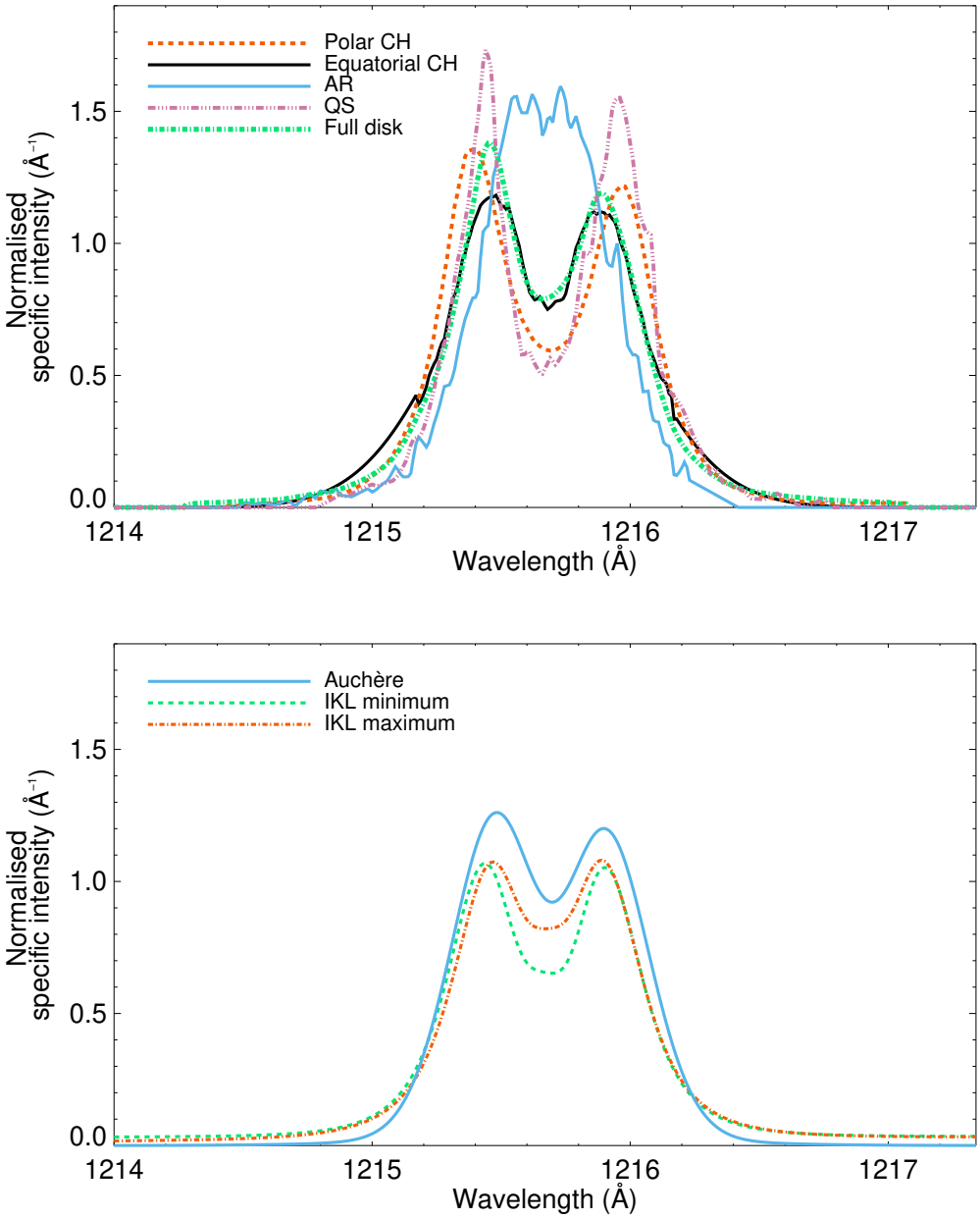

Figure 3.6: Top panel: Lyα irradiance profiles reported in Figs. 6a and 12 of Fontenla et al. (1988) (QS and AR 2340, respectively), as well as profiles observed on April 17, 2009 (polar CH; Tian et al., 2009b), on October 28, 1996 (full disc; Lemaire et al., 2015) and an equatorial CH at the central meridian observed between November 27 and 29, 1975 (Bocchialini & Vial, 1996). Bottom panel: parameterised Lyα profiles from Auchère (2005) and from Kowalska-Leszczynska et al. (2018) (at maximum and at minimum of solar activity). Each profile has been normalised to its total intensity.

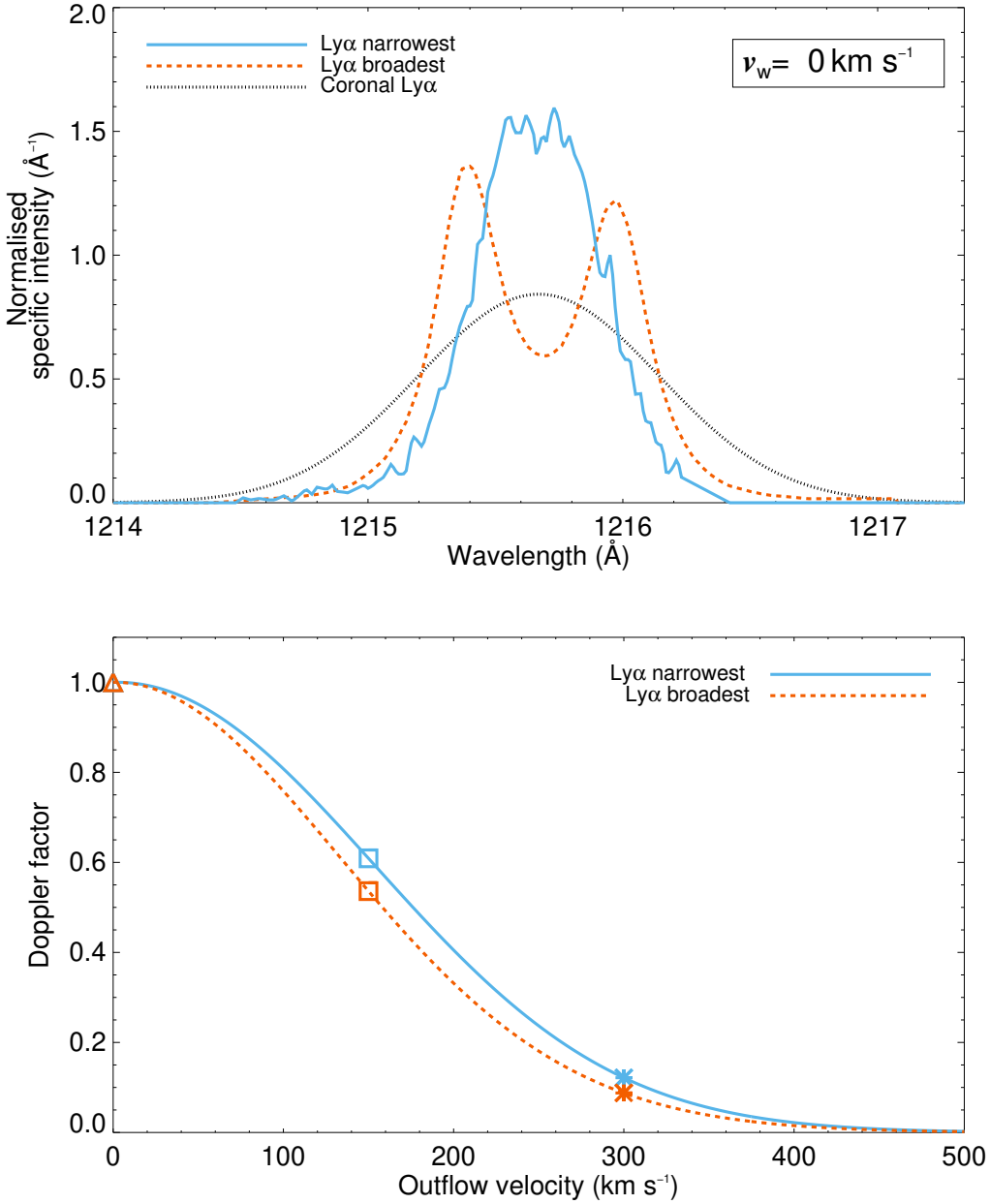

Figure 3.7: Top panel: normalised chromospheric profiles reported in Fig. 12 of Fontenla et al. (1988) (AR 2340, blue solid line) and observed on April 17, 2009 (polar CH, orange dashed line; Tian et al., 2009b), overlapped with a normalised Gaussian coronal profile (black dotted line) computed by assuming a coronal H I temperature equal to 1.5×10^6 K, considering $\theta = 0°$. Bottom panel: Doppler factor as a function of v_w calculated considering each chromospheric profile. Triangles, squares, and asterisks: see Fig. 3.3.

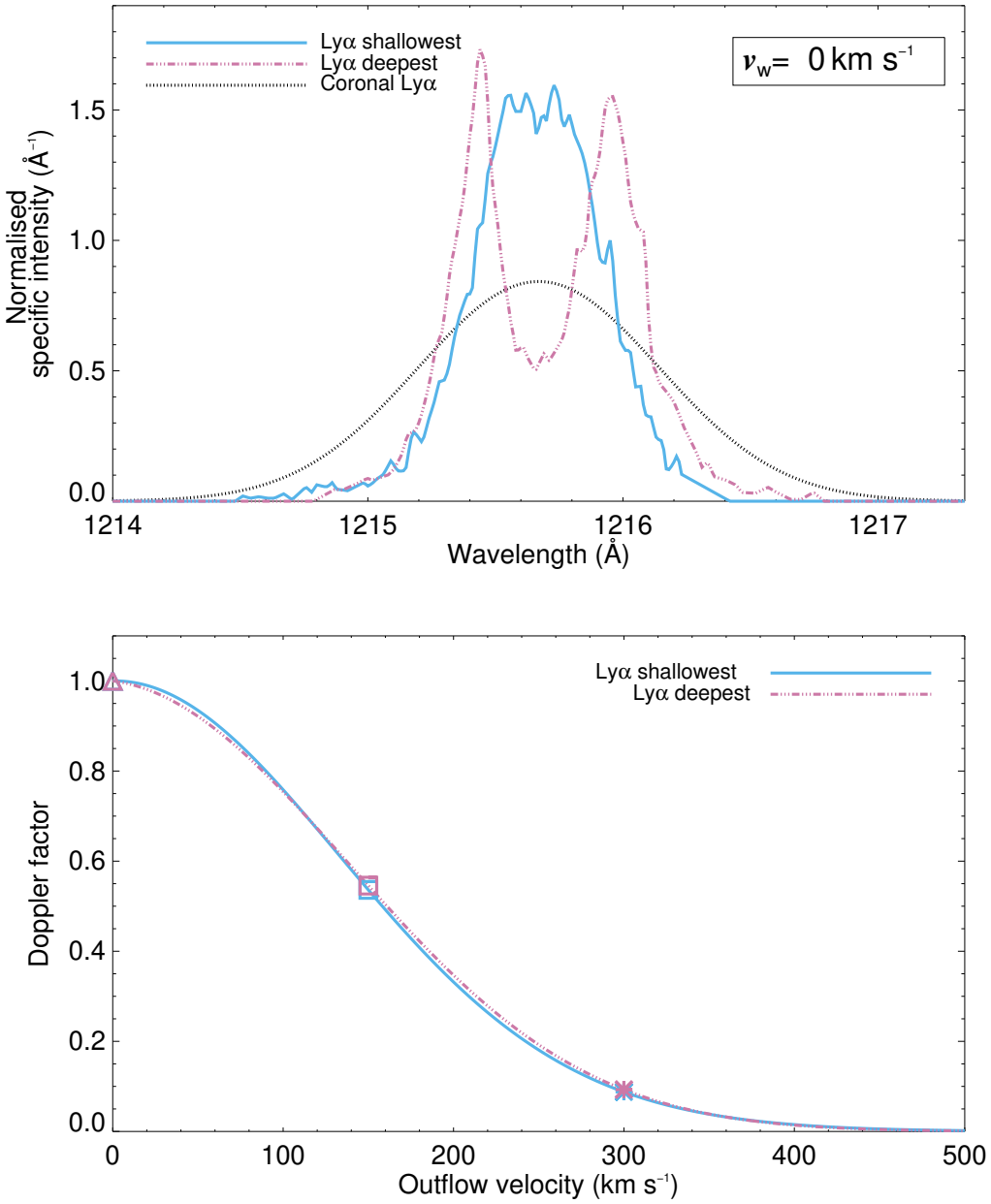

Figure 3.8: Top panel: normalised deepest (QS, magenta dash-dot-dot-dot line) and shallowest (AR 2340, blue solid line) profiles reported in Figs. 6a and 12 of Fontenla et al. (1988), respectively, overlapped with a normalised Gaussian coronal profile (black dotted line) computed by adopting a value for the coronal H I temperature equal to 1.5 $\times$ 10^6 K, considering $\theta = 0°$. Bottom panel: Doppler factor as a function of v_w calculated considering each chromospheric profile. Triangles, squares, and asterisks: see Fig. 3.3.

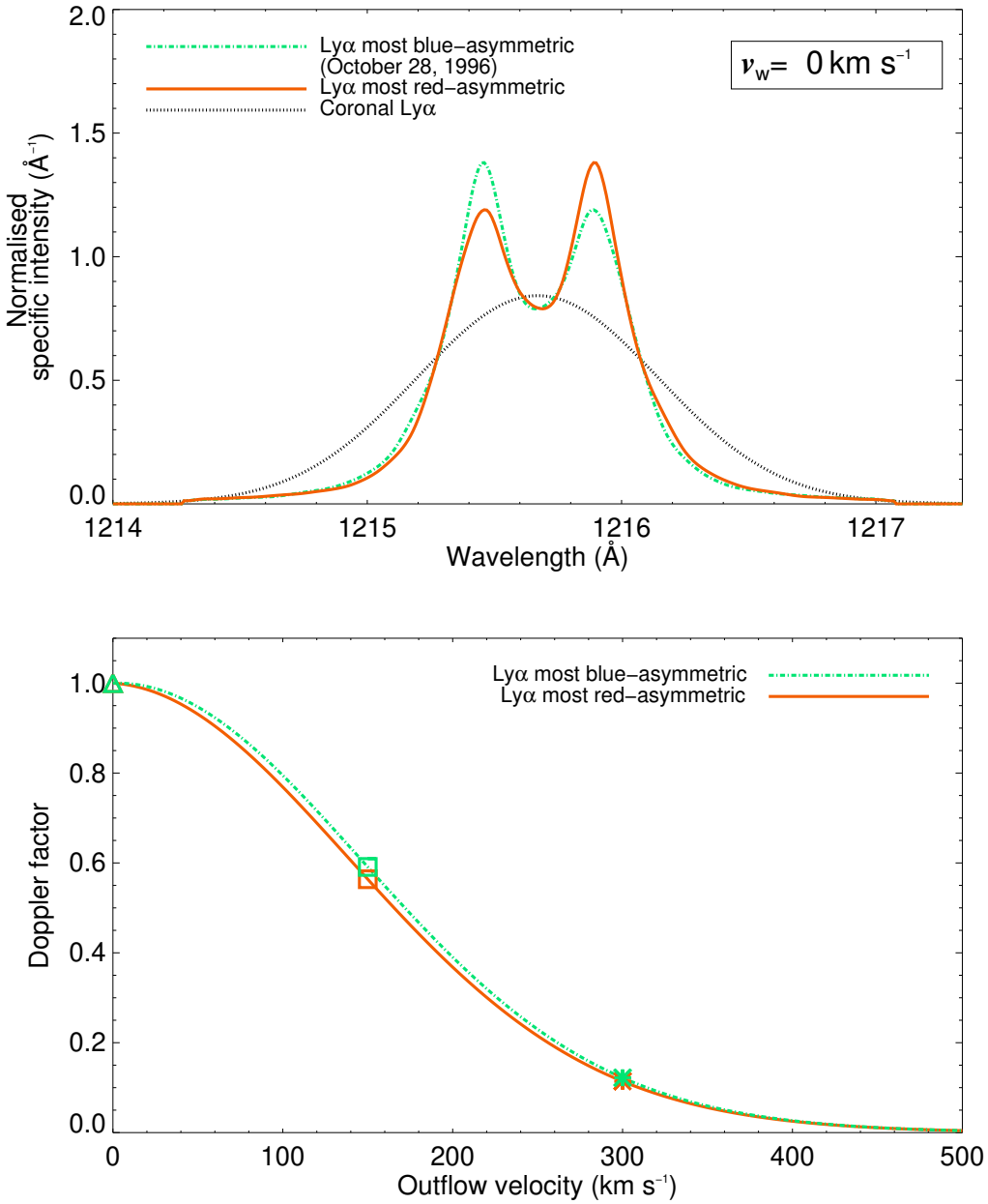

Figure 3.9: Top panel: normalised chromospheric bluest asymmetric profile (full disc; $I_{peak-blue}/I_{peak-red}$ = 1.16) observed on October 28, 1996 (green dash-dotted line; Lemaire et al. 2015) and the reddest asymmetric profile ($I_{peak-blue}/I_{peak-red}$ = 0.86; orange solid line), respectively, overlapped with a normalised Gaussian coronal profile (black dotted line) computed by assuming a coronal H I temperature equal to 1.5×10^6 K, considering $\theta = 0°$. Bottom panel: Doppler factor as a function of v_w calculated considering each chromospheric profile. Triangles, squares, and asterisks: see Fig. 3.3.

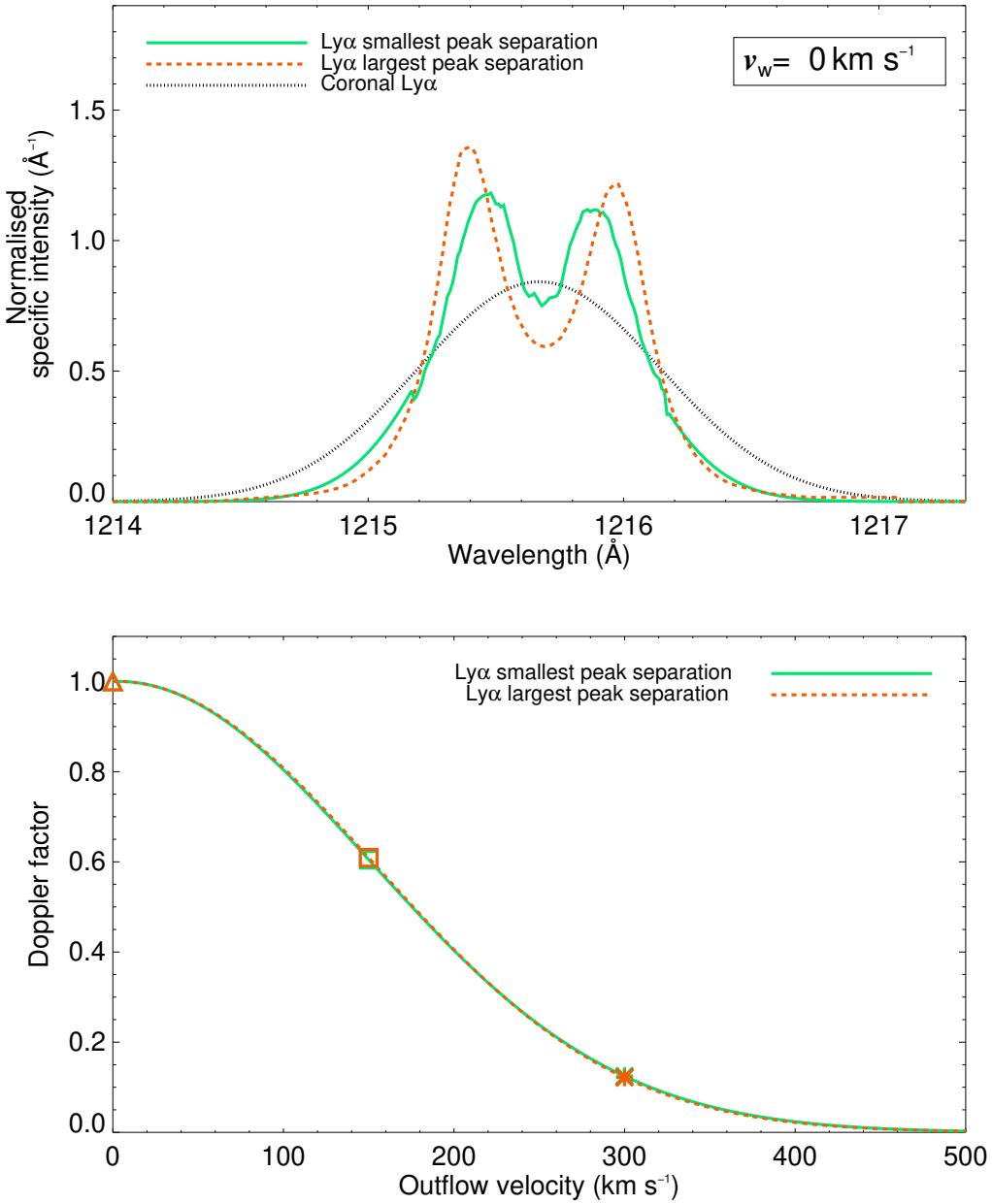

Figure 3.10: Top panel: normalised CH profiles with greatest (orange dashed line) and smallest (green solid line) peak separations observed in a polar CH observed on April 17, 2009 (polar CH; Tian et al., 2009b) and in an equatorial CH at the central meridian on 27-29 November, 1975 (Bocchialini & Vial, 1996), respectively, overlapped with a normalised Gaussian coronal profile (black dotted line) computed by setting the coronal H I temperature at 1.5×10^6 K, considering $\theta = 0°$. Bottom panel: Doppler factor as a function of v_w calculated considering each chromospheric profile. Triangles, squares, and asterisks: see Fig. 3.3.

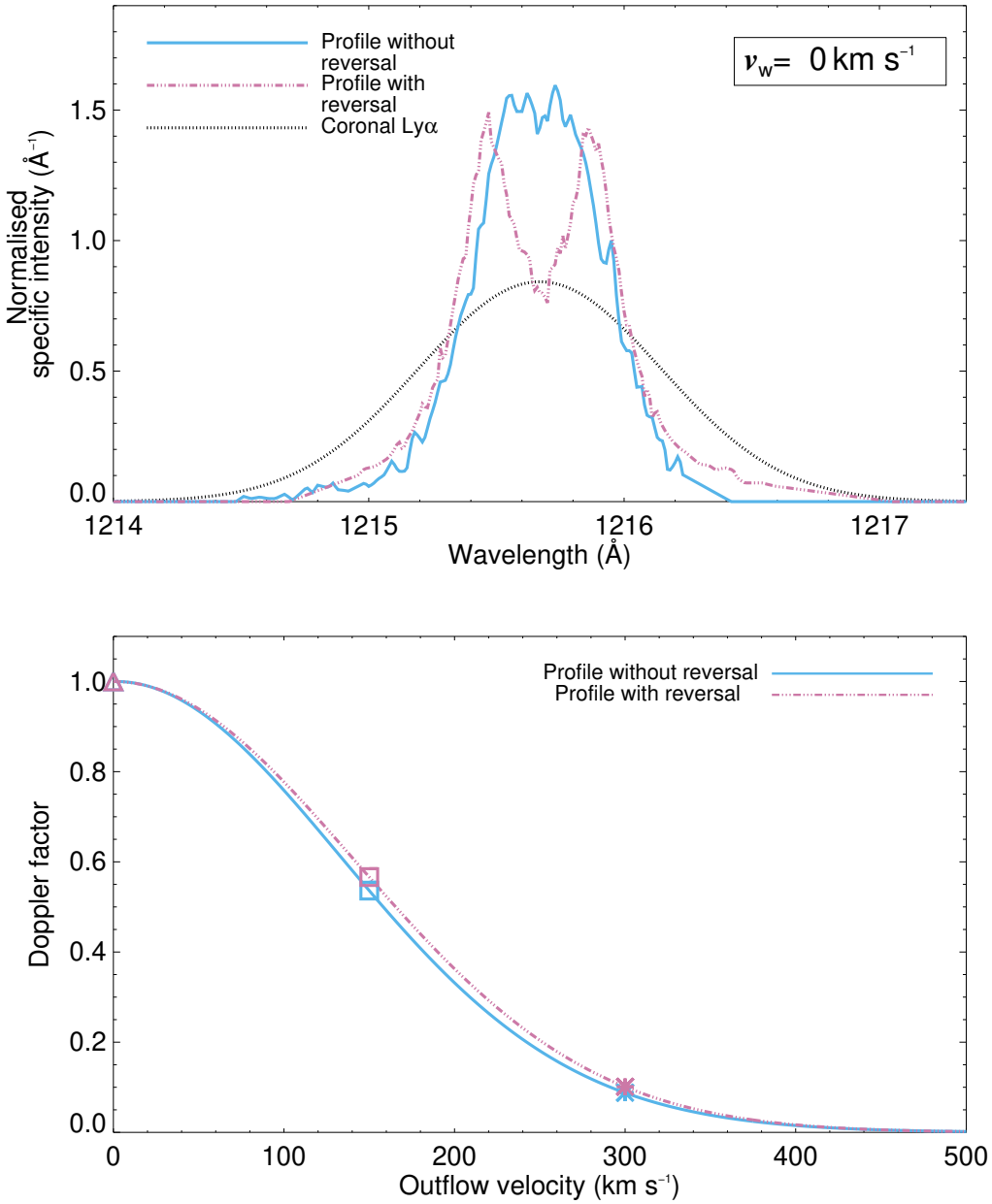

Figure 3.11: Top panel: normalised AR profiles with and without reversal relevant to AR 2363 (magenta dash-dot-dot-dot line; see Fig. 5a of Fontenla et al., 1988) and AR 2340 (blue solid line; see Fig. 12 of Fontenla et al., 1988), respectively, overlapped with a normalised Gaussian coronal profile (black dotted line) computed by assuming a coronal H I temperature equal to 1.5×10^6 K, considering $\theta = 0°$. Bottom panel: Doppler factor as a function of v_w calculated considering each chromospheric profile. Triangles, squares, and asterisks: see Fig. 3.3.

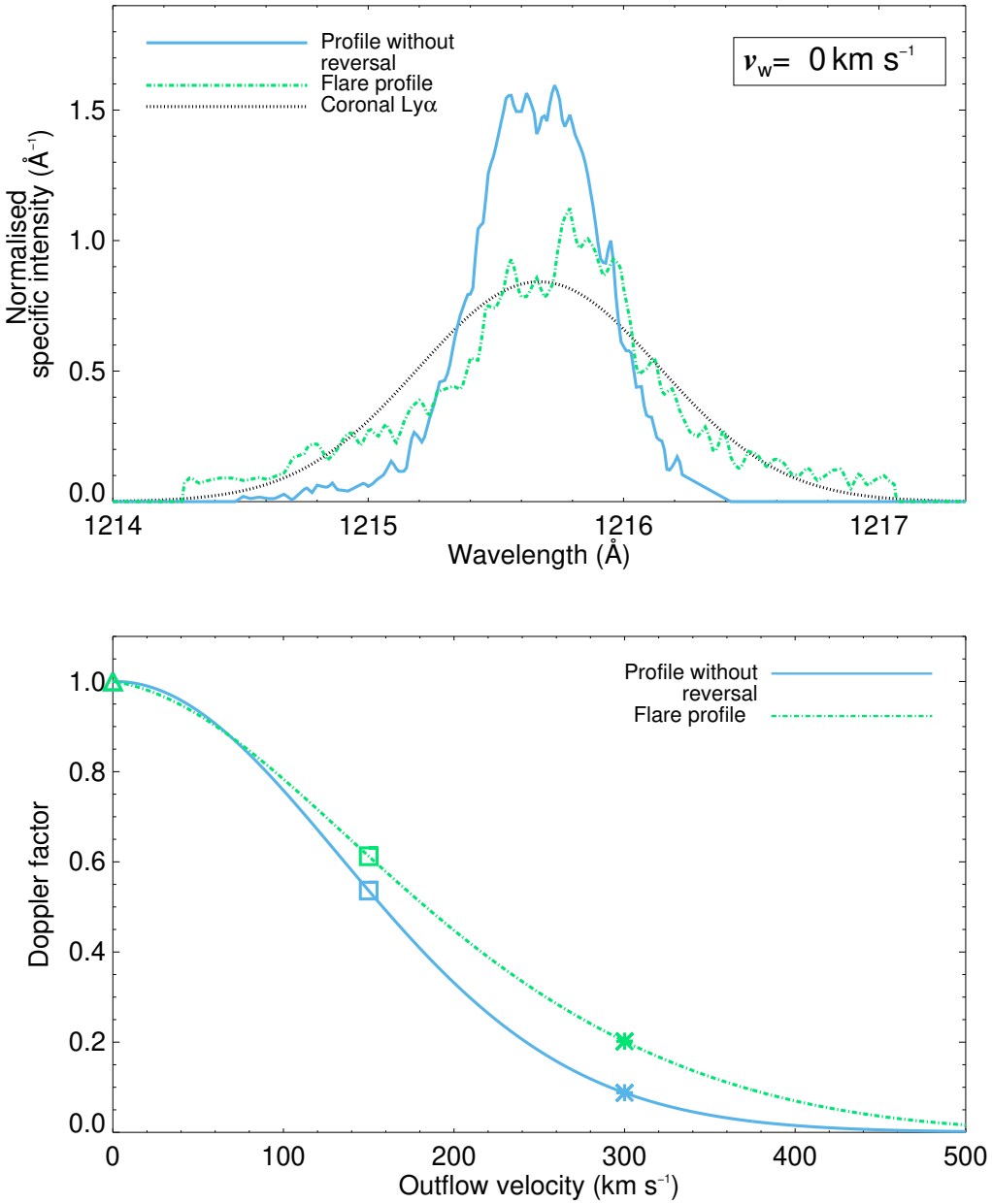

Figure 3.12: Top panel: normalised flare (green dash-dotted line; see Fig. 2e of Lemaire et al., 1984) and AR 2340 (blue solid line; see Fig. 12 of Fontenla et al., 1988) profiles, the latter without reversal, overlapped with a normalised Gaussian coronal profile (black dotted line) computed by assuming a coronal H I temperature equal to 1.5×10^6 K, considering $\theta = 0°$. Bottom panel: Doppler factor as a function of v_w calculated considering each chromospheric profile. Triangles, squares, and asterisks: see Fig. 3.3.

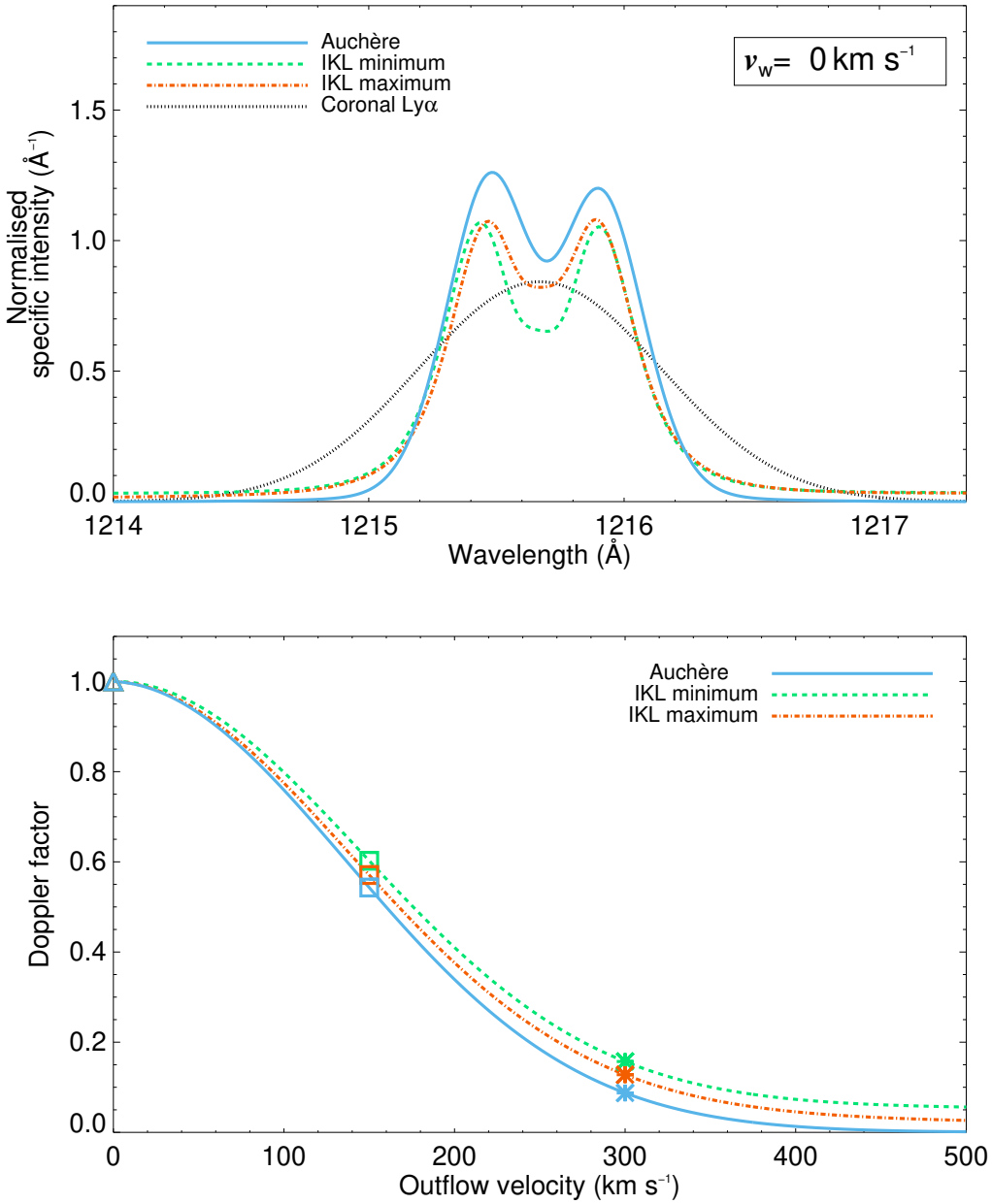

Figure 3.13: Top panel: normalised parameterised chromospheric profiles reported in Fig. 3.6; Kowalska-Leszczynska et al. (2018) (green dashed line at minimum and orange dash-dotted line at maximum) and Auchère (2005) (blue solid line), overlapped with a normalised Gaussian coronal profile (black dotted line) computed by setting the coronal H I temperature at 1.5×10^6 K, considering $\theta = 0°$. Bottom panel: Doppler factor as a function of v_w calculated considering each chromospheric profile. Triangles, squares, and asterisks: see Fig. 3.3.

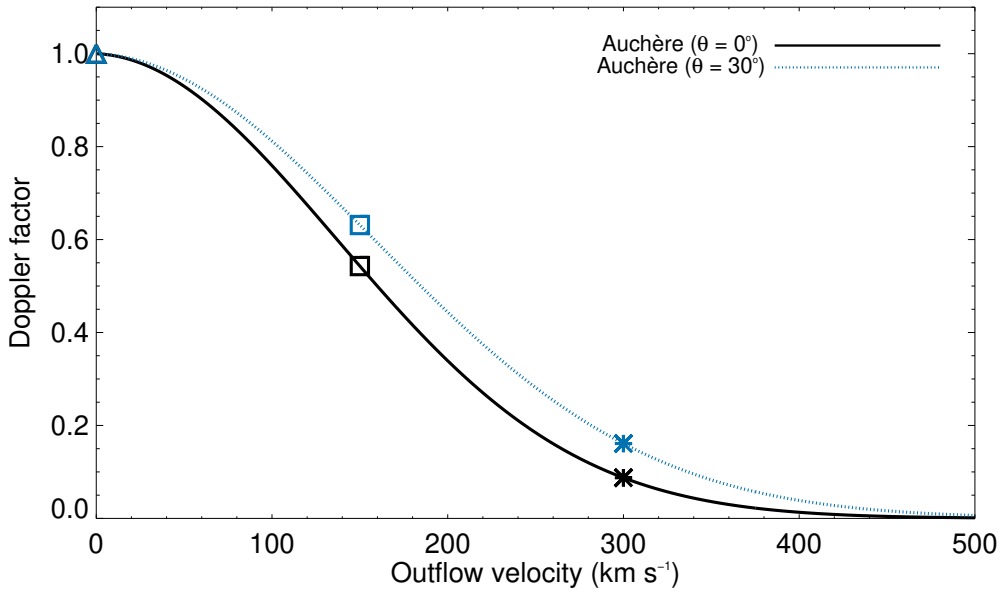

Figure 3.14: Doppler factor as a function of v_w calculated considering the normalised Auchère (2005) profile when $\theta = 0°$ and $\theta = 30°$. Triangles, squares, and asterisks: see Fig. 3.3.

Chapter 4

Metis and its scientific aims

Metis, onboard the Solar Orbiter mission, is the first coronagraph capable to observe simultaneously the coronal UV radiation in a narrow window (15 nm FWHM), centered at 121.6 nm (Lyα emission), and the coronal polarised visible light brightness (VL pB) in the spectral band 580 - 640 nm (Antonucci et al., 2020). The Solar Orbiter mission has been designed to reach a minimum distance from the Sun (perihelion) of about 0.28 au and a maximum distance (aphelion) of about 0.8 au, such that the FoV of Metis is extended from $\approx$ 1.7 $R_\odot$ to $\approx$ 3.6 $R_\odot$ at perihelion and from $\approx$ 4.8 $R_\odot$ to $\approx$ 10.2 $R_\odot$ at aphelion. The Metis performances, combined with the characteristics of the other Solar Orbiter instruments, contribute to provide answers to the following scientific questions (Antonucci et al., 2020; Müller et al., 2020):

- What drives the solar wind and where does the coronal magnetic field originate?
- How do solar transients drive heliospheric variability?
- How do solar eruptions produce the energetic particle radiation that fills the heliosphere?
- How does the solar dynamo work and drive connections between the Sun and the heliosphere?

The answers to these questions can be obtained by investigating the following scientific issues:

- Energy deposition and outflows in the expanding corona.
- Role of magnetic field lines in channelling the coronal wind.
- Coronal fluctuations and their role in the solar wind acceleration.
- Coronal mass ejections and early propagation.
- Eruption of prominences and their propagation in the corona.
- Global evolution of the streamer belt.
- Acceleration of the solar energetic particles (SEPs).

In order to provide a general picture of the instrument properties to the readers of this thesis work, in the following sections the author of this manuscript describes in detail the Metis design and characteristics, its performances and aims, and the data handling and validation procedures.

4.1 Metis coronagraph configuration design

Given the conditions under which the Metis coronagraph works (thermal environment encountered by Solar Orbiter) and the scientific objectives underlined, the instrument was designed to obtain the highest scientific return.

The Metis coronagraph consists of three main units (see Fig. 4.1): the Metis Optical Unit (MOU), the Metis Processing and Power Unit (MPPU), and the Camera Power Converter (CPC).

The role of the MPPU is to control the instrument mechanisms, the thermal hardware on MOU and the power distribution, along with the management of the instrument operations. This unit acquires and processes the detectors data, and interfaces to the spacecraft for instrument power and telecommand (TC), telemetry (TM) and science data transmission. The MPPU executes all the on-board processes, such as frame average, variance, radiation artefacts removal, data compression and packet formatting.

Over the MPPU, the CPC is mounted, and its role is to supply low-voltage power to the detectors.

Finally, the MOU is composed by the external occultation system, telescope, polarimeter, two detectors (UV and VL), and the High Voltage Unit (HVU), which provides high voltage to the UV detector. The detail concerning the Metis optical design are reported in the next subsection.

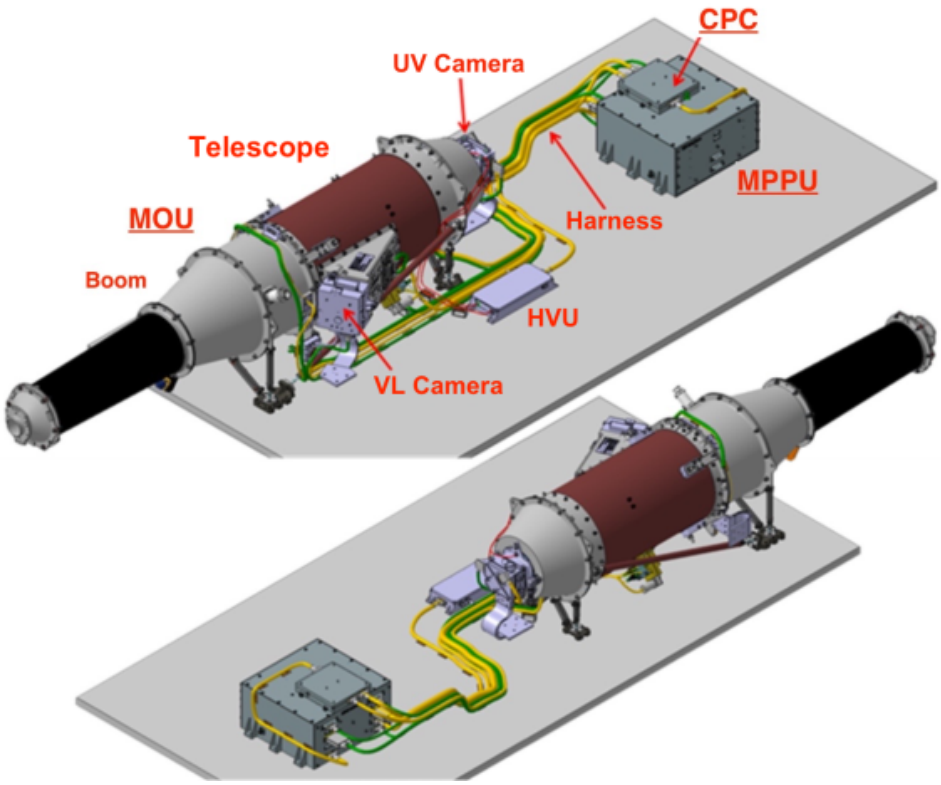

Figure 4.1: Illustration of Metis in its flight configuration, consisting of the Metis optical unit (MOU), the Metis processing and power unit (MPPU), and the camera power converter (CPC). Image adapted from Antonucci et al. (2020)

4.1.1 Metis optical unit

The Metis coronagraph is a wide field telescope characterised by an external occultation system to mask the solar disc (See Fig. 4.2). The coronal light enters through a circular aperture of an inverted external occulter

(IEO), located outside the spacecraft heat shield. The IEO is characterised by a conical shape; this geometry has been chosen to minimise the stray light that enters the instrument. A small M0 spherical mirror back rejects the solar disc light entering the IEO. However, the mirror is characterised by microroughness, so that not all the solar disc light is rejected and a little percentage is scattered. Then, part of the not-rejected solar disc radiation will hit the walls of Metis external buffle. Another remarkable source of stray light is that coming from the IEO aperture edge, which is not stopped by the M0 mirror and enters the instrument along the optical path as coming from a ring-like source. The coronal light, along with the stray light, is collected by an on - axis aplanatic Gregorian telescope, characterised by a primary (M1) and a secondary (M2) mirrors, where each one is concave, ellipsoid and with a central hole. The diffracted light associated to the IEO edge is blocked by the Internal Occulter (IO), where an image of the IEO edge is focused by M1. The diffracted light coming from the M0 mirror edge is removed by a Lyot stop (LS). A field stop (FS) is placed at the focal plane of the M1 mirror, in order to limit the outer FoV, with a further reduction of the stray light. After the reflection by the M2 mirror, the VL and UV paths are splitted by an UV interference filter (IF), positioned at a tilt angle of 12° with respect to the optical axis and composed by an interferential multilayer filter film. This device transmits the UV radiation in a spectral window centered at 121.6 nm and with a FWHM equal to 15 nm toward the ultraviolet detector assembly (UVDA), while the VL is reflected of 24° toward an off-axis polarimeter and, successively, to the visible light detector assembly (VLDA). The UVDA consists of a microchannel plate (MCP) with a photocathode coating of potassium bromide (KBr), which detects UV radiation and transforms it into electrons that are accelerated against a phosphorus screen. The visible radiation emitted by the screen is led onto a CMOS active pixel sensor (APS) STAR1000 (1024 $\times$ 1024 square pixels, each one 15 μm sized) via a fibre optic taper. The VLDA is composed of a custom-made CMOS APS with 2048 by 2048 pixels of 10-µm size each one. Moreover, the UV and VL detectors collect the Metis FoV with a 20 arcsec/pixel and 10 arcsec/pixel scale factor, respectively. The main characteristics of the described optical devices and more details are reported in Antonucci et al. (2020) and Fineschi et al. (2020).

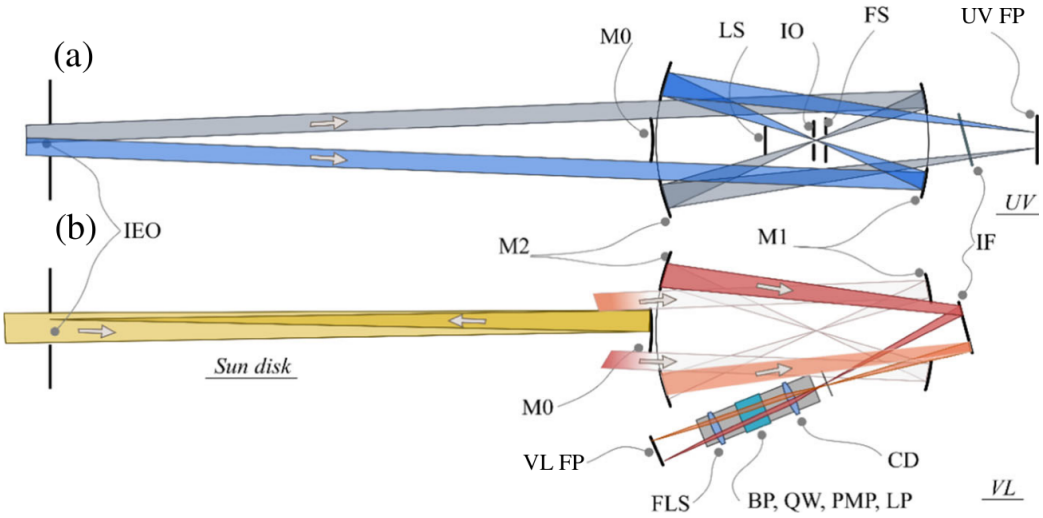

Figure 4.2: a) UV channel; b) VL channel. In the a) panel, the optical path of coronal light is shown, while in the b) panel the optical path of the Sun disc light is also shown. Image adapted from Fineschi et al. (2020)

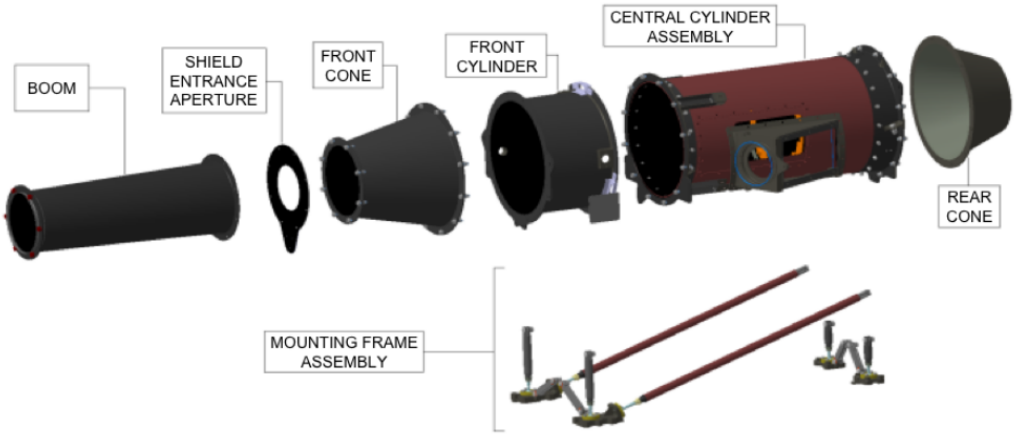

Figure 4.3: Structural parts of the Metis coronagraph. Image adapted from Antonucci et al. (2020).

The alignment of the instrument can be subject to large temperature differences. In fact, the instrument entrance is located on the external panel of the heat shield of the spacecraft, reaching temperatures up to 500 °C. However, the coronagraph detectors have to be held at a temperature

of -45 °C. Thus, in order to avoid this issues, the structure is divided into five sections (see Fig. 4.3):

- Structural boom, which holds the Metis entrance aperture passing through the Solar Orbiter heat shield; this component reaches the highest temperatures.
- Front cone, which introduces a first thermal decoupling.
- Front cylinder, which provides a second thermal decoupling.
- Central cylinder assembly, which holds the large majority of Metis subsystems, including the cooled VL detector.
- Rear cone, which closes the rear part of the instrument and holds the UV detector.

Metis polarimeter

The Metis polarimeter has been designed to detect the coronal VL pB component due to the Thomson scattering of photospheric photons from free coronal electrons, in the spectral band going from 580 nm to 640 nm. In particular, the role of the polarimeter is to collect the light after focusing, perform polarisation measurements and refocus this on the VL detector. The polarimeter works with an $f/4.2$ aperture ratio and returns a paraxial demagnification of 0.67, optimising the spatial resolution (Fineschi et al., 2020). The Metis polarimeter consists of (see Fig. 4.5):

- Collimating doublet (CD).
- Bandpass filter (BP), restricting the instrumental bandpass in the range from 580 nm to 640 nm.
- Quarter-wave plate (QWP) retarder.
- Polarisation modulation package (PMP), composed of two liquid crystals-based variable retarders (LCVRs).
- Linear polariser (LP) acting as analyser.

- Focus lens system (FLS), which projects the polarised image on the VL detector.

The acquisition of four images by setting different setups of the PMP allows to obtain the mesurements of the coronal light polarisation. The nematic liquid crystals variable retarders are optical elements that change the orientation of the molecules of which are composed by applying low voltages (under 10 V; Alvarez-Herrero et al., 2015). This allows to vary the optical retardance of the PMP without any mechanism. The polarimeter follows the de Sénarmont compensator configuration (Sénarmont, 1840), which couples the QWP with a 180° rotating analyser (this latter given by a combination of the LCVRs and LP relative orientation). Taking into account a right-handed reference frame with the z axis oriented along the light propagation direction and the x axis parallel to the polarisation axis of the LP component, the fast axis of the QWP is parallel to the y axis, and the fast axis of the LCVR is tilted by -45° with respect to the x axis (see Fig. 4.4). Setting the PMP optical retardance at 90°, 180°, 270°, and 360° with respect to the initial PMP fast axis direction, the Stokes vectors of the observed radiation can be measured.

4.2 Metis coronagraph performances and its aims

Metis observations consist of global maps of the coronal emission built simultaneously in the H I Lyα and in the 580 - 640 nm VL pB spectral window. Another important characteristic of Metis is its high temporal and spatial resolution. In particular, the instrument is capable to acquire coronal images with a minimum temporal cadence equal to 1 s, and with a spatial resolution down to about 2000 km and 4000 km in the VL an UV channels, respectively. Obviously, different resolutions can be used depending on the scientific aim. The FoV is characterised by an internal boundary of 1.6°, due to the combined action of the IO and the LS, and an external boundary delimited by the FS and the detector size. The former limits the FoV until a $\pm$ 3.4°, while the latter delimits a square of $\pm$ 2.9°. The instrument can reach a minimum distance of 0.28 au (perihelion) and a maximum distance of about 0.8 au (aphelion). This means that at the perihelion the FoV extends from 1.7 $R_\odot$, very close to the Sun surface, to

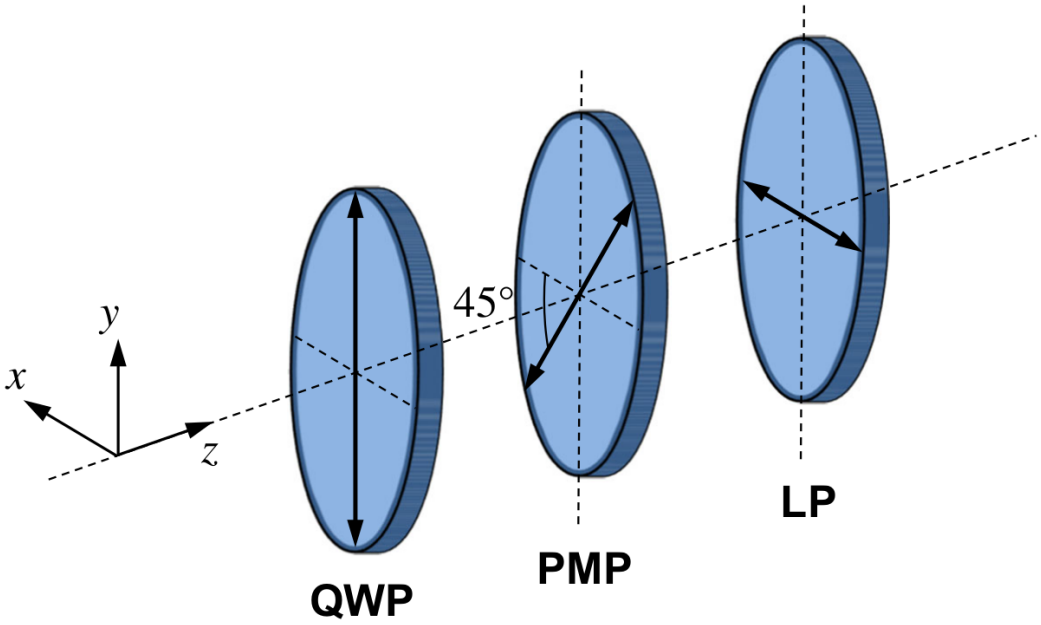

Figure 4.4: Scheme of the relative orientation of the Metis polarimeter. The arrows indicate the fast axis of the QWP and PMP, and the polarisation axis for the LP. Image adapted from Fineschi et al. (2020).

3.0 - 3.6 $R_\odot$, while at the aphelion the FoV ranges between 4.8 $R_\odot$ and 8.7 - 10.2 $R_\odot$.

As explained in Section 3.3, the combination of H I Lyα data and of the electron density distribution (the latter deduced from pB observations; see Section 3.2) allows to apply the Doppler dimming technique to infer the outflow velocity of the solar wind. The detailed Metis observations of the Lyα and pB radiation permit to determine the wind velocity gradient and to identify where and at which rate the energy deposition occurs in the solar corona, and, then, to discriminate between fast and slow solar wind.

The observation of VL pB allow to outline the coronal magnetic features, and the outflow investigation helps to associate the topology of the magnetic field with the wind regime and to understand how the magnetic field regulates the solar wind speed, going deeper in the study of the origin and sources of the solar wind. During the near-perihelion phases, not only the Metis FoV inner edge goes closest to the low corona, but the

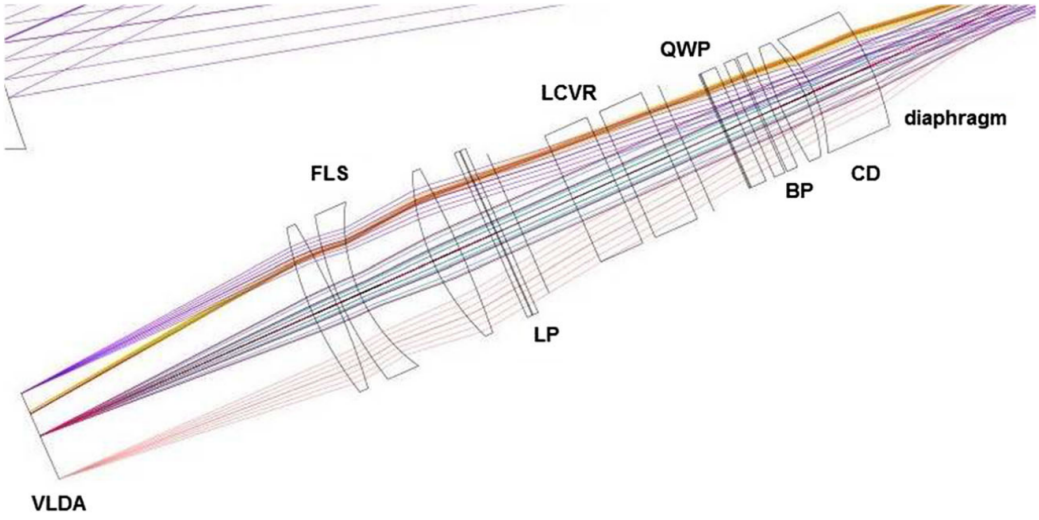

Figure 4.5: Schematic view of the Metis polarimeter, composed of the following elements: a collimating doublet (CD), a bandpass filter (BP), a quarter-wave plate (QWP) retarder, a polarisation modulation package (PMP) composed of two liquid crystals-based variable retarders (LCVRs), a linear polariser (LP), and a focus lens system (FLS). Image adapted from Fineschi et al. (2020).

orbital motion of the spacecraft with respect to the solar surface is slower that at 1 au, favouring the investigation of the intrinsic evolution of the solar corona, also observing open field lines separating sub-streamers.

The high resolution of the data should represent a tool for the observation of transient and intermittent phenomena that can give an important contribution in the origin of the slow wind, such as the plasma blobs generating in the cusp of the helmet streamers (Sheeley et al., 1997). Also pseudo-streamers and the corresponding plasma sheets that separate same-polarity regions can be observed at high resolution, investigating their role in the origin of the solar wind.

The nature of coronal fluctuations can be probed with this instrument, investigating their origin, how they connect with the dynamics of the photosphere, their role in transferring energy from the inner corona to the regions where the solar wind accelerates, how they evolve from the corona to the interplanetary space, and to discriminate between fluctuations originating from the rotation of magnetic flux tubes and those ascribed to wave propagation and inhomogeneities carried by the wind. Observa-

tions of the coronal fluctuation have been made by SOHO/UVCS in the polar CHs (Ofman, 1997, 2000; Bemporad et al., 2008) and in the slow wind (Telloni et al., 2009), and by STEREO/COR coronagraphs through white-light images going radially up to 4 $R_\odot$ (Telloni et al., 2013, 2014).

For what concerns the CMEs onset and propagation, the joint science of Metis with the EUI instrument onboard Solar Orbiter provides detailed information on the regions where the eruption and the early propagation of the CMEs occur, along with the eventual relative eruptive prominence evolution. The spatial evolution of the structure and the reconfiguration of the solar corona in response to a CME can be followed and investigated when observations at 1 au with other joint instruments are considered (for example, with LASCO C2 and C3 coronagraphs onboard SOHO). The out-of ecliptic vantage point will offer for the first time observations of the corona from mid-latitudes and will allow to investigate the longitudinal structure and distribution of propagating CMEs. These events can be important for the global evolution of the streamer belt, and the out-of ecliptic view will allow to investigate the longitudinal extent of coronal features from a lightly warped streamer belt during the minimum of solar activity, to a more complex structure near the maximum of activity.

Finally, the instrument permits to discriminate between flare accelerated SEPs and those related to CME events, by taking into account the large variations of their physical properties from one event to another. In fact, the radio emissions due to shock-accelerated electron beams manifest by type II bursts, and the timing of these events allows to identify the shock produced by the passage of a CME (Mancuso & Bemporad, 2009).

The activity of Metis will be complemented with the simultaneous contributions coming from other space missions dedicated to the heliophysics, such as PSP, the BepiColombo (Benkhoff et al., 2010), Proba-3, ASO-S, and Aditya-L1.

In summary, the performances of the Metis coronagraph and the high quality of the data provided by the instrument allow to obtain detailed results about the solar wind onset, acceleration, and heating, also taking into account the occurrence of transient events, and to correlate them to the solar magnetic field, investigating the evolution of the outer solar atmosphere and the connection between the Sun and the heliosphere. The first results are reported in Chapter 5, provided by the Metis first light,

the first quadrature between SolO and PSP, and the first CME observed with Metis.

4.3 Data acquisition, transmission and handling

The polarised brightness acquisitions consist of frames delivered at a constant rate at four different polarisation angles. These frames are processed for CRs and SEPs removal, statistic analysis and CME monitoring, and those with the same polarisation are averaged. Indeed, the total VL brightness (tB) can be extracted setting the polarisation angle only to two positions. In this case, all frames are acquired at a constant rate, switching the polarisation angle in the middle of the detector integration time (DIT), and successively are averaged. If the polarisation angle position is maintained fixed to obtain single polarisation data, acquisitions at high rate can be performed. In this configuration, the monitoring of the CMEs and solar disc is disabled. The correction of CRs and SEPs is also disabled, because there are not frames to be summed.

The ultraviolet acquisition can be distinguished into two configurations: the photon-counting and analogue modalities. The former allows to detect each single observed photon by increasing the gain voltage. Indeed, the latter, at lower voltages, permits to acquire an analogue signal proportional to the flux of the arriving photons.

In the aforementioned cases, the final images are compressed and sent to ground at a specific cadence. Once the in-flight telemetry are received by the Science Operation Centre (SOC) through the Mission Operation Centre (MOC), the data are distributed to the instrument team. The science data pipeline produces scientific products at different levels. First of all, the pipeline combines the telemetry packets of each data product, decompresses the data when it is necessary, and returns the not calibrated FITS level 0 (L0) data. Therefore, the header data, necessary for the calibrations, are decoded by the pipeline and used in order to produce the level 1 (L1) data. Finally, the pipeline calibrates the data to physical units, and converts onboard time to coordinated universal time (UTC) and the instruments coordinate system to the world coordinate system (WCS; for example, see Greisen & Calabretta, 2002; Thompson, 2006). The final cali-

brated data are available for the scientific community as level 2 (L2) data. The physical units used to produce L2 data are photons cm^{-2} s^{-1} sr^{-1} and MSB (Mean Solar Brightness) for the UV and VL data, respectively. The latter unit is equivalent to 4.67 x 10^{20} photons cm^{-2} s^{-1} sr^{-1} in the visible spectral band in which Metis observes.

Because of the different distances between the spacecraft and the Sun during the mission, the data downlink capability can experience significant changes, with latencies retrieval that can exceed 100 days. Furthermore, the payload telemetry is organised by different priorities: the first data to be received to ground are the housekeeping data, while the last are the science data. To minimise the data latency, a set of low-latency data is downlinked at each ground contact, consisting of two VL and one UV images highly compressed, in order to comply with the limit of 1 MB/day allowed for each instrument onboard Solar Orbiter. Moreover, the VL channel can provide light curves relative to eight temporal series of mean brightness obtained by averaging the counts of the pixels detected in eight radial sectors selected on the FoV. The function of low-latency data is to give an overview of the data relative to the last ground contact, to monitor the instrument performances, to check the science data quality, and to change future planning if necessary.

4.3.1 Metis data validation

The data validation activity, where the author of this thesis has given significant contributions, consists of four main steps and accessory data for investigations:

- Check for telemetry, telecommand and data produts errors, discrepancies and anomalies.
- Data volume check.
- Door status.
- Off-pointings and image features investigation.

The Metis observations are scheduled along each orbit into three ten-day intervals, called Remote Sensing Windows (RSW). The observations

sessions are subdivided in Long Term Plannings (LTP), with a duration of the order of month. A LTP is characterised by several Short Term Plannings (STP), each one including up to 10 days of acquisitions.

For what concerns the first step, the scope of this verification is:

- Check for TM errors that might have modified the planned observations or notified out-of-limits errors or warnings.
- Check if images are missing (both L0 and L1).
- Check if images are corrupted (L0).
- Check for missing or retransmitted packets not visible in the images.
- Verification of light curves, low latency data and log matrices.
- Presence of other anomalies.

In the second step, the data volume must be confined within a telemetry corridor timeline provided by the SOC for each LTP. Then, the scope of this step is to compare the effective data volume with the predicted one.

In the third step, the door status check, other than a simple functional verification, allows to record the open/closed cycles of the door, because the number of cycles is limited.

In the last step, off-pointing and image features are checked by using a quick look tool written in IDL and in Python programming languages, which allows to view L0 images in order to check in detail each single image and to perform running differences and movies to record remarkable intensity variations, important for the identification of CME occurrences. Finally, the functionalities of the tool are used to check if the instrument is in an off-pointing position and to verify the presence of particular features, such as stars, planets, comets, debris, CRs and SEPs.

Chapter 5

First results

In this chapter, the first results provided by the analysis of data obtained with the Metis coronagraph are reported, where the aforementioned diagnostics techniques have been used. In particular, the first light of Metis has been considered to study in detail the solar wind configuration at the rising of solar activity cycle, also exploiting detailed information about the solar corona structure obtained with a 3D MHD model of the Predictive Science Incorporated (San Diego, California). Simultaneous observational campaigns have been performed with the SolO and PSP spacecraft during their first quadrature, extending the solar wind investigation up to about 22 $R_\odot$. Finally, the Metis performances allowed to study in detail the first CME observed with the instrument, showing how Metis is also capable to give important information on the onset and evolution of coronal transient events. All these results, described in the following sections, are reported in the works of Romoli et al. (2021), Antonucci et al. (2023), Telloni et al. (2021), and Andretta et al. (2021), where the author of this thesis gave remarkable contributions concerning the data analysis and the writing.

5.1 Metis first light observation of the solar wind

The first light of Metis was observed on May 15, 2020 (minimum of solar activity), providing simultaneous H I Lyα (121.6 $\pm$ 10 nm) and VL pB (580 - 640 nm) images of the extended corona with high spatial and temporal

resolution (down to 2000 km and 4000 km at perihelion in the VL and UV channels, respectively, and a minimum temporal cadence equal to 1 s; see Chapter 4 for more details). The aim of this analysis is the study of the outward propagation of the solar wind in the inner corona at the rising of solar activity cycle (see Romoli et al., 2021). In particular, the author of this thesis performed the radiometric calibration of the UV data and the analysis concerning the solar wind outflow velocity and the coronal electron density determination.

During the coronal observations, SolO was at 0.64 au. The line that separates SolO by the Sun was forming an angle of 11.4° W relative to the Earth-Sun direction, and the spacecraft was at 4.3° N with respect to the solar equatorial plane. During the acquisition activity, at the aforementioned distance of the spacecraft from the Sun, the FoV was extended from 3.8 $R_\odot$ to 7.0 $R_\odot$. The observations were performed in the time interval 11:39 - 11:41 UT. In particular, the selected pB image was obtained by combining polarimetric images with DIT = 30 s, while the corresponding H I Lyα image was obtained by averaging six frames with DIT = 16 s. The author of this thesis calibrated the acquired UV data by considering the measured UV intensity of the α Leonis star in the region of transit across the Metis FoV. In particular, the region of interest, where the transit occurred, is the equatorial sector of the corona at the East and West limbs, within a latitude of $\pm 20°$, where the observed streamers were quasi-equatorial structures in the VL and UV channels (see Fig. 5.1).

The West streamer in the images shows a double structure, more complex than that extending at the East limb, probably due to the occurrence of transient phenomena at the time of observation or to a more warped streamer belt. In fact, LASCO-C2 images show the presence of a blob observed at the West limb on May 15, 2020, at 11:36 UT (see Fig: 5.2). Due to the slight angular separation between the POS identified by Metis and LASCO-C2 (11.4°), the blob was entering in the Metis FoV, and this may have contributed to the more complex structure of the West streamer. These factors have determined the choice to concentrate the analysis to the simplest and more clear East streamer structure.

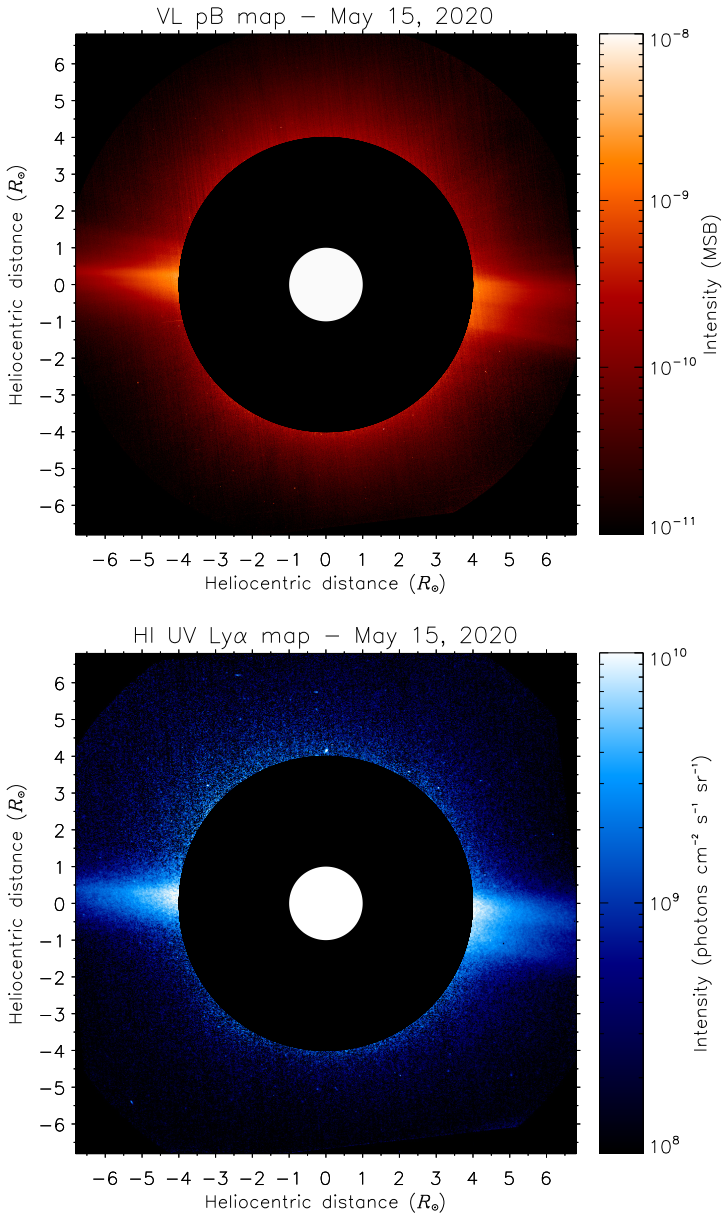

Figure 5.1: Coronal pB (top) and H I UV Lyα (bottom) images acquired with Metis on May 15, 2020 (first light), at 11:39 UT. The white filled circle identifies the solar disc.

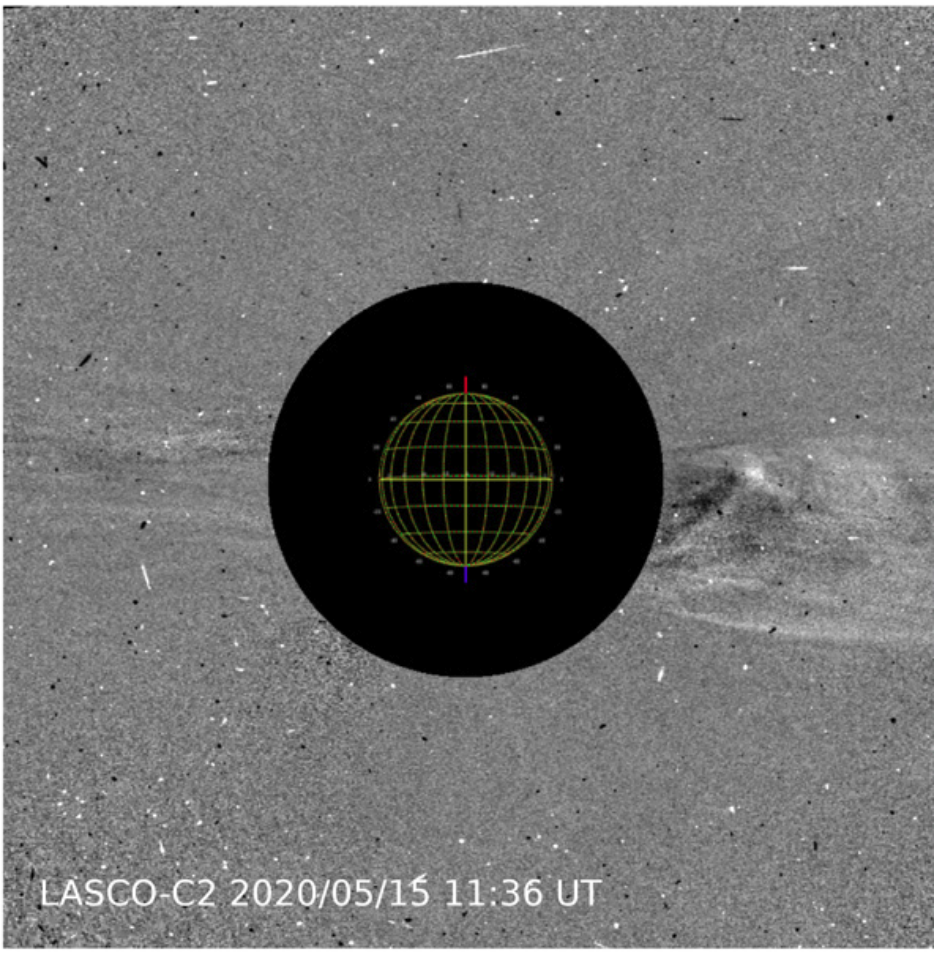

Figure 5.2: Coronal blob observed at the West limb with SOHO/LASCO-C2 on May 15, 2020, at 11:36 UT. The structure is highlighted by a difference of images. Image adapted from Romoli et al. (2021).

The selected coronal images obtained with Metis were used by the author of the present manuscript to proceed with the application of the Doppler dimming technique for the determination of the outflow velocity of the neutral hydrogen atoms in the analysed region. Until about 10 $R_\odot$ the rate of charge exchange between hydrogen atoms and protons is high (see, for example, Olsen et al., 1994; Allen et al., 1998), so that the neutral hydrogen flow velocity is representative of the proton velocity, which is the principal coronal component, and, thus, allows to have a

good estimate of the solar wind velocity.

To achieve this purpose, the synthetic Lyα intensity, which depends on several parameters described in Chapter 3, is compared with the observed one, and the velocity is obtained by iteratively changing it until a satisfactory match between the compared intensities is reached. The algorithm used in this way is illustrated in Dolei et al. (2018, 2019) and Capuano et al. (2021), and the developed tool for the neutral hydrogen solar wind velocity determination is reported in Appendix B. To infer the synthetic Lyα intensity, the following assumptions were considered.

The pB first light were used by the author of this manuscript to derive the electron density through the application of the Van De Hulst (1950) inversion method (see Section 3.2). The tool based on this technique is reported in Appendix A. In Fig. 5.3 (top panel) the inferred density is shown as a function of the polar angle (PA), where the latter is zero at the north pole and increases going counterclockwise (for example, PA = 90° at East and along the equator). The density structure in the corona is highlighted by the observed polarised brightness trend as a function of the latitude (see Fig. 5.3, bottom panel). In particular, both the pB and the electron density are characterised by values greater than the $1/e$ of the maximum value in an angular sector with an amplitude of about $\pm 10°$. The quasi-symmetric layer of denser plasma is observed at the center of the projection on the POS of the surface dividing positive and negative polarity field lines of the coronal magnetic field, where the latter shows a quasi-dipolar configuration during the time of observations. On the axis of the current sheet, which is located few degrees toward the North pole with respect to the equator, the electron density varies from 1.6×10^5 cm^{-3} to 0.45×10^5 cm^{-3} at 4.0 $R_\odot$ and 6.8 $R_\odot$, respectively. Over about $\pm 10°$, the density tends to be flatter and approaches typical coronal hole values (see Spadaro et al., 2017), with the northern wing more structured then the southern one.

The adopted electron temperature follows the analytical expression derived by Gibson et al. (1999) for the equatorial regions, with values going from 0.7×10^6 K to 0.4×10^6 K at 4.0 $R_\odot$ and 6.8 $R_\odot$, respectively.

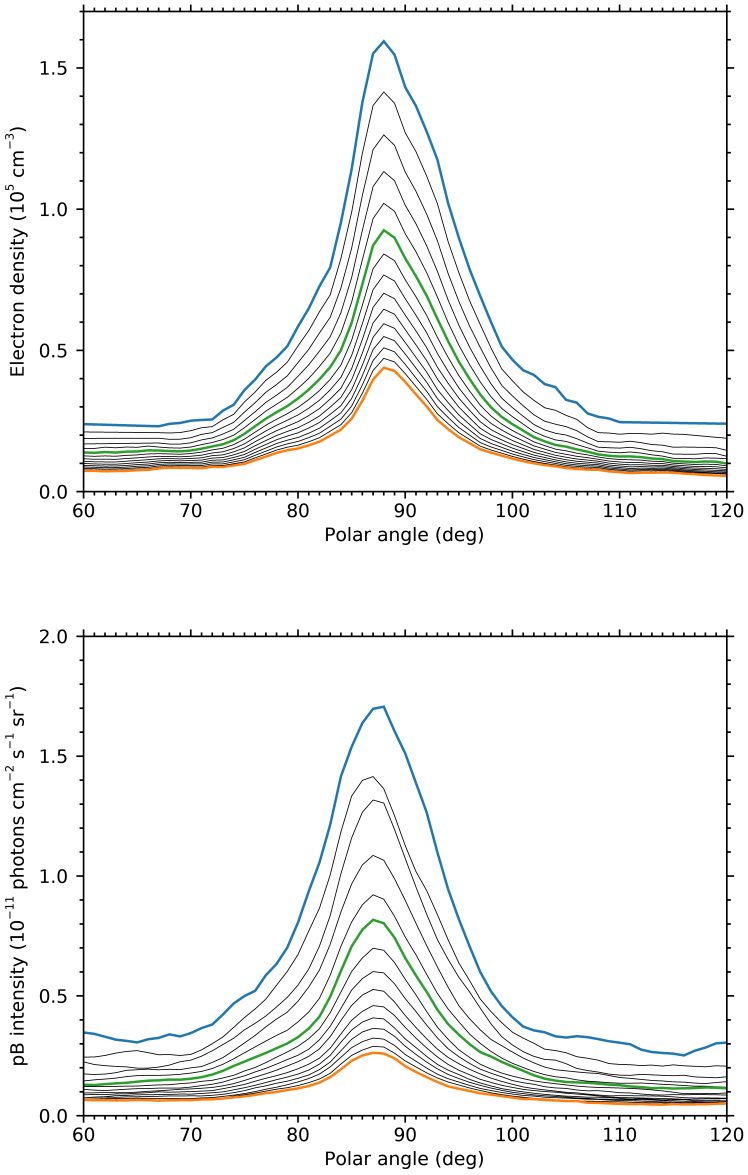

Figure 5.3: The coronal electron density (top panel) inferred by the pB observed with Metis on May 15, 2020 (bottom panel), under the hypothesis of a cylindrical corona and by applying the Van De Hulst (1950) inversion method. Both the panels show the profiles as a function of the polar angle. The curves are shown at step of 0.2 $R_\odot$, going from 4.0 $R_\odot$ to 6.8 $R_\odot$. The blue, green, and red lines indicates the profiles inferred at 4.0 $R_\odot$, 5.0 $R_\odot$ and 6.8 $R_\odot$, respectively. Panels adapted from Antonucci et al. (2023).

For what concerns the coronal H I temperature, the anisotropic and isotropic scenarios were considered in the analysis. In the isotropic case, the same constant temperature was adopted all over the selected coronal region for both the directions parallel and perpendicular to the assumed radial coronal magnetic field, which means $T_{HI,\perp} = T_{HI,\parallel} = 1.6 \times 10^6$ K. In the anisotropic case, the perpendicular temperature $T_{HI,\perp} = 1.6 \times 10^6$ K and the parallel temperature $T_{HI,\parallel} = T_e$ were adopted.

The excitation chromospheric Lyα intensity used along with the chromospheric Lyα profile to excite the H I coronal atoms was considered uniform all over the solar disc, with a value equal to 8.16×10^4 erg cm^{-2} s^{-1} sr^{-1}, that is 5.0×10^{15} photons cm^{-2} s^{-1} sr^{-1}, obtained with the UARS/SOLSTICE instrument (see Lemaire et al., 2015). The associated exciting profile is the analytical one proposed by Auchère (2005), where the author of the paper reproduces a typical solar minimum profile performing a sum of three Gaussian profiles (see Section 3.3.3).

These quantities allow to calculate the synthetic emissivity in each point of the space in the coronal sector selected for this analysis. Fixed a point in the POS, the intensity is given by the sum of the emissivity contributions coming from each infinitesimal volume along the LOS. Then, to infer the synthetic intensity, the obtained synthetic emissivity has to be integrated along the LOS. For this analysis, the author of this thesis integrated the synthetic emissivity along the LOS in a range of 10 $R_\odot$, that is ± 5 $R_\odot$ around the POS. The same range was considered to apply the van de Hulst inversion method to the first light pB data.

To increase the signal to noise ratio (S/N) of the observed UV image, a 4×4 binning was performed by the author of this manuscript, reaching S/N values greater than 5 in a region of $\pm\ 20^\circ$ with respect the equatorial streamer belt. Then, this angular sector was chosen for the analysis.

Once the Doppler dimming technique was applied on the first light data, and considering the aforementioned conditions, it has been found that the velocity values obtained in the isotropic H I temperature case are higher of about 40 km s^{-1} with respect to those inferred in the anisotropic scenario, all over the field considered. In particular, in the equatorial sheet, and in the anisotropic H I temperature case, the velocities are almost uniform, with values of about 160 ± 18 km s^{-1}. The values tend to increase out of the equatorial region. In particular, those at ± 0.2 $R_\odot$,

± 0.4 $R_\odot$, ± 0.6 $R_\odot$, and ± 0.7 $R_\odot$ from the equatorial plane and for the anisotropic H I temperature can be deduced from Fig. 5.5. For example, at ± 0.7 $R_\odot$ from the equatorial plane and at 6.0 $R_\odot$ in heliocentric distance, the velocity varies from 210 km s^{-1} to 185 km s^{-1} in the southern and northern borders, respectively. Going toward higher latitudes, beyond the high density sheet, a velocity gradient of tens of km s^{-1} deg^{-1} is observed, defining the transition from the slow to the fast wind.

The found velocities can be compared with those obtained by UVCS observations. In particular, the slow wind was measured along a streamer axis through the doublet O VI 1032 Å and O VI 1037 Å, obtaining about 100 km s^{-1} (for example, see Frazin et al., 2003). During the declining phase of activity of cycle 23, Susino et al. (2008) studied a middle latitude streamer observed with UVCS, finding that at 5.0 $R_\odot$ the O VI ions flow at higher velocity with respect to the hydrogen atoms (135 km s^{-1} and 60 km s^{-1}, respectively). In an equatorial streamer observed with UVCS on 2008 (minimum of activity), Dolei et al. (2015) found an higher hydrogen velocity, that is 140 km s^{-1}. In general, from several studies, it turns out that the O VI ions are faster than H I atoms, suggesting a different energy deposition rate in the solar wind acceleration region for the two species at all the latitudes and during different phases of solar activity.

An update of the work of Romoli et al. (2021) has been carried on by Antonucci et al. (2023), with the aim to derive the fine structure of the solar wind density and velocity as a function of the latitude, to study the structure of the slow wind zone in the quiet corona out to the boundary between slow and fast solar wind, and to discuss the properties of the slow wind in terms of the magnetic field topology, that is, of the expansion of the coronal magnetic field lines and of the physical factors characterising the separatrix web in the solar atmosphere. In order to reach this goal, a refined approach of the Doppler dimming technique applied to Metis data was introduced (see Appendix B), in order to consider the best approximation of the polarised emissivity distribution and coronal density for the moderate warping of the equatorial plasma sheet along the LOS (see Fig. 5.6), through a 3D MHD model generated by the Predictive Science Incorporated (PSI, San Diego, California).

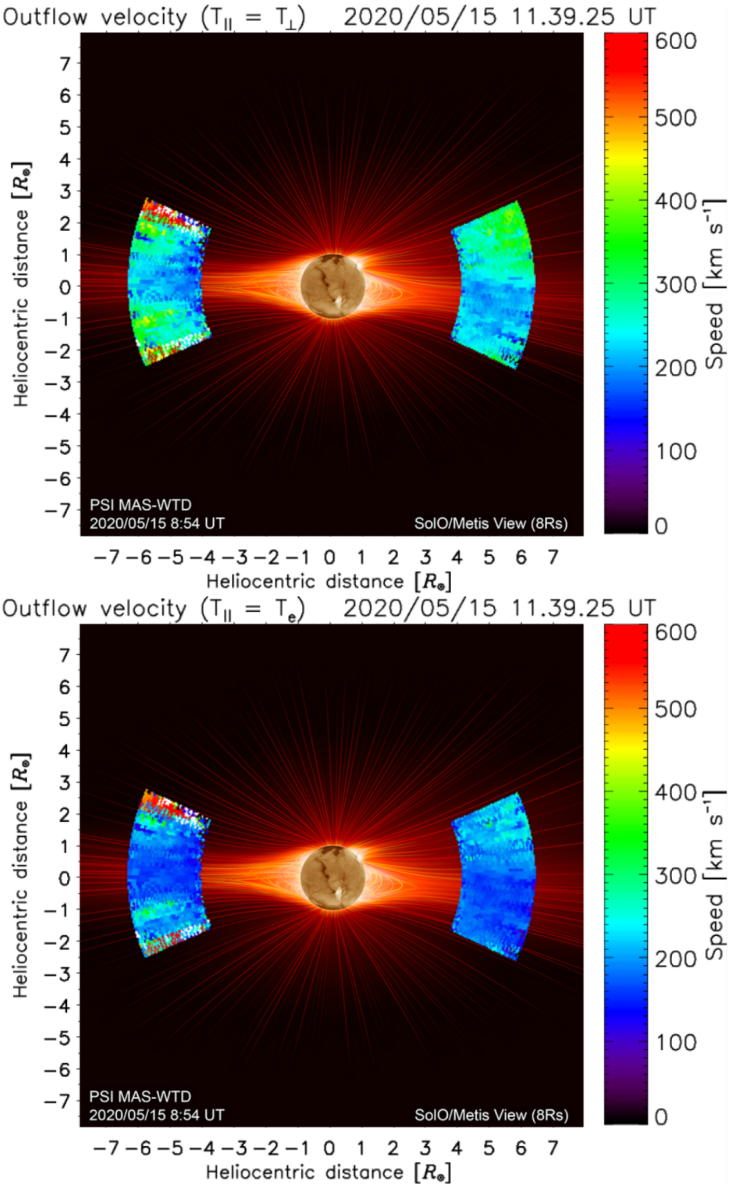

Figure 5.4: Outflow velocity maps of the neutral coronal hydrogen in the regions with S/N = 5, in the isotropic (top) and anisotropic (bottom) temperature scenarios. Image adapted from Romoli et al. (2021).

Since the West limb shows a more complex structure with respect to the East streamer, probably due to the occurrence of transient events or to a more warped streamer belt, the East limb corona is appropriate

for studying the super-radial expansion of the magnetic field lines as a modulator of the solar wind speed at and in the vicinity of the outward extension of the streamer belt, and also for relating the slow wind belt to the development of a web of separatrix or quasi-separatrix layers. For statistical reasons, the study was carried out in an angular sector with a width of about $\pm$ 30° across the solar equator, where the UV S/N > 3.

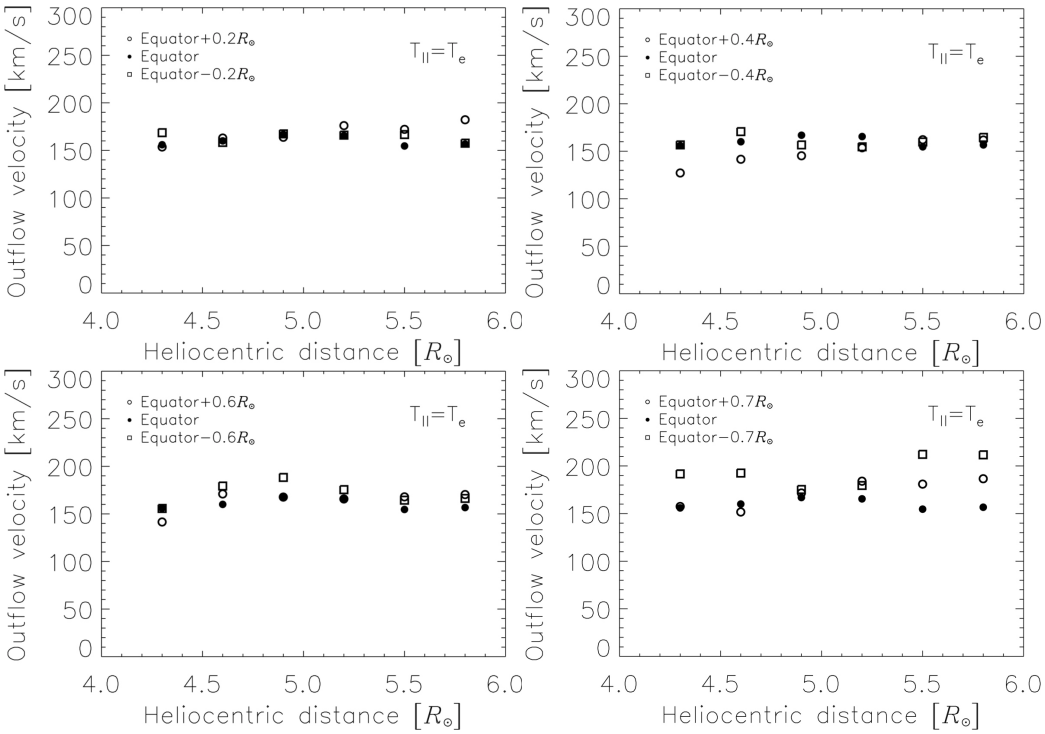

Figure 5.5: Outflow velocity in the anisotropic H I temperature case, as a function of the heliocentric distance and taking into account the edges of four strips with a width of $\pm$0.2 $R_\odot$ (top left), $\pm$0.4 $R_\odot$ (top right), $\pm$0.6 $R_\odot$ (bottom left), and $\pm$0.7 $R_\odot$ (bottom right) with respect to the equatorial plane. The cylindrical symmetry for the solar corona has been assumed. Panels adapted from Romoli et al. (2021).

This further investigation was performed considering the same data used in the previous work (Romoli et al., 2021). All the procedures of data handling are unchanged, except for the UV radiometric calibration. In fact, this one was improved by the author of the present manuscript by considering a set of standard UV stars transiting in the FoV of Metis. In

particular, the selected stars are α Leonis, ρ Leonis, observed on June 15 and 17, 2020, and ω Scorpii and θ Ophiuchi, observed on March 15 and 25, 2021, respectively. The transit of these stars occurred in the region corresponding to $\pm 30^{\circ}$ of latitude around the equator, such that the measurements of their UV fluxes were adopted to well calibrate the region of interest for this analysis. The fluxes measured along the different stellar trajectories were interpolated in the radial direction and averaged over specific latitudinal ranges, in order to derive a 2D radiometric calibration map applicable to the studied sector across the equator. Such a calibration returns Lyα intensities higher than those obtained in Romoli et al. (2021), especially in the inner region up to about 5 $R_{\odot}$, with uncertainties $\leq$20%.

The Doppler dimming technique was applied to the Lyα intensity data calibrated as aforementioned, along with the electron density coming from the MHD model developed by the PSI, which uses a wave-turbulent-driven (WTD) approach for the coronal heating (see Mikić et al., 2018; Boe et al., 2021, 2022). In order to account for the Metis pB observations, the author of this thesis normalised the modelled 3D electron density distribution in the following way. The values of the modelled electron density along each selected LOS were normalised multiplying them by a factor obtained from the ratio between the pB measured with Metis and that obtained by integrating the modelled polarised emissivity along the LOS. Such a factor ranges between 0.9 and 1.5 in the region selected for the analysis, with a trend almost constant along the radial direction. It is worth to note that the integration of the modelled polarised emissivity along the LOS was not performed within a constant spatial range along each LOS direction, but in a range that varies as a function of the radial distance. In fact, the data cube returned by the model has a longitudinal extension of $\pm 60^{\circ}$ around the POS. Then, given a point on the POS at a heliocentric distance r, the range of integration along the LOS is given by:

$$LOS(r) = 2r \tan 60^{\circ} = 2r\sqrt{3} \tag{5.1}$$

For example, in the analysed region, that goes from 4.0 $R_{\odot}$ to 6.8 $R_{\odot}$, the LOS integration range is equal to 13.9 $R_{\odot}$ and 23.6 $R_{\odot}$, respectively.

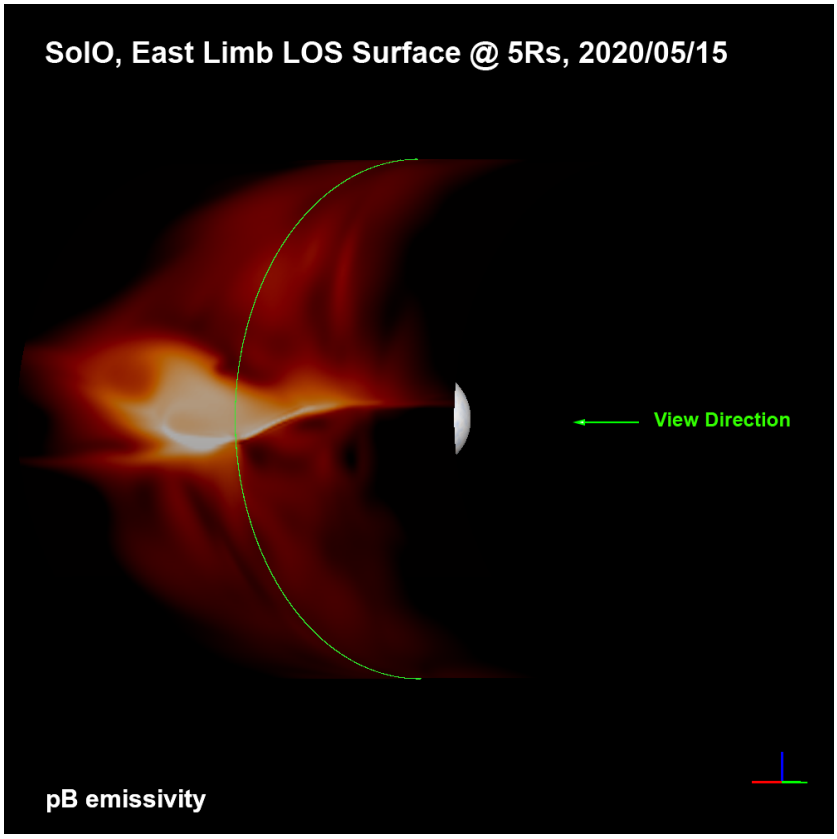

Figure 5.6: pB coronal emissivity along the LOS, at the East limb and at a distance of 5.0 $R_\odot$ on the POS (traced by the green line), as a function of the polar angle. The viewpoint is rotated of 45° in longitude from the Solar Orbiter position. The computation comes from a 3D MHD model of the PSI. The lightly warped sheet surrounding the HCS is highlighted. Image adapted from Antonucci et al. (2023).

Once performed the normalisation, the values of the electron density on the equatorial sheet, averaged along the LOS, range between 1.35×10^5 cm^{-3} and 0.30×10^5 cm^{-3} at 4.0 $R_\odot$ and 6.8 $R_\odot$, respectively (see Fig. 5.7, bottom panel). These values are slightly lower than those inferred when the cylindrical symmetry is assumed for the coronal configuration; however, in both cases the electron density latitudinal profiles show a flatter trend going toward the poles. In the northern side the density gradient is less steep, and the presence of an active region around 30° can be highlighted by the observed asymmetry. Behind $\pm 30°$, the density approaches coronal hole typical values (see Spadaro et al., 2017).

The electron and neutral hydrogen temperatures, and the chromospheric exciting intensity and profile used for this analysis are the same considered in Romoli et al. (2021). The helium abundance was assumed to linearly vary between 2.5% at the equatorial latitude to 10% at the boundaries of the considered latitudinal sector, following the results of Moses et al. (2020), concerning the study of a particular minimum configuration reached on 2009.

The synthetic H I Lyα intensity, thus, was derived by integrating the inferred Lyα emissivity along the same LOS ranges considered for the integration of the polarised emissivity. Therefore, the Doppler dimming technique was applied considering the tool reported in Appendix B, comparing the synthesised UV intensity with the observed one to estimate the outflow velocity of the coronal neutral hydrogen. In particular, the observed UV intensity was corrected for the interplanetary H I Lyα intensity, equal to 3.0 $\times$ 10^7 photons cm^{-2} s^{-1} sr^{-1} (for example, see Kohl et al., 1997).

The obtained results suggest that thin layers showing large velocity gradients delimit the core plasma sheet and separate the slowest wind from two faster and less dense streams at about 15° N and 10° S (see Fig. 5.8). In the plasma sheet the solar wind velocity ranges from about 117 km s^{-1} to about 150 km s^{-1} and from about 115 km s^{-1} to about 190 km s^{-1} as it propagates from 4.0 R$_\odot$ to 6.8 R$_\odot$, in the case of anisotropy ($T_{HI,\perp}$ = 1.6 $\times$ 10^6 K, $T_{HI,\parallel}$ = T_e) and isotropy ($T_{HI,\perp}$ = $T_{HI,\parallel}$ = 1.6 $\times$ 10^6 K) for the H I temperature, respectively. The velocity curves are characterised by an increase from the minimum value in correspondence of the current sheet to a peak value near 15° N and 10° S, that at 6.8 R$_\odot$ is of about 175 km s^{-1} and about 230 km s^{-1}, in the anisotropic and isotropic cases, respectively. In the slow stream the coronal plasma is accelerating at higher rate (Δv $\approx$ 30-75 km s^{-1} in 2.8 R$_\odot$) than in the faster wind layers surrounding the plasma sheet (Δv $\approx$ 15-40 km s^{-1} and Δv $\approx$ 20-60 km s^{-1} in 2.8 R$_\odot$, in the northern and southern higher velocity streams, respectively), where the first and second value of Δv indicate the anisotropic and isotropic cases, respectively.

The obtained wind speed results can be compared with the degree of expansion of the open magnetic field lines returned by the aforementioned 3D MHD model, which can be expressed in terms of the expansion

factor, that is a parameter measuring the divergence of the magnetic field lines and is defined as follows (for example, see Riley et al., 2015):

$$f_{B_r} = \left(\frac{r_0}{r_1}\right)^2 \frac{B_r(r_0, \theta_0, \phi_0)}{B_r(r_1, \theta_1, \phi_1)} \tag{5.2}$$

where B_r is the radial magnetic field component and (r_0, θ_0, ϕ_0) is the location from which the flux tube expands to another location indicated with (r_1, θ_1, ϕ_1). The expansion factor (f_{B_r}) characterising the field lines is reported in Fig. 5.9 (top panel) as a function of the polar angle and at 5.0 $R_\odot$ in heliocentric distance, lying on the POS (continuous line) and weighted for the pB emissivity along the LOS (dashed line). The zone of large expansion factor is delimited by two f_{B_R} minima located approximately at 10° S and 15° N, almost coincident with the latitudes corresponding to the two fastest wind streams.

The large width of the f_{B_R} peaks in coincidence of the slower wind characterising the denser plasma sheet. Thus, the expansion factor shows an anticorrelation with the outflow velocity as a function of the latitude, also if the feature at 86° is coincident with the peak of the density plasma sheet, while the outflow velocity minimum is located at about 92°. Going toward the wings of the profiles, the expansion factor shows a moderate increase, related to a moderate decrease of the outflow velocity. The effects of the expansion factor increase in the northern and southern sides are correlated to the presence of a 30° N active region and a 25° S flux concentration, both at the 340° Carrington longitude (for what concerns the latter, the zero meridian used today in the Carrington system was defined on January 1, 1854, in correspondence of the meridian that passed the ascending node, given by the intersection between the solar equator and the ecliptic plane, at Greenwich noon).

It is worth to note that the outflow velocity resulting from the approach used in Romoli et al. (2021), but applying the improved UV calibration, has been also determined by the author of the present manuscript, and the comparison with the expansion factor has been performed. In Romoli et al. (2021) the warping of the plasma sheet is neglected, and the cylindrical symmetry in the computation of the electron density derived from the Metis polarised brightness observations is taken into account. In this case, the velocity shows a more pronounced dip in a narrow zone

coincident with the axis of the plasma sheet at 86° and a second minor dip at about 95°.

Finally, the hypothesis of the contribution of a S-Web in the onset and acceleration of the solar wind can also be taken into account. Fig. 5.10 shows the squashing factor Q along the LOS, returned by the 3D MHD model, at the East limb and at 5 $R_\odot$ on the POS, as a function of the polar angle. This parameter is a measure of the gradient in the field line mapping (Titov et al., 2011) and highlights the separatrix and quasi-separatrix coronal layers, which extend up to 30° from the HCS (Titov et al., 2002). In Fig. 5.9 (bottom panel) the main features of the squashing factor are shown within ±30° around the equator, with the most prominent peaks appearing at about 10° N and 5° S (PA = 80° and PA = 95°, respectively). These are the latitudes where the wind speed positive gradients delimit the slow stream centered on the plasma sheet. Then, high values of the squashing factor can be linked to the increase of the outward flowing wind velocity, which also coincide with the lowest expansion factors of the magnetic field lines.

The ratio $f_{max,B_r}/f_{B_r}$ between the maximum expansion factor experienced by the magnetic field lines along the radial direction (f_{max,B_r}) and the expansion factor at 5 $R_\odot$, weighted for the pB emissivity along the LOS, is shown in Fig. 5.11 as a function of the polar angle. This quantity shows two peaks at about ±20° with respect the equatorial plane, identifying the regions where the divergence-convergence behavior of the field lines is more significant. These regions are located roughly at the boundaries of the separatrix web region, which indicates that the S-web is limited by regions where the wind flux tubes divergence shows the largest non-monotonic behavior.

Therefore, in the slow wind zone, where the wind speed is regulated by the magnetic field lines expansion, a significant contribution can be also given by the plasma ejected during reconnection processes occurring within the open field corridors characterising the separatrix and quasi-separatrix web.

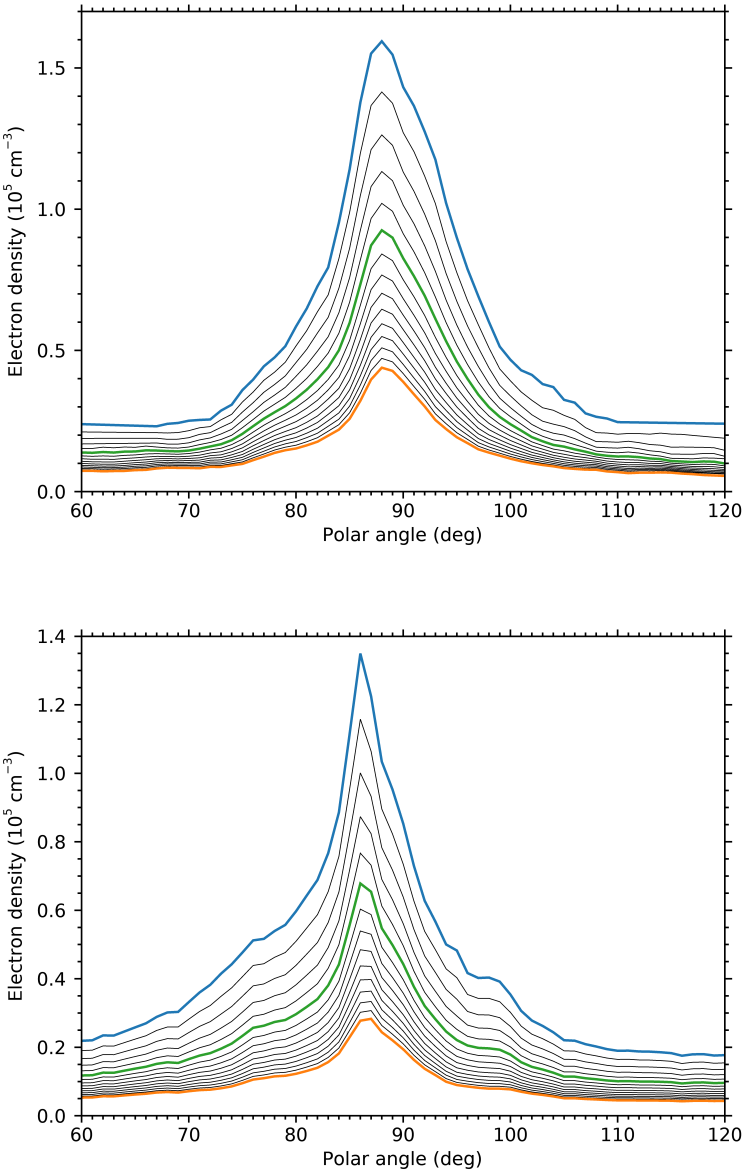

Figure 5.7: Coronal density as a function of the polar angle obtained under the hypothesis of cylindrical corona and applying the Van De Hulst (1950) method to the pB data acquired with Metis on May 15, 2020 (first light; top panel), and inferred from the PSI 3D MHD model after the normalisation performed by considering the pB observed with Metis (bottom panel). The curves are shown at step of 0.2 $R_\odot$, going from 4.0 $R_\odot$ to 6.8 $R_\odot$. The blue, green, and red lines indicates the profiles inferred at 4.0 $R_\odot$, 5.0 $R_\odot$ and 6.8 $R_\odot$, respectively. Panels adapted from Antonucci et al. (2023).

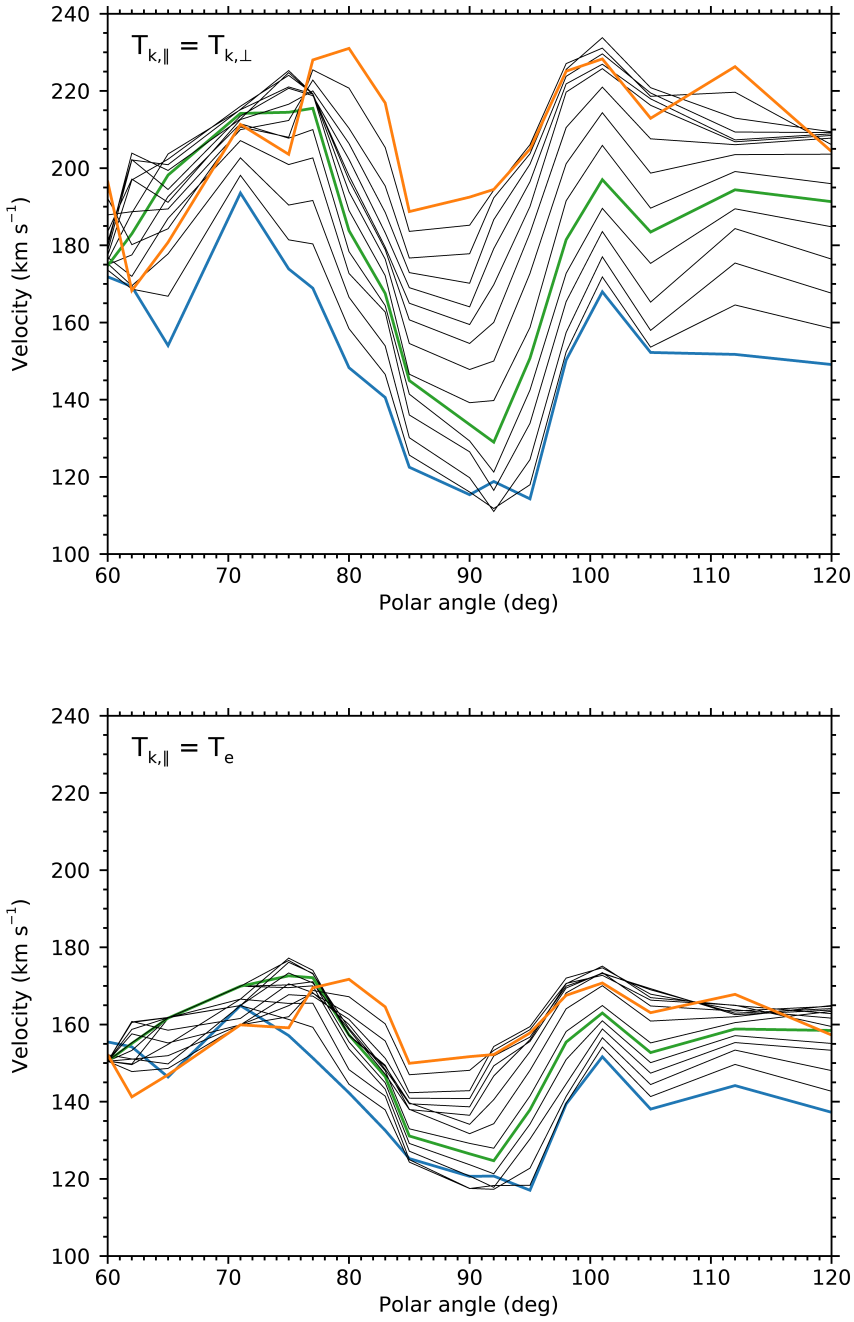

Figure 5.8: Outflow velocity as a function of the polar angle in the isotropic (top panel) and anisotropic (bottom panel) cases, when the Metis first light and the 3D MHD model of the PSI are considered. The curves are shown at step of 0.2 $R_\odot$, going from 4.0 $R_\odot$ to 6.8 $R_\odot$. The blue, green, and red lines indicates the profiles inferred at 4.0 $R_\odot$, 5.0 $R_\odot$ and 6.8 $R_\odot$, respectively. Panels adapted from Antonucci et al. (2023).

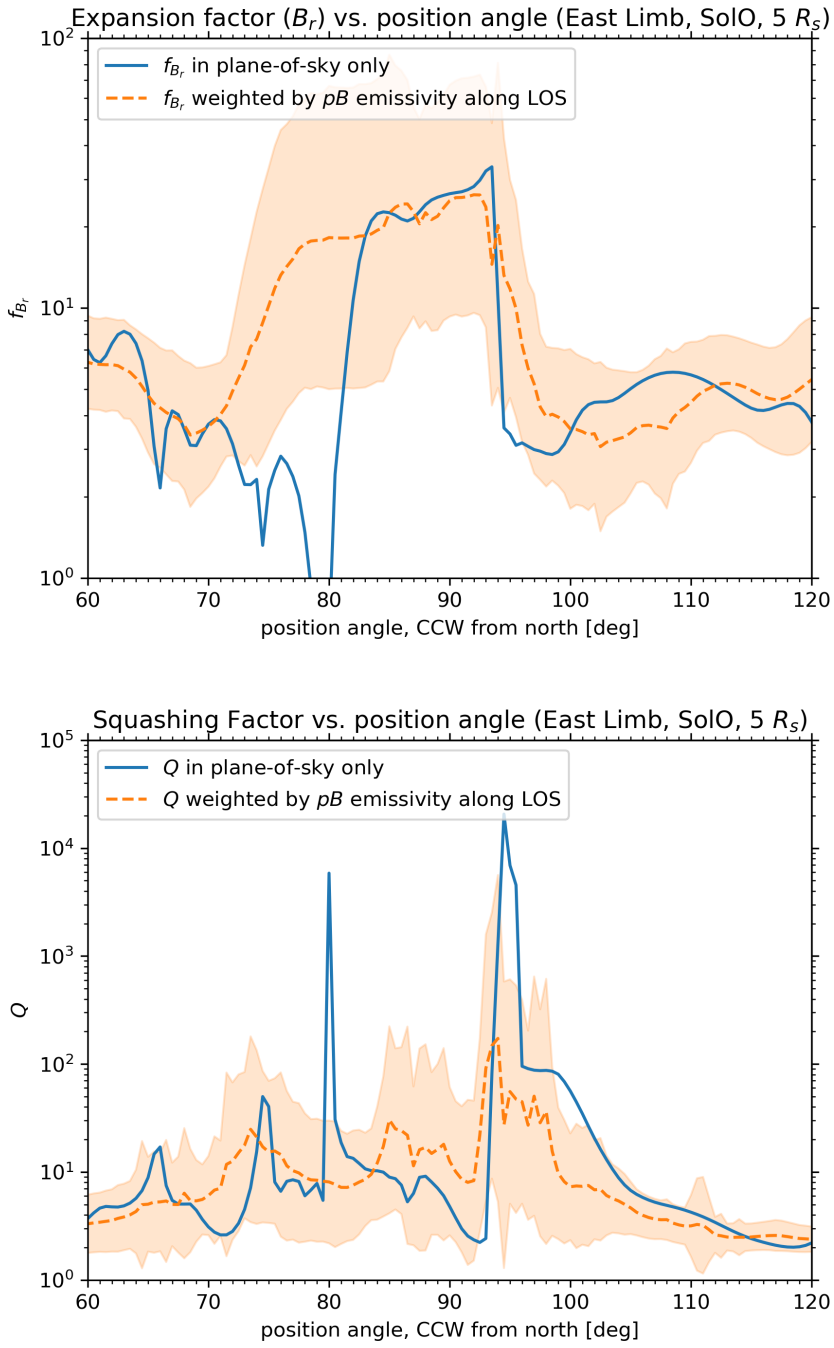

Figure 5.9: The expansion factor experienced by the magnetic field lines (top panel) and squashing factor (bottom panel) as a function of polar (position) angle, setting the heliocentric distance at 5.0 $R_\odot$. The continuous line indicates the quantity lying on the POS, while the dashed line is weighted for the pB emissivity along the LOS. The shaded area represents the ± 1 standard deviation. Bottom panel adapted from Antonucci et al. (2023).

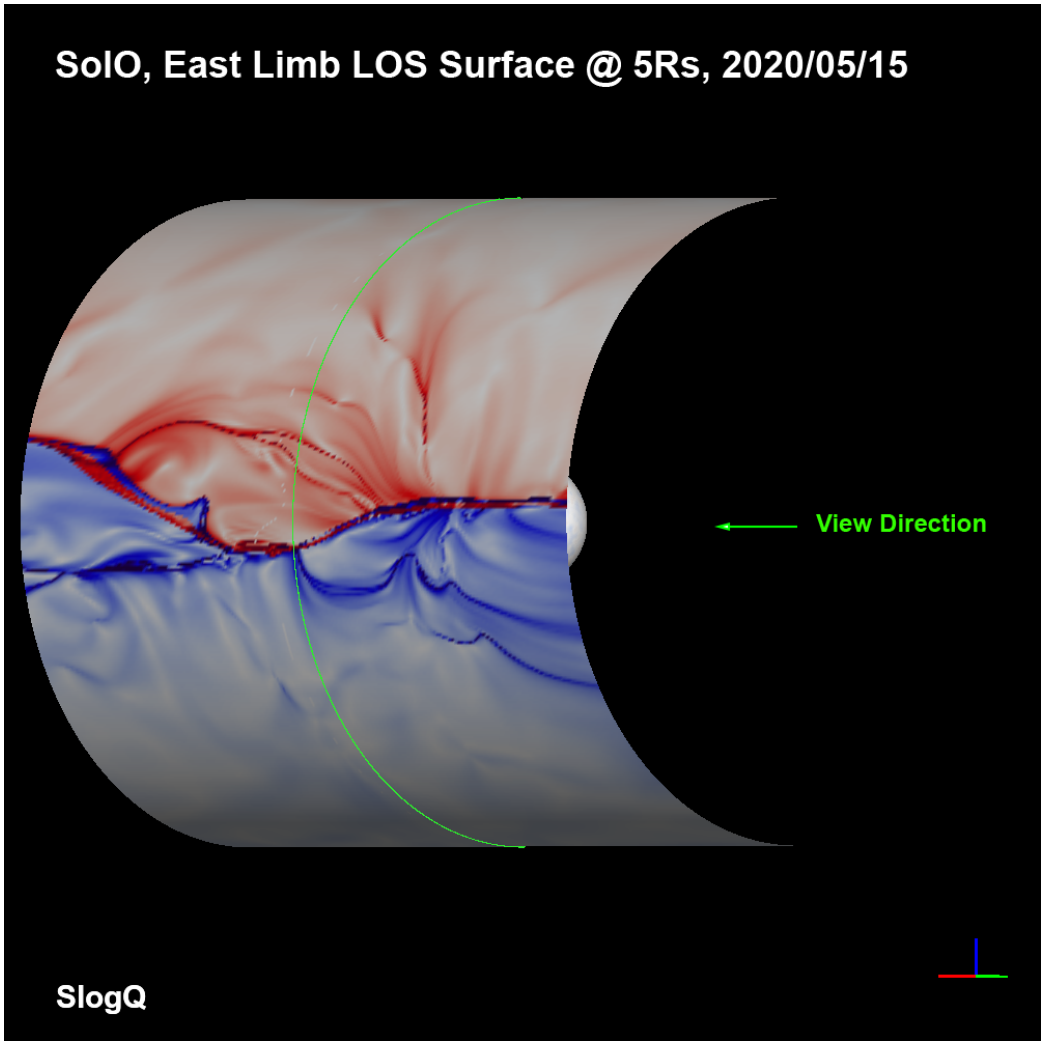

Figure 5.10: As in Fig. 5.6, but for the squashing factor. Figure adapted from Antonucci et al. (2023).

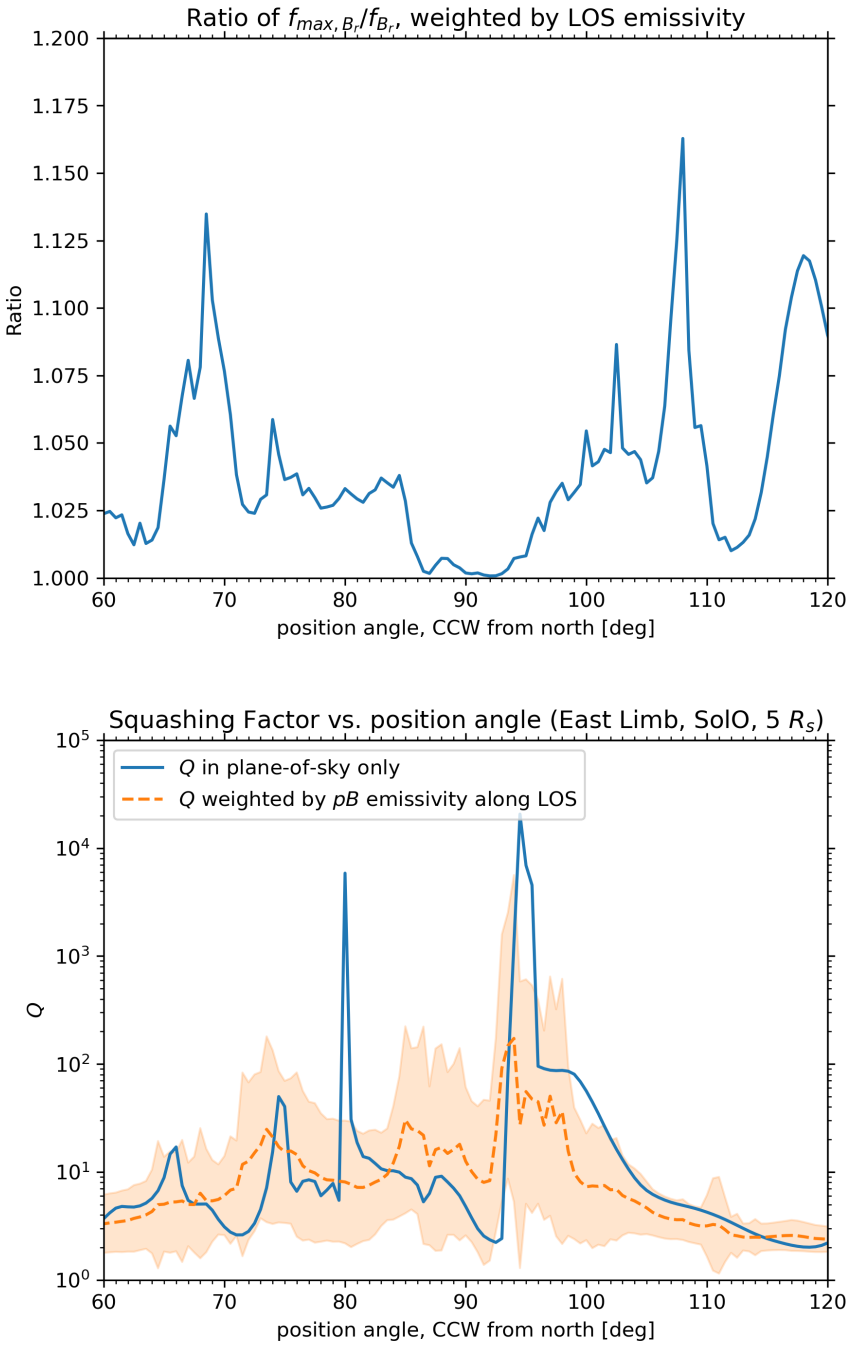

Figure 5.11: Ratio $f_{max,B_r}/f_{B_r}$ between the maximum expansion factor experienced by the magnetic field lines along the radial direction and the expansion factor at 5 $R_\odot$, weighted for the pB emissivity along the LOS (top panel). This quantity is compared with the squashing factor as a function of polar (position) angle, setting the heliocentric distance at 5.0 $R_\odot$ (bottom panel). In the latter case, the continuous line indicates the quantity lying on the POS, while the dashed line and the shaded area in the bottom panel represent the quantity weighted for the pB emissivity along the LOS and the ± 1 standard deviation, respectively. Panels adapted from Antonucci et al. (2023).

5.2 First SolO - PSP quadrature

The first quadrature between SolO and PSP gave the opportunity to investigate the evolution of the solar wind from the extended corona to the inner heliosphere, by coupling PSP in-situ measurements and Metis remote sensing observations (see Telloni et al., 2021). In this view, the author of this thesis work analysed the Metis and PSP data in order to determinate coronal quantities up to relatively high heliocentric distances, such as neutral hydrogen outflow velocity, electron density, and radial magnetic field.

Such a quadrature occurred on January 18, 2021, when PSP was at 0.1 au ($\approx$ 22 $R_\odot$) from the Sun and SolO was orbiting at 0.58 au, resulting in a FoV extending from 3.5 $R_\odot$ to 6.3 $R_\odot$. The joint SolO-PSP observations allowed to analyse the behaviour of the solar wind not yet processed by non-linear interactions, such that it has been possible to relate the local properties of the plasma with the coronal sources. While Metis was observing the outflowing plasma, the PSP spacecraft was about 30° behind the POS, such that it probed the same plasma observed by Metis. In fact, PSP and the plasma observed by Metis reached the same location at the same time, about 16 hours later the Metis remote measurements, based on the velocity inferred by Metis observations (see Fig. 5.12). In particular, Metis observed the corona on January 17, 2021, at 16:30 UT, while PSP reached the POS on January 18, 2021, at 08:44 UT, when it was 3.8° below the ecliptic plane.

The analysis of Metis data was performed in the following way. Since PSP probed the plasma in an angular sector of $\pm$2.5° around the 3.8° S latitude when the spacecraft reached the POS, a mean around this sector was performed for pB and UV images, obtaining a radial profile for each observed quantity (see Figs. 5.13 and 5.14). These profiles were used to infer the electron density n_e and the outflow velocity radial profiles for the coronal plasma that impinged on the PSP instruments. The inversion method proposed by Van De Hulst (1950) was applied to the pB radial profile by using the tool reported in Appendix A, obtaining the electron density profile shown in Fig. 5.15. The inferred density values fit very well the value obtained by the proton density n_p measurement performed with PSP, assuming a helium abundance of 2.5% of the fully

ionised plasma, which means $n_e = n_p/0.95$ (Moses et al., 2020). The measured electron density ranges between 4×10^5 cm^{-3} and 4×10^4 cm^{-3} between 3.5 R$_\odot$ and 6.3 R$_\odot$, respectively. The value deduced by PSP measurements is about 2.4×10^3 cm^{-3} at 21.4 R$_\odot$. The inferred densities agree with those found by Romoli et al. (2021) and Antonucci et al. (2023) within the denser plasma sheet region.

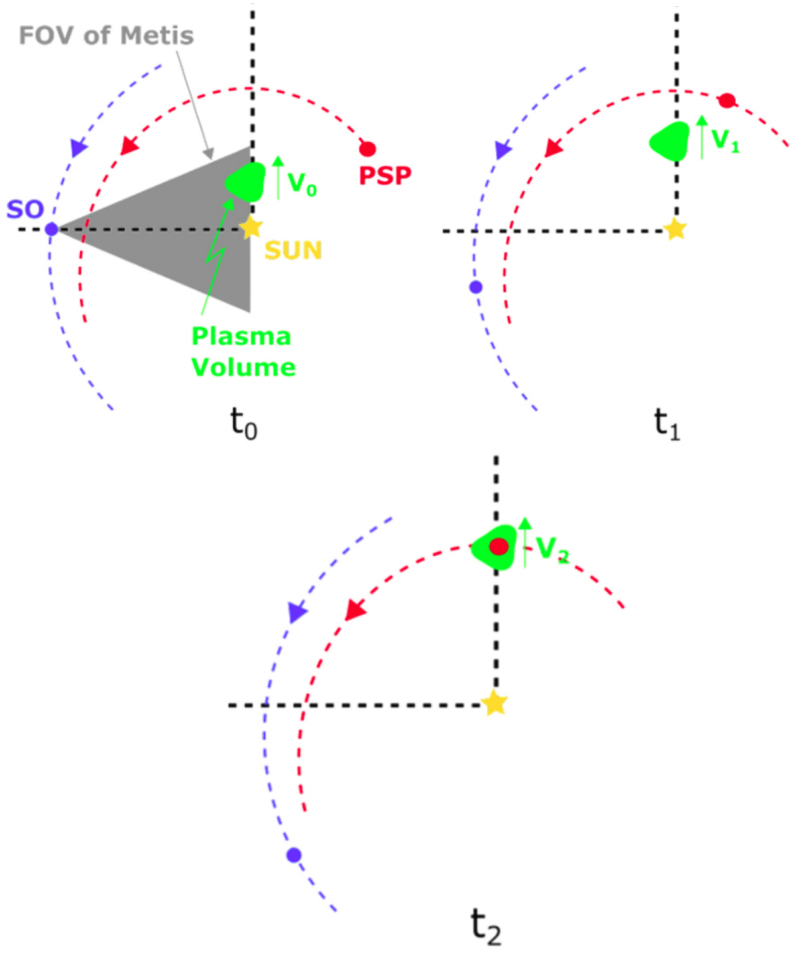

Figure 5.12: Positions of SolO (blue) and PSP (red) relative to the Sun (yellow). t_0 is the time of Metis observations, t_2 is the time in which the observed plasma and PSP reached the POS, and t_1 is an intermediate time. Panels adapted from Telloni et al. (2021).

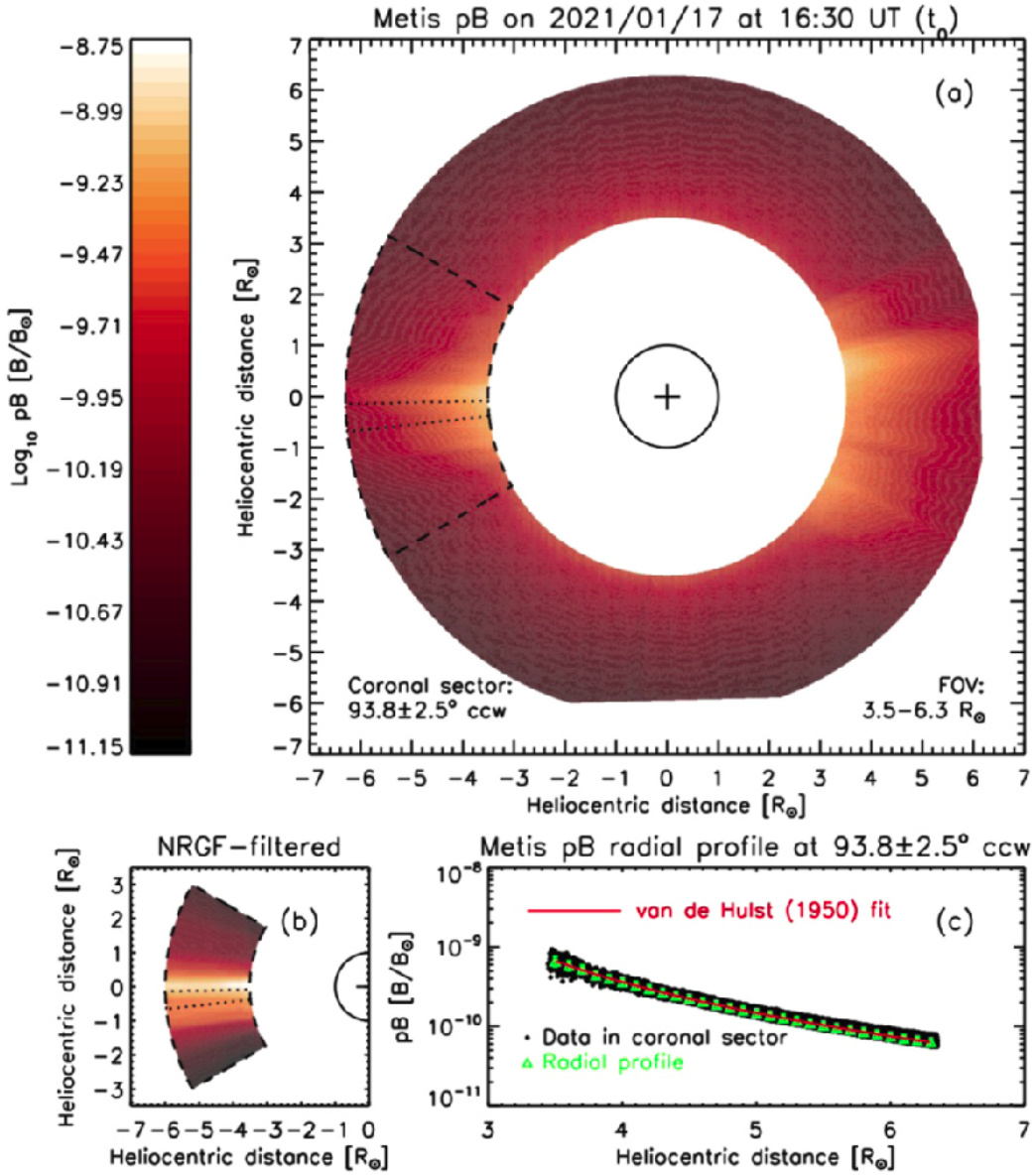

Figure 5.13: pB observed with Metis on January 17, 2021, at 16:30 UT. The sectors delimited with dashed lines ($\pm 30^\circ$ around the equatorial plane) are highlighted in the bottom left by using a normalizing-radial-graded filter (NRGF). In the bottom right the radial profile obtained by averaging the data in the sector between the dotted lines, with a width of $\pm 2.5^\circ$ and centered at 3.8° S, is obtained. Image adapted from Telloni et al. (2021).

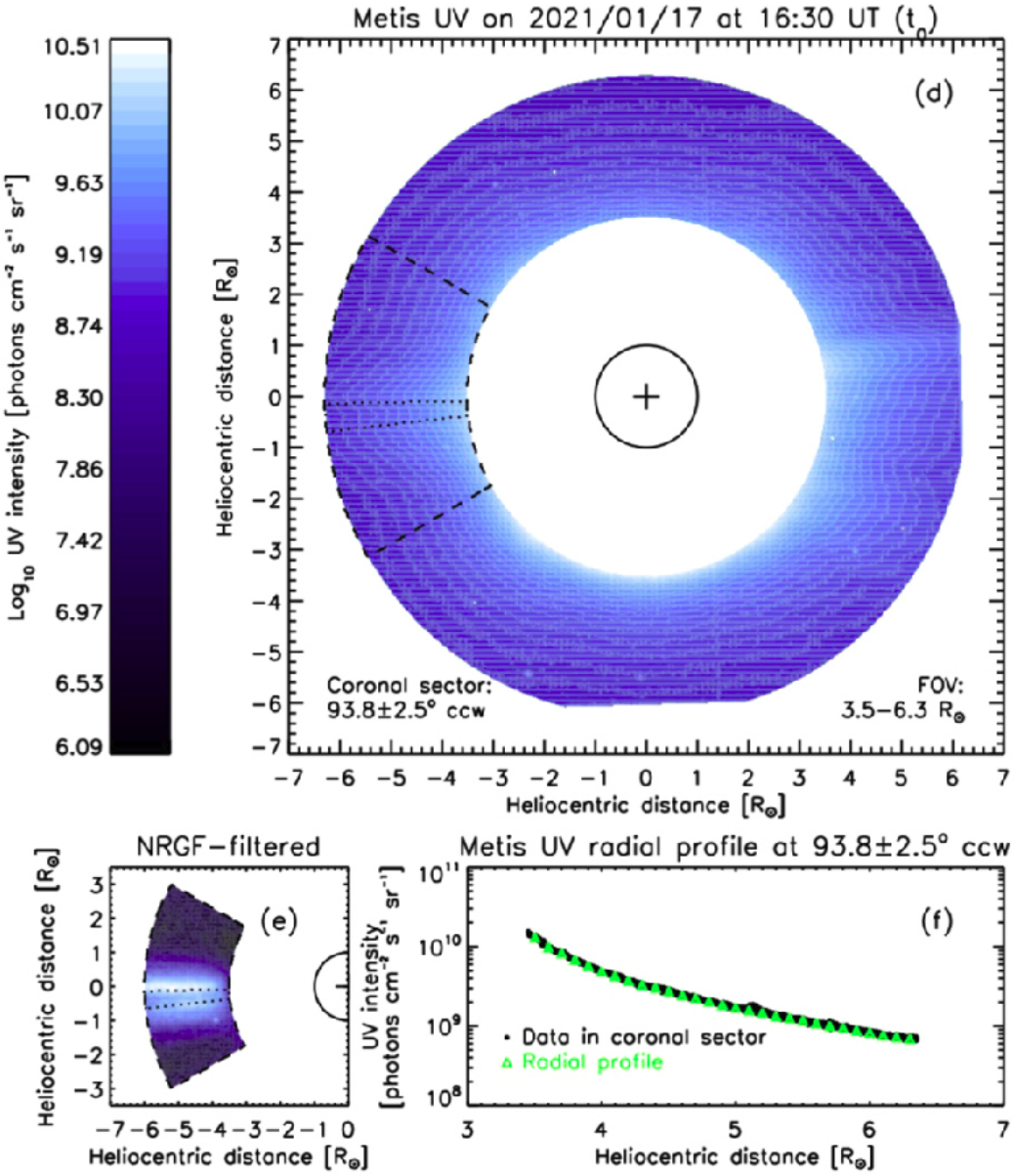

Figure 5.14: As in Fig. 5.13, but for the H I Lyα observed on January 17, 2021, at 16:30 UT. Image adapted from Telloni et al. (2021).

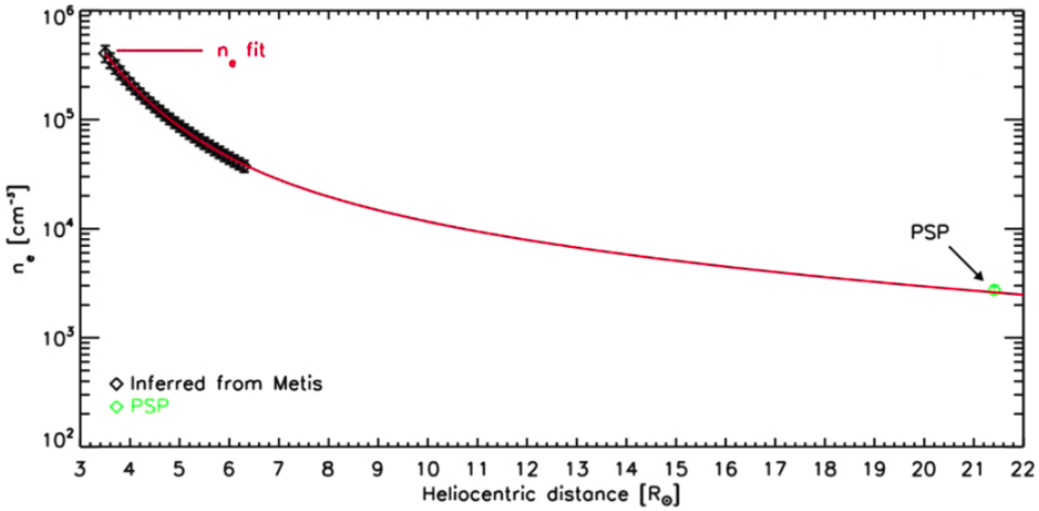

Figure 5.15: Electron density inferred from pB observations performed with Metis on January 17, 2021, at 16:30 UT, in a sector of $\pm 2.5°$ centered at 3.8° S, by applying the Van De Hulst (1950) method. See Telloni et al. (2021).

The outflow velocity was obtained by applying the tool reported in Appendix B to the pB and H I Lyα data obtained simultaneously with Metis, where the tool exploits the Doppler dimming technique. The synthetic Lyα intensity, to be compared with the observed one to obtain iteratively the outflow velocity, was calculated by considering the following assumptions. The electron temperature was derived following the expression proposed by Gibson et al. (1999); the perpendicular neutral hydrogen temperature was set equal to 1.6×10^6 K (such as in Romoli et al., 2021; Antonucci et al., 2023), and the anisotropy degree $T_{HI,\perp}/T_{HI,\parallel}$=1.72 was assumed; the chromospheric exciting Lyα intensity was set equal to 5.42 $\times 10^{15}$ photons cm^{-2} s^{-1} sr^{-1}, provided by the LASP Interactive Solar Irradiance Data Center, while the relative exciting profile is that proposed by Auchère (2005). It is worth to note that the considered anisotropy degree was measured with PSP for the protons, and was adopted as a proxy for the neutral hydrogen anisotropy degree by assuming an efficient mechanism of charge exchange. The inferred velocity (see Fig. 5.16) shows a rapid increase as a function of the heliocentric distance, from $\approx$ 80 km s^{-1} to $\approx$ 150 s^{-1} in the range going from 3.5 $R_\odot$ to 4.5 $R_\odot$, and then the plasma experiences a lower acceleration, achieving a velocity of about

180 km s^{-1} at 6.3 $R_\odot$. The velocity measured in-situ at the PSP location is 247 km s^{-1}. It is possible to find a good fit (red line) between the velocity values obtained with Metis and PSP measurements, where the used function is a sum of a log-normal distribution and logarithmic quadratic function, which has not interpretative aims, but only permits to define an analytical profile. Furthermore, these values are comparable with those inferred by the Metis first light analysis in the equatorial region.

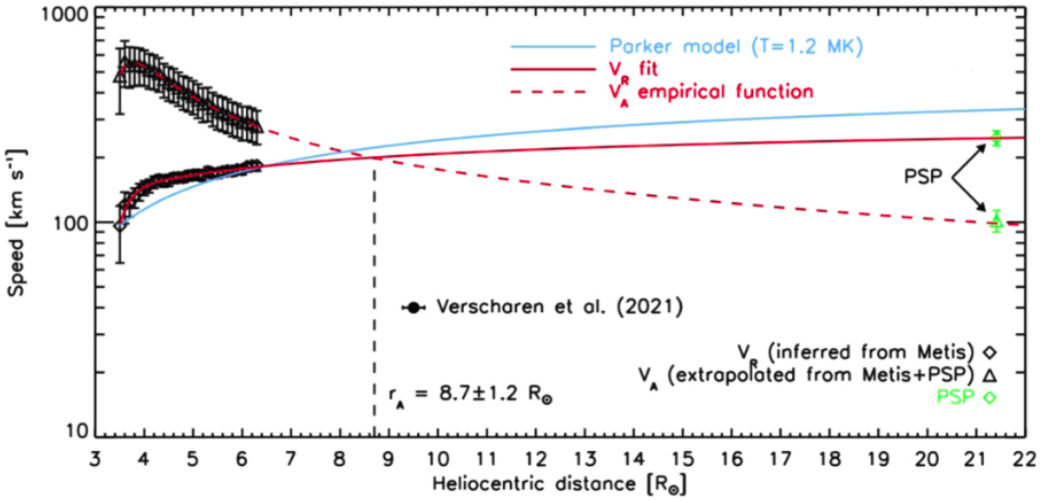

Figure 5.16: Outflow velocity inferred from Metis observations performed on January 17, 2021, at 16:30 UT, in a sector of $\pm 2.5°$ centered at 3.8° S. The Alfvén velocity and radius are also shown, and the curve obtained from the Parker model with a temperature of 1.2×10^6 K is also reported. See Telloni et al. (2021).

By applying the conservation of the mass and magnetic frozen-flux to Metis velocity and density measurements, and using plasma and magnetic field data obtained by PSP, the radial trend of the magnetic field was estimated (see Fig. 5.17), not directly measurable in the corona. The inferred radial magnetic field values range from about 10^4 nT to 2×10^3 nT in the range 3.5 - 6.3 $R_\odot$, while in the PSP position the in-situ measured radial magnetic field value is about 2.4×10^2 nT. These values are lower than those reported in the literature (Dulk & McLean, 1978; Pätzold et al., 1987; Vršnak et al., 2004; Gopalswamy & Yashiro, 2011; Poomvises et al., 2012; Mancuso & Garzelli, 2013), which are based on remote sensing observations, where the contribution from LOS integration effects is

not negligible, and in some cases in-situ measurements very far from the Sun are considered, not allowing a clear connection to the coronal source regions. Instead, in the present case the accuracy of the coronal magnetic field values is much higher due to the proximity of PSP to the Sun.

These results demonstrate that the capabilities of the Metis coronagraph, along with the synergy with the PSP activity, allow to investigate in detail coronal plasma quantities up to high heliocentric distances, as never done before.

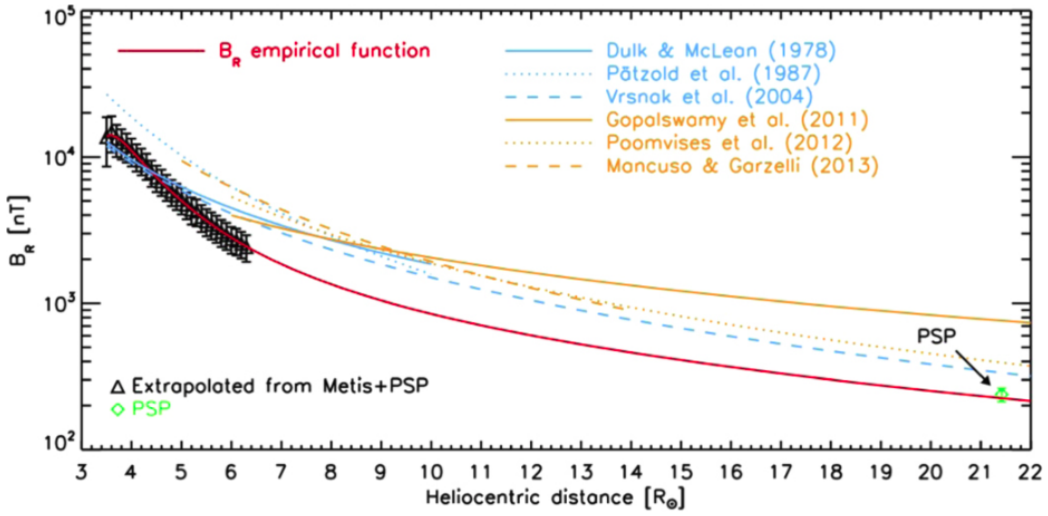

Figure 5.17: Radial magnetic field inferred by assuming mass and magnetic flux conservation. The profile was obtained starting from Metis observations performed on January 17, 2021, at 16:30 UT, in a sector of $\pm 2.5°$ centered at 3.8° S. Magnetic field radial profiles from literature (see text) are also shown for comparison. See Telloni et al. (2021).

5.3 First CME observed with Metis

The Metis performances also allow to obtain detailed information on transient events, identifying their fine structure and following their evolution from their early propagation, simultaneously in polarised brightness and in H I Lyα imaging. These features are very important for the development of forecasting tools for the occurrence of these events and their impact to the Earth magnetosphere, in view of space weather applications (for example, see Hapgood & Thomson, 2010). Regarding this subject, the

author of this thesis gave a significant contribution in the data handling and in the kinematics investigation of the first CME observed with the Metis coronagraph.

On January 14-17, 2021, the Metis coronagraph acquired VL and H I Lyα images at about 0.6 au from the Sun, during a synoptic programme to obtain out-of-ecliptic-remote-sensing-window observations along the spacecraft orbit, in order to monitor the status of the solar corona for a longer time. During this synoptic programme, one VL pB sequence and two UV images were acquired simultaneously every 4 hours, starting at 00:30 UT on January 14, 2021.

Metis observed for the first time a slow and relatively faint CME occurred on January 16-17, 2021, and other observations of the same event were performed with different space telescopes and from different positions around the Sun, such as the SOHO/LASCO-C2 and STEREO-A/COR2 coronagraphs. Such a CME appeared as an almost circular feature propagating above the East limb as observed with LASCO-C2 and COR2 coronagraphs, close to the ecliptic plane, while Metis observed the event above the West limb, because at that moment SolO was almost in opposition with respect STEREO-A, while the latter was separated by about 56° from SOHO (see Fig. 5.18).

The event was visible in the Metis FoV from 00:30 UT to at least 12:30 UT of January 17, 2021. Fig. 5.19 shows the CME images obtained with Metis in the pB (top row) and H I Lyα channels (bottom panel) from 00:45 UT to 12:53 UT. It is possible to note that these images show the same features in both channels. In particular, due to their high resolution, the pB images are more detailed than the UV images, although some features observed in the UV channel seem to be more structured than the pB counterpart. For example, the separation between the leading fronts in the UV images acquired at 04:53 UT are more evident than in pB images.

To identify the location of the source region of the CME, a graduated cylindrical shell (GCS) 3D model was applied to reconstruct the transient event (Thernisien et al., 2006; Thernisien, 2011), where the author of this thesis gave a significant contribution for its correct application; to reach this aim, the Metis images were coupled with those acquired with STEREO-A/COR 2 and SOHO/LASCO-C2 (see Fig. 5.20). Data obtained at 19.5 nm and 30.5 nm from the Extreme Ultraviolet Imager (EUVI), on

board STEREO-A, and in 17.4 nm by the Full Sun Imager (FSI) of the EUI instrument, aboard Solar Orbiter, were also considered for this purpose. The results suggest that the source region was located at 13.4° S and at a Carrington longitude of 292.5°. The source region position is consistent with the location of the AR NOAA 12797, although they do not overlap, but form an angle of about 30° toward East with respect to the active region. Such a discrepancy can be justified by deviations and rotations of the CME with respect to the position of the source region. Closer inspections of EUVI 30.4 nm images revealed that the source region was located almost exactly in a filament channel East of the AR.

Finally, in order to estimate the velocity propagation of the CME, the multiple loop-like features visible in the UV images were tracked. In particular, an elliptical fit was performed on the location of the inner front for two different times between 04:30 UT and 05:00 UT, determining an expansion velocity of the front of about 140 km s^{-1}, while the centre of the CME flux rope, identified by the center of the ellipse, was estimated to propagate at 70 km s^{-1} (see Fig. 5.21). These values are similar or slower than those which characterise the plasma where the CME propagates, such as reported in Telloni et al. (2021); Romoli et al. (2021); Antonucci et al. (2023).

It is interesting to note that the similarity between the pB and UV images apparently contradicts the results found by Bemporad et al. (2018), who predicted that the observed CME front should appear darker in Lyα with respect the background corona, because of the Doppler dimming of the coronal H I Lyα radiation. However, this scenario is valid for a simulated fast CME with radial velocities greater than 300 km s^{-1}. Since for the present analysis the expansion speed of the transient event is much lower, the contribution of the Doppler dimming on the coronal UV intensity is small. For example, Dolei et al. (2018) found that for the inferred velocities, the Doppler dimming reduction factor is of about 0.75, while for velocities higher than 300 km s^{-1} the reduction factor reaches values below 0.1. Furthermore, the presence of non-equilibrium ionisation effects (Pagano et al., 2020), that produce a higher fraction of neutral hydrogen atoms in the CME front with respect to the equilibrium case, could give a contribution to the H I Lyα intensity increase. Then, all these considerations can explain the similarities between the pB and UV images.

The author of this thesis contributed in the application and the checking of the described procedures and in the writing of the relative paper, such as done for the other works presented in this chapter.

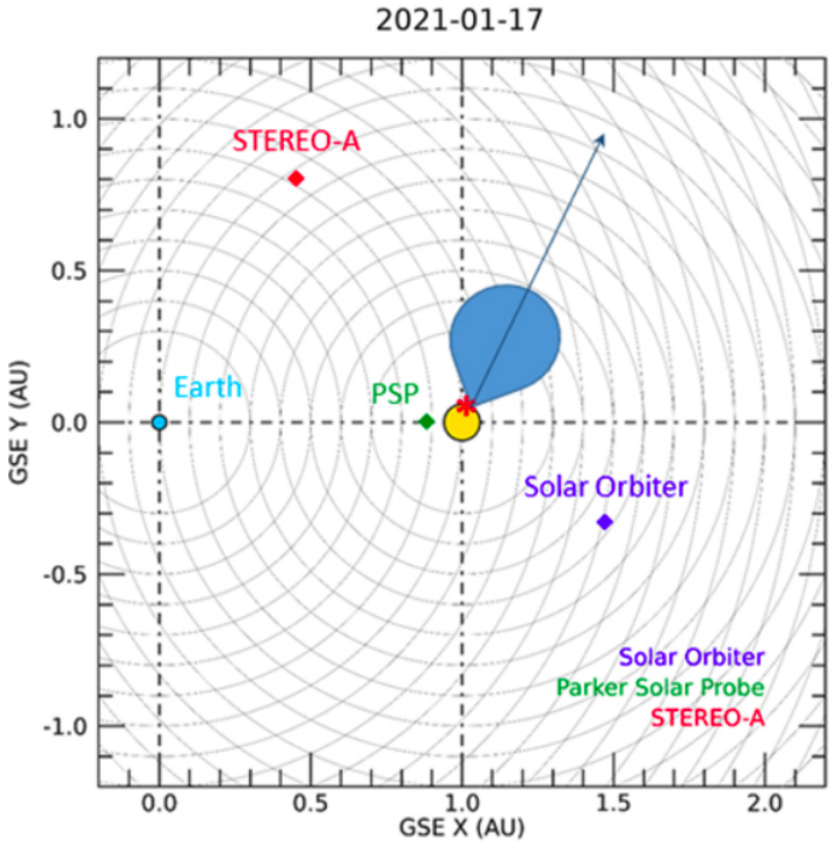

Figure 5.18: Positions of the SolO, PSP, STEREO-A, and SOHO (L1 point near the Earth) spacecraft with respect to the Sun. Image adapted from Andretta et al. (2021).

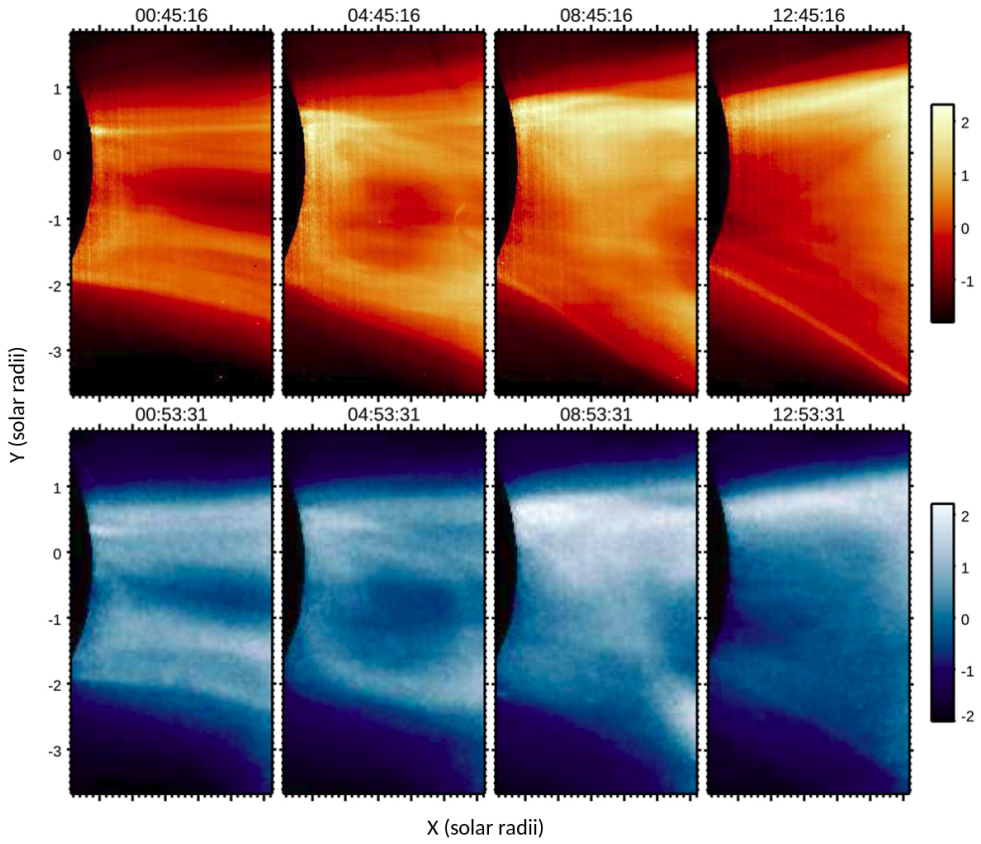

Figure 5.19: Images of the CME observed with Metis on January 16 and 17, 2021 (VL pB and UV Lyα), processed via the NRGF alghorithm and with the scale in unit-less numbers as produced by the algorithm. Each UV image shown in the panels is the second observed in the relative set. Image adapted from Andretta et al. (2021).

.

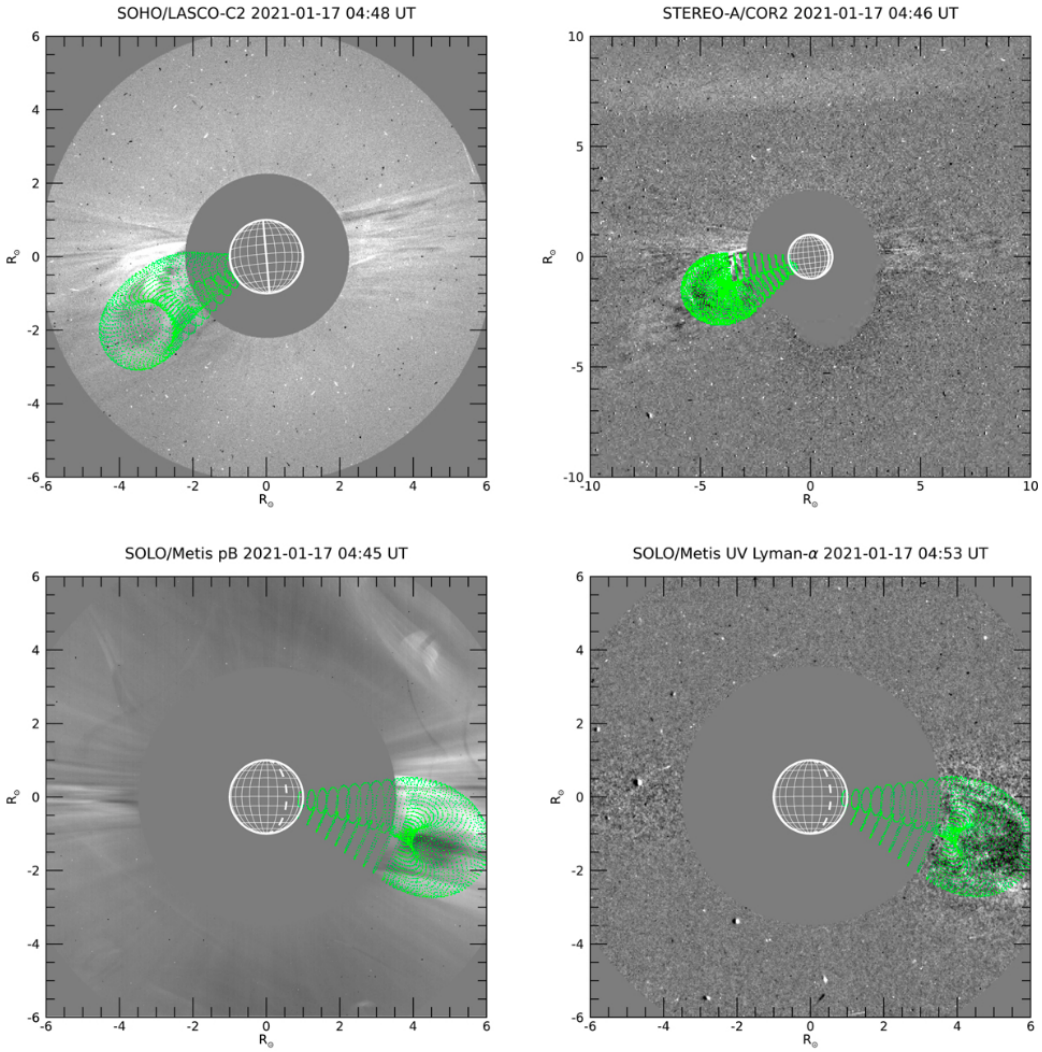

Figure 5.20: Top row: GCS reconstruction applied to running-difference images by the SOHO/LASCO-C2 (left) and STEREO-A/COR2 (right) instruments. Bottom row: same reconstruction applied to the SolO/Metis pB image (left) and the H I Lyα image (right). In the Metis images, transient and spurious reflections recorded in both channels can be observed, probably due to small debris passing in front of the telescope aperture. However, these reflections do not remarkably affect the sector of the FOV where the CME is observed. The Stonyhurst coordinate grid, with a spacing of 15°, is overlaid on the images, where the zero is set at the intersection of the equator plane and central meridian as seen from the Earth. The latter (solid white line) or the meridian opposite to Earth (dashed white line) are also shown. Image adapted from Andretta et al. (2021).

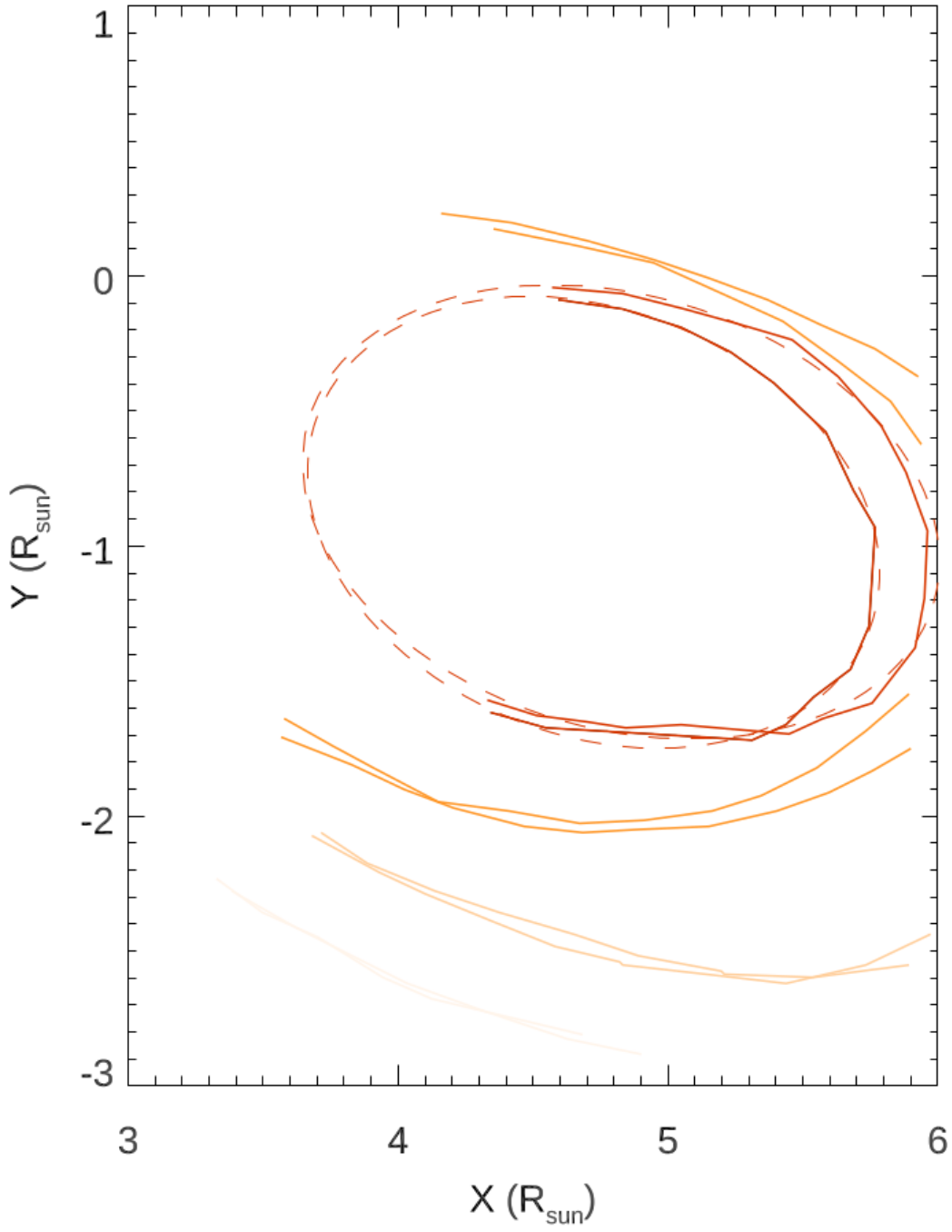

Figure 5.21: CME fronts observed on January 16-17, 2021, between 04:30 UT and 05:00 UT. The inner front was measured in two times (red solid lines) and fitted with an ellipse (dashed red lines), in order to measure the front and centre propagation speeds, the latter identified by the centre of the ellipse. The other lines identify the other fronts viewed in the images. Image adapted from Andretta et al. (2021).

Conclusions

The aim of this thesis work is to give a contribution to understanding how the magnetic field regulates the structure of the outer solar atmosphere, with important effects on the heating and the acceleration of the coronal plasma into the heliosphere and on the different regimes of the solar wind. The main atmospheric structures highlighting the solar activity are introduced, along with the main features of the solar wind, its source regions and currently accepted acceleration mechanisms. The main coronal diagnostics techniques are described, used to infer the expanding corona density and outflow velocity starting from remote sensing observations, such as those performed with Metis. In particular, the inversion method developed by Van De Hulst (1950) is described in detail. Such a method provides the coronal electron density distribution starting from VL pB data. The technique used to infer the solar wind outflow velocity exploits the Doppler dimming process for the H I UV Lyα radiation, according to which the coronal flowing hydrogen atoms are less efficient in resonantly scattering the chromospheric exciting UV radiation, due to the red-shift of the inner atmosphere photons as seen by the flowing atoms. The coronal H I Lyα intensity can be synthesised by considering physical parameters taken from specific coronal models and from literature, such as electron and H I temperatures, and chromospheric exciting radiance and profile, along with the electron density obtained from pB measurements, applying the aforementioned Van De Hulst (1950) technique. The comparison between the synthetic intensity and the observed one, on the POS, allows to determine the outflow velocity of hydrogen atoms by iteratively changing this parameter until a satisfactory match between the compared intensities is reached. This method requires simultaneous acquisitions of the coronal pB and UV radiation to be applied: Metis is the first corona-

graph designed to reach this purpose.

The main characteristics and performances of the instrument are described, along with the main data handling procedures.

A detailed analysis of the Metis first light has been carried out (May 15, 2020), with the aim of studying the propagation of the solar wind in the corona, in order to investigate the slow wind sources out to the boundary between the fast and slow wind. A first analysis, performed in an angular sector of $\pm 20^{\circ}$ wide, returned, in the region corresponding to the denser plasma, velocity values of about 200 km s^{-1} and 160 km s^{-1} in the cases in which isotropic and anisotropic H I temperartures are considered, respectively, with an almost-constant trend along the radial direction. The inferred electron densities show higher values in about $\pm 10^{\circ}$ in latitude around the equatorial plane, going from 1.6×10^5 cm^{-3} to 0.45×10^5 cm^{-3} at 4.0 $R_{\odot}$ and 6.8 $R_{\odot}$, respectively. Flatter trends characterise the density in the regions outside the streamer, where higher velocity values are observed. Moreover, a most recent analysis, where an improved UV calibration was applied and the Doppler dimming tool was updated to consider a 3D MHD model of the corona, allowed to study in detail the fine structure of the solar wind, analysing in particular the East region. In this case, the solar wind was studied in an angular sector of $\pm 30^{\circ}$ wide in latitude, centered on the equatorial plane. This analysis confirms that the central zone, within about $\pm 10^{\circ}$ in latitude, is denser and is characterised by slower wind, separated from two lateral streams of faster wind, where steep velocity gradients are observed.

In the dense core layer, on the surface that separates opposite magnetic polarities, the denser and slower wind experiences an acceleration higher than in the surrounding layers. At 6.8 $R_{\odot}$ in the core of the streamer belt the wind speed reaches values within 150 km s^{-1} and 190 km s^{-1}, depending on the hypothesis adopted for the H I temperature across the coronal magnetic field lines. The slow wind layer is limited by thin layers where the velocity increases up to 175 km s^{-1} and 230 km s^{-1} in the anisotropic and isotropic H I temperature, respectively, and at 6.8 $R_{\odot}$, forming two faster wind streams at about 15° N and 10° S. These trends were compared with the degree of divergence of the magnetic flux tubes, confirming that a remarkable contribution to the wind acceleration is related to the configuration of the coronal magnetic field, where the re-

gions with high magnetic field lines divergence are anticorrelated with the denser and slower solar wind. Thus, the Metis data show that even in absence of reconnection processes, the densest and slowest features of the coronal wind are formed by the plasma flowing along the current sheet. Furthermore, the hypothesis of the contribution coming from the presence of a S-Web in the acceleration of the slow solar wind has been considered, where photospheric dynamics can stress the separatrix or quasi-separatrix layers, extending within a latitudinal range of $\pm 30^{\circ}$ around the equatorial plane, and can give origin to current sheets and to associated processes of interchange reconnection and coronal plasma release that contribute to the acceleration of the slow wind. It is possible to conclude that the diagnostics techniques applied to VL pB and UV H I Lyα radiation are capable to map the distribution of the solar wind outflow velocity and to relate it to the magnetic field.

The first quadrature between Solar Orbiter and PSP allows, for the first time, the investigation of the same parcel of coronal plasma observed with Metis between 3.5 $R_{\odot}$ and 6.3 $R_{\odot}$ and measured in-situ by PSP at about 22 $R_{\odot}$ on January 17 and 18, 2021, respectively. The electron density and the outflow velocity have been measured in a narrow latitudinal sector at the Eastern equatorial region. The plasma reaches a velocity of about 180 km s^{-1} at 6.3 $R_{\odot}$; the fit performed on the Metis velocity data shows an agreement with the value returned by PSP at 21.4 $R_{\odot}$, equal to 247 km s^{-1}. These values are in agreement with those obtained from the Metis first light analysis, within the uncertainties, confirming the typical values of the slower wind at relatively low heliocentric distances. The electron density values ranges between 4×10^5 cm^{-3} and 4×10^4 cm^{-3} between 3.5 $R_{\odot}$ and 6.3 $R_{\odot}$, respectively. In this case, the fit of the electron density, inferred from Metis pB data, is in agreement with the electron density deduced by PSP measurements, which provided a value of about 2.4×10^3 cm^{-3}. It is worth to note that also these values are in agreement with those obtained when the Metis first light analysis was performed, concerning the denser plasma sheet region. The opportunity offered by this quadrature permits to infer the coronal magnetic field values along the radial direction, starting from the knowledge of the density and velocity provided by Metis observations and considering the density, velocity, and magnetic field measured with PSP, assuming mass and magnetic flux

conservation.

Further interesting results are obtained from the first CME observed with Metis on January 16 and 17, 2021. The high resolution of the acquired images allows to highlight the CME fine structure, identifying the expanding fronts and estimating an expansion velocity of about 140 km s^{-1} for the CME front and about 70 km s^{-1} for the center of the CME. The event was also observed with different instruments. In particular, the data acquired with SOHO/LASCO-C2 and STEREO/COR-2, along with the Metis observations, were considered to analyse the structure of the transient event by applying a GCS 3D model. The complementing of these data with SolO/EUI/FSI observations allowed to identify the source region of the CME, associated with the AR NOAA 12797. Further inspections of STEREO-A/EUVI 30.4 nm images reveal that the source region was located almost exactly in a filament channel East of the AR.

The reported results confirm how the Metis performances, also combined with those of instruments onboard SolO and other spacecraft, can help to give a contribution to understanding how the solar magnetic field regulates the outer solar atmosphere structure, with effects in the evolution of its features and on the onset and acceleration of the outflowing solar wind. They also allow to investigate the acceleration and initial configuration of the transient events, defining the initial conditions. Moreover, they contribute to the investigation of the processes that induce transient events occurrences, with important effects related to the interaction of the Earth magnetosphere with the magnetised plasma coming from the Sun. In particular, Metis allows to investigate the early propagation of these events in the heliosphere, contributing to the development of tools to foresee severe space weather events, which can affect space and ground-based infrastructures, and can be dangerous for anthropic technological activities and even human health and safety.

Bibliography

Abbo, L., Ofman, L., Antiochos, S. K., et al. 2016, Space Sci Rev, 201, 55

Allen, L. A., Habbal, S. R., & Hu, Y. Q. 1998, J. Geophys. Res., 103, 6551

Altschuler, M. D., & Perry, R. M. 1972, Sol. Phys., 23, 4101

Alvarez-Herrero, A., et al., 2015, Proc. SPIE, 9613, 96130I

Andretta, V., Bemporad, A., De Leo, Y., et al. 2021, A&A 656, L14

Antiochos, S. K., Linker, J. A., Lionello, R., et al. 2012, Space Sci. Rev. 172, 169–185

Antonucci, E., Abbo, L., Dodero, M. A. 2005, A&A, 435, 699-711

Antonucci, E., Romoli, M., Andretta, V., et al. 2020, A&A, 642, A10

Antonucci, E., Cooper, D., Capuano, G. E., et al. 2023, Physics of Plasmas, 30, 022905

Artzner, G., Bonnet, R. M., Vial, J. C., et al. 1977, A&A, 3, 131

Auchère, F. 2005, ApJ, 622, 737

Bame, S. J., McComas, D. J., Barraclough, B. L., et al. 1992, A&A Supplement Series, 92, 237

Beckers, J. M., & Chipman, E. 1974, Sol. Phys., 34, 151

Bemporad, A., Matthaeus, W.H., & Poletto, G., 2008, ApJ, 677, L137

Bemporad, A., Pagano, P., & Giordano, S. 2018, A&A, 619, A25

Benkhoff, J., van Casteren, J., Hayakawa, H., et al. 2010, Planet. Space Sci., 58, 2

Bocchialini, K., & Vial, J. C. 1996, Sol. Phys. 168, 37

Boe, B., Habbal, S., Downs, C., et al. 2021, ApJ, 912, 44

Boe, B., Habbal, S., Downs, C., et al. 2022, ApJ, 935, 173

Bonnet, R. M., Lemaire, P., Vial, J. C., et al. 1978, A&A, 221, 1032

Brueckner, G. E., Howard, R. A., Koomen, M. J., et al. 1995, Sol. Phys., 162, 357

Capuano, G. E., Dolei, S., Spadaro, D., et al. 2021, A&A, 652, A85

Cranmer, S. R., Kohl, J. L., Noci, G., et al. 1999b, ApJ, 511, 481

Cranmer, S. R., Panasyuk, A. V., & Kohl, J. L. 2008, ApJ, 678, 1480

Cranmer, S. R. 2020, ApJ, 900, 105

Dere, K. P., Landi, E., Mason, H. E., et al. 1997, A&AS, 125, 149

Dodero, M. A., Antonucci, E., Giordano, S., et al. 1998, Solar Physics, 183, 77-90

Dolei, S., Susino, R., Sasso, C., et al. 2018, A&A, 612, A84

Dolei, S., Spadaro, D., & Ventura, R. 2015, A&A, 577, A34

Dolei, S., Spadaro, D., & Ventura, R. 2016, A&A, 592, A137

Dolei, S., Spadaro, D., Ventura, R., et al. 2019, A&A, 627, A18

Domingo, V., Fleck, B., & Poland, A. I. 1995, Sol. Phys., 162, 1

Dulk, G. A., & McLean, D. J. 1978, SoPh, 57, 279

Fineschi, S., Gardner, L. D., Kohl, J. L., et al. 1998, SPIE Conf. Ser., 3443, 67

Fineschi, S., Naletto, G., Romoli, M., et al. 2020, Exp. Astron., 49, 239

Fontenla, J., Reichmann, E. j., & Tandberg-Hanssen, E. 1988, A&A, 329, 464

Fox, N. J., Velli, M., Bale, S. D., et al. 2016, SSRv, 204, 7

Frazin, R. A., Cranmer, S. R., & Kohl, J. L. 2003, ApJ, 597, 1145

Gabriel, A. H. 1971, Sol. Phys., 21, 392

Gabryl, J.-R., Cugnon, P., & Clette, F. 1999, Solar Wind Nine, AIP Conf. Proc., 471, 749

Gan., W., Deng, Y., Li, H., et al., 2015, Proc. SPIE, 9604, 96040T

Gloeckler, G. et al.: 1992, Astron. Astrophys. Suppl. 92, 267

Gouttebroze, P., Lemaire, P., Vial, J. C., et al. 1978, ApJ, 225, 655

Greisen E. W., Calabretta, M. R. 2002, A&A, 395, 1061

Gunár, S., Schwartz, P., Koza, J., & Heinzel, P. 2020, A&A, *in press*

Gibson, S. E., Fludra, A., Bagenal, F., et al. 1999, J. Geophys. Res., 104, 9691

Gopalswamy, N., Newmark, J., Yashiro, S., et al. 2021, Sol. Phys., 296, 15

Gopalswamy, N., & Yashiro, S. 2011, ApJL, 736, L17

Gradshteyn, I. S., & Ryzhik, I. M. 1996, *Table of Integrals, Series, and Products*. Academic Press, 5th edition

Hapgood, M., & Thomson, A. 2010, *Space weather: its impact on Earth and implications for business.*, Lloyd's 360 Risk Insight

Hayes, A. P., Vourlidas, A., & Howard, R. A. 2001, ApJ, 548, 1081

Howard, R. A., Moses, J. D., Vourlidas, A., et al. 2008, Space Sci. Rev., 136, 67

Hundhausen, A. J. 1972, *Coronal Expansion and Solar Wind*, Springer-Verlag Berlin Heidelberg

Inhester, B. 2015, arXiv:1512.00651

Kasper, J. C., Abiad, R., Austin, G., et al. 2016, SSRv, 204, 131

Ko, Y.-K., Fisk, L. A., Geiss, J., Gloeckler, G., et al. 1997, Sol. Phys., 171, 345

Kohl, J. L, and Withbroe, G. L. 1982, ApJ., 256, 263

Kohl, J. L., Esser, R., Gardner, L. D., et al. 1995, Sol. Phys., 162, 313

Kohl, J.L., Noci, G., Antonucci, E., et al. 1997, Sol. Phys., 175, 613

Kohl, J. L., Noci, G., Antonucci, E., et al. 1998, ApJ, 501, L127

Kohl, J. L., Esser, R., Cranmer, S. R., et al. 1999, ApJL, 510, L59

Kowalska-Leszczynska, I., Bzowski, M., Sokòł, J. M., & Kubiak, A. 2018, ApJ, 852, 115

Lamy, P. L., Quémerais, E., Llebaria, A., et al. 1997, ESA SP-404, 491

Lamy, P., Damé, L., Vivès, S., et al. 2010, Proc. SPIE, 7731, 773118-1

Lamy, P., Llebaria, A., Boclet, B., et al. 2020, Sol. Phys., 295, 89

Lamy, P., Gilardy, H., Llebaria, A., et al. 2021, Sol. Phys., 296, 76

Landi, E., Doron, R., Feldman, et al. 2001, ApJ, 556, 912

Landi, E., Young, P. R., Dere, K. P., et al. 2013, ApJ, 763, 86

Lemaire, P., Choucq-Bruston, M., & Vial, J. -C. 1984, Sol. Phys., 90, 63

Lemaire, P., Emerich, C., Curdt, W., et al. 1998, A&A, 334, 1095

Lemaire, P., Emerich, C., Vial, J. -C., et al. 2002, in From Solar Min to Max: Half a Solar Cycle with SOHO, ed. A. Wilson, Esa SP, 508, 219

Lemaire, P., Vial J.-C., Curdt, W., et al. 2015, A&A, 581, A26

Li, J., Raymond, J. C., Acton, L. W., et al. 1998, ApJ, 506, 431

Mancuso, S. & Bemporad, A., 2009, Advances in Space Research, 44, 451

Mancuso, S., & Garzelli, M. V. 2013, A&A, 553, A100

Marsh, E., Muhlhauser, K.-H., Rosenbauer, H., et al. 1982, J. Geophys. Res., 86, 9199

McComas, D. J., Blame, S. J., Barraclough, B. L., et al. 1998, Geophys. Res. Lett. 25(1), 1

McComas, D. J., Elliot, H. A., Schwadron, N. A., et al. 2003, Geophys. Res. Lett. 30, 1517

McComas, D. J., Ebert, R. W., Elliot, H. A., et al. 2008, Geophys. Res. Lett. 35(18), L18103

Mikić, Z., Downs, C., et al. 2018, Nat. Astron., 2, 913

Miller, M. S., Caruso, A. J., Woodgate, B. E., & Sterk, A. A. 1981, Appl. Opt., 20, 3805

Minnaert, M. 1930, Zs. Ap., 1, 209

Moses, J. D., Antonucci, E., Newmark, J., et al. 2020, NatAs, 4, 1134

Müller, D., Marsden, R. G., St. Cyr, O. C., & Gilbert, H. R. 2013, Sol. Phys., 285, 25

Müller, D., St. Cyr, O., Zouganelis, I., et al. 2020, A&A, 642, A1

Moran, T. G., & Davila, J. M. 2004, Science, 305, 66

Munro, R. H., & Jackson, B. V. 1977, ApJ, 213, 874

Noci, G., Kohl, J. L., & Withbroe, G. L. 1987, ApJ, 315, 706

Ofman, L., Romoli, M., Poletto, G., et al. 1997, ApJ, 491, L111+

Ofman, L., Romoli, M., Poletto, G., et al. 2000, ApJ, 529, 592

Olsen, E. L., Leer, E., & Holzer, T. E. 1994, ApJ, 420, 913

Owen, C. J., Bruno, R., Livi, S., et al. 2020, A&A, 642, A16

Owens, M. J., Forsyth, R. J. 2013, Living Rev. Solar Phys., 10, Issue 1, id. 5

Pagano, P., Bemporad, A., & Mackay, D.H., 2015, A&A, 582, A72

Pagano, P., Bemporad, A., & Mackay, D. H. 2020, A&A, 637, A49

Pätzold, M., Bird, M. K., Volland, H., et al. 1987, SoPh, 109, 91

Parenti, S., Bromage, B. J. I., Poletto, G., et al. 2000, A&A, 363, 800

Parker, E. N. 1958, ApJ, 128, 664-675

Pilipp, W. G., Muehlhaeuser, K.-H., Miggenrieder, H., et al. 1987, J. Geophys. Res., 92, 1075

Poomvises, W., Gopalswamy, N., Yashiro, S., Kwon, R.-Y., & Olmedo, O. 2012, ApJ, 758, 118

Pottasch, S. R. 1964, Space Sei. Rev., 3, 816

Quémerais, E., & Lamy, P. 2002, A&A, 393, 295

Raymond, J. C., Kohl, J. L., Noci, G., et al. 1997, Sol. Phys., 175, 645

Reber, C. A. 1990, EOS, 71, 1867

Renotte, E., Baston, E., Bemporad, A., et al., 2014, Proc. SPIE, 9143, 91432M

Riley, P., Linker, J. A., and Arge, C. N., 2015, Space Weather 13, 154–169

Romoli, M., Antonucci, E., Andretta, V., et al. 2021, A&A, 656, A32

Rottman, G. J., & Woods, T. N. 1994, SPIE, 2266, 317

Rochus, P., Auchère, F., Berghmans, D., et al. 2020, A&A, 642, A8

Saito, K., Makita, M., Nishi, K., et al. 1970, AnTok, 12, 53

Seetha, S. & Megala, S., 2017, Current Science, 113, 4, 610

De Sénarmont, H. 1840, Ann. Chim. Phys. (2), 73, 337

Sheeley, N. R., Wang, Y. M., Hawley, S. H., et al. 1997, ApJ, 484, 472

Schmit, D., Sukhorukov, A. V., De Pontieu, B., et al. 2017, ApJ, 847, 141

Smith, E. 2001, Journal of Geophysical Research, vol. 106, n.A8, 15819

Song, H. Q., Chen, Y., Liu, K., et al 2009, Sol. Phys., 258, 129

Spadaro, D., Susino, R., Dolei, S., et al. 2017, A&A, 603, A35

Spadaro, D., Susino, R., Ventura, R., Vourlidas, A., & Landi, E. 2007, A&A, 475, 707

Susino, R., Ventura, R., Spadaro, D., et al. 2008, A&A, 488, 303

Telloni, D., Bruno, R., Carbone, V., et al. 2009, ApJ, 693, 1022

Telloni, D., Ventura, R., Romano, P., et al., 2013, ApJ, 767, 138

Telloni, D., Antonucci, E., Dolei, S., et al., 2014, A&A, 565, A22

Telloni, D., Andretta, V., Antonucci, E., et al. 2021, ApJL, 920, L14

Telloni, D., Zank, G. P., Stangalini, M., et al., 2022, ApJL, 936, Issue 2, id.L25

Telloni, D., Antonucci, E., L. Adhikari, et al., 2023, A&A, 670, L18

Thernisien, A. F. R., Howard, R. A., & Vourlidas, A. 2006, ApJ, 652, 763

Thernisien, A. F. R. 2011, ApJ, 194, 33

Thompson, W. T. 2006, A&A, 449, 791

Tian, H., Curdt, W., Marsch, E., & Schühle, U. 2009, A&A, 504, 239

Tian, H., Teriaca, L., Curdt, W., & Vial, J. C. 2009, ApJ, 703, L152

Titov, S. V., Hornig, G., & Démoulin, P. 2011, Journal of Geophysical Research (Space Physics) 107, 1164

Titov, S. V., Mikić, Z., Linker, J. A., et al. 2011, ApJ, 731, 111

Van De Hulst, H. C. 1950, Bull. Astron. Inst. Netherland, 410, 135

Viall, N. M., & Vourlidas, A. 2015, ApJ, 807, 176

Wang, Y. M., Sheeley Jr., 1990, ApJ, 355, 726–732

Wang, Y. M., Sheeley Jr., N. R., Walters, J. H., et al. 1998, ApJ, 498, L165-L168

Wilhelm, K., Curdt, W., Marsch, E., et al. 1995, Sol. Phys., 162, 189

Wilhelm, K., Marsch, E., Dwivedi, B. N., et al. 1998, ApJ, 500, 1023

Withbroe, G. L., Kohl, J. L., Weiser, H., & Munro, R. H. 1982, Space Sci. Rev., 33, 17

Woodgate, B. E., Tandberg-Hanssen, E. A., Bruner, E. C., et al. 1980, Sol. Phys, 65, 73

Vasquez, A. M., Van Ballegooijen, A. A., & Raymond, J. C. 2003, ApJ, 598, 1361

Vernazza, J., and Reeves, E. M. 1978, Ap. J. Suppl, 37,485

Verscharen, D., Bale, S. D., & Velli, M. 2021, MNRAS, 506, 4993

Vršnak, B., Magdalenić, J., & Zlobec, P. 2004, A&A, 413, 753

Acknowledgements

I thank Prof. Francesca Zuccarello, Dr. Daniele Spadaro and all the Metis Team for their support during my thesis work and during the last three years as PhD student. They gave me all the tools necessary to develop my research skills, training me deeper in the world of solar physics. I want to thank the Collegio dei Docenti of the PhD course in Physics at the University of Catania for their role in coordinating the students during these years. Finally, I thank the referee, who considered my thesis work and gave their precious judgment.

Appendix A

van de Hulst inversion tool

The following code allows to determine the coronal electron density by applying the Van De Hulst (1950) inversion method to the VL pB data acquired with the SolO/Metis coronagraph or with SOHO/LASCO and STEREO/COR coronagraphs.

```
    pro CID_PB_INVERT_VDH,x,y,coeff,edens,chi2,checkfit,pb_u, $
chi2max=chi2max,debug=debug,verbo=verbo
;-------------------------------------------------------------------------
;               Procedure  CID_PB_INVERT_VDH
;
; Purpose
; Invert pB to Electron Density by van de Hulst (1950) method
;
; Called by
;      CID_PB_INVERT_COMPU
;
; Call
; CID_PB_FITTING
; CID_VDH_GEOM
;
; Input
; x Heliocentric distance array (Rsun)
; y pB array (1/Bsun)
; pb_u=0.63 ; Limb Brightening
```

```
;
; Optional Input
; checkfit ; flag to check fitting goodness
;
; Output
; coeff ; power law radial electron density function coefficients
; eden ; power law radial electron density profile
; chi2 ; chi2
;
; Author:
; L.Zangrilli, S. Giordano, G. E. Capuano
;
; History
;  2021 VDH algorithm implementation by L. Zangrilli
; 2021  robust pB Fitting by S. Giordano, G. E. Capuano
;-------------------------------------------------------------------------

IF ~KEYWORD_SET(chi2max) then chi2max=0.
if ~N_ELEMENTS(checkfit) then checkfit='n'
IF ~KEYWORD_SET(DEBUG)  then debug=''
IF ~KEYWORD_SET(VERBO)  then verbo=''

cconst=3.44e-6

CID_PB_FITTING,x,y,p1,chi2,checkfit,chi2max=chi2max,debug=debug

; Electron density

; geometrical factors
CID_VDH_GEOM,x,geom,u=u

b = fltarr(N_ELEMENTS(p1))
b[1] = p1[1]-1. & b[3] = p1[3]-1.
b[5] = p1[5]-1. & b[7] = p1[7]-1.

b[0] = 1./cconst*1./(sqrt(!dpi)*gamma((-b[1]+1.)/2.)/(2.*gamma(-$
```

```
b[1]/2.+1.)))*p1[0]

b[2] = 1./cconst*1./(sqrt(!dpi)*gamma((-b[3]+1.)/2.)/(2.*gamma(-$
b[3]/2.+1.)))*p1[2]

b[4] = 1./cconst*1./(sqrt(!dpi)*gamma((-b[5]+1.)/2.)/(2.*gamma(-$
b[5]/2.+1.)))*p1[4]

b[6] = 1./cconst*1./(sqrt(!dpi)*gamma((-b[7]+1.)/2.)/(2.*gamma(-$
b[7]/2.+1.)))*p1[6]

; Power Law Radial Density Profile
edens = 1.e8*(b[0]*x^b[1]+b[2]*x^b[3]+b[4]*x^b[5]+b[6]*x^b[7])/geom

; Power Law Radial Density Function Coefficients
coeff=b

end

pro CID_VDH_GEOM,x,geom,u=u
;---------------------------------------------------------------------
; Purpose
; Compute Geometric Factor for van de Hulst
;---------------------------------------------------------------------

IF ~N_ELEMENTS(u) then u=0.63 ; Limb Brightening

omega=asin(1./x)
dueapb=(1.-u)/(1.-1./3.*u)*(2.*(1.-cos(omega)))+ $
u/(1.-1./3.*u)*(1.-cos(omega)^2/sin(omega)*alog((1.+$
 sin(omega))/cos(omega)))

dueamb=(1.-u)/(1.-1./3.*u)*(2./3.*(1.-cos(omega)^3)) $
+u/(1.-1./3.*u)*(1./4.+sin(omega)^2/4.-cos(omega)^4/ $
(4.*sin(omega))*alog((1.+sin(omega))/cos(omega)))
```

```
ag=(dueapb+dueamb)/4. & bg=(dueapb-dueamb)/2.
geom=ag-bg

end

pro CID_PB_FITTING,x,y,p1,chi2,checkfit,chi2max=chi2max,$
debug=debug
;---------------------------------------------------------------------
;Purpose
; Perform the fit on the pB radial profiles
;
; Input
; x ; Heliocentric distance array (Rsun)
; y ; pB array (1/Bsun)
; chi2max             ; max acceptable value of Chi2
;
;
; Output
; p1 ; radial power law function coefficients
; checkfit ; flag to check fitting goodness
; chi2 ; chi2
;
;---------------------------------------------------------------------

IF ~KEYWORD_SET(DEBUG) then debug=''

; Fitting function
ffunc = 'P[0]*x^P[1] + P[2]*x^P[3] + P[4]*x^P[5] + P[6]*x^P[7]'

; Number of parameters of fitting function
nparams = 8 ; number of paraneters of the fitting function
p = fltarr(nparams)

; Structure to force some parameters of fitting function
pi = replicate({fixed:0, limited:[0,0], limits:[0.D,0.D]}, nparams)
```

```
; force amplitudes to > 0.
pi(0).limited(0) = 1 & pi(0).limits(0) = 0.
pi(2).limited(0) = 1 & pi(2).limits(0) = 0.
pi(4).limited(0) = 1 & pi(4).limits(0) = 0.
pi(6).limited(0) = 1 & pi(5).limits(0) = 0.

; force exponents to > -16.
pi(1).limited(0) = 1 & pi(1).limits(0) = -16
pi(3).limited(0) = 1 & pi(3).limits(0) = -16.
pi(4).limited(0) = 1 & pi(5).limits(0) = -16
pi(5).limited(0) = 1 & pi(7).limits(0) = -16

; force exponents to < 0.
pi(1).limited(1) = 1 & pi(1).limits(1) = 0.
pi(3).limited(1) = 1 & pi(3).limits(1) = 0.
pi(5).limited(1) = 1 & pi(5).limits(1) = 0.
pi(7).limited(1) = 1 & pi(7).limits(1) = 0.

ad_factor = 1.e10 ; ad hoc factor to perform fitting

nx = N_ELEMENTS(x)

m_step = 0 ; manual step
a_step = 0 ; automatic step
refit:

; Remove 1st and last element
nxi = 1
nxf = 1
xt = x(nxi:nx-nxf)
yt = y(nxi:nx-nxf)

; Remove 1st element if  1st < 2nd
back0:
if yt(0) lt yt(1) then begin
xt = xt(nxi:*)
```

```
yt = yt(nxi:*)
goto,back0
endif

nxt = N_ELEMENTS(xt)

; Manually Remove some data
if m_step eq 1 then begin
ansr=''
READ,'Would you like to remove more data ? (y(n): ',ansr
if ansr eq 'y' then begin
PRINT,'Number of radial elements: ',STRCOMPRESS(ROUND(N_ELEMENTS(xt)))
READ,' Remove the first: ',nxi
READ,' Remove the last : ',nxl
i0 = nxi
i1 = nxt-1-nxl
xt = xt(i0:i1)
yt = yt(i0:i1)
endif
endif

; Manually Remove some data
if a_step ge 1 then begin
nxi = a_step*5
nxl = a_step*5
i0 = nxi
i1 = nxt-1-nxl
xt = xt(i0:i1)
yt = yt(i0:i1)
endif

yt = yt*ad_factor
ey=SQRT(yt)

; Find last-but-one maximum value (ymx) and its distance (xmx)
ytmp = yt(SORT(yt))
```

```
xtmp = x(SORT(yt))
ymx = ytmp(N_ELEMENTS(ytmp)-2)
xmx = xtmp(N_ELEMENTS(ytmp)-2)

; Perform fitting

; try order 1  ------------------------------------------------
fpower = 1
p[1] = -14. & p[0] = ymx/xmx^p[1]

pi(0).fixed = 0 & pi(2).fixed = 1
pi(4).fixed = 1 & pi(6).fixed = 1

pi(1).fixed = 0 & pi(3).fixed = 1
pi(5).fixed = 1 & pi(7).fixed = 1

if m_step eq 1 then begin
ansp=''
READ,'Change guess paramaters ? (y(n): ',ansp
if ansp eq 'y' then begin
print,'P[1] = ',p[1]
print,'P[0] = ',p[0]/ad_factor
tmp1 = -2
read,' New P[1] = ',tmp1
read,' New P[0] = ',tmp0
p[1] = tmp1 & p[0] = tmp0*ad_factor
endif
endif

P1 = MPFITEXPR(ffunc, xt, yt, ey, P, perror = eP, bestnorm = chi2,$
quiet = 1, PARINFO = pi, STATUS = status, ERRMSG = errmsg)
if status le 0 then MESSAGE,'order 1: '+ errmsg,/INFO
chi2_power1 = chi2
p01 = p1

; try order 2  ------------------------------------------------
```

```
fpower = 2

if N_ELEMENTS(x) le fpower*2+2 then begin
chi2_power2 = chi2_power1*10. & p02 = FLTARR(8)
chi2_power3 = chi2_power1*10. & p03 = FLTARR(8)
chi2_power4 = chi2_power1*10. & p04 = FLTARR(8)
goto,nofit
endif

p[1]=p01[1] & p[0]=p01[0]
p[3]=-8. & p[2]=ymx/xmx^p[3]

pi(0).fixed = 0 & pi(2).fixed = 0
pi(4).fixed = 1 & pi(6).fixed = 1

pi(1).fixed = 0 & pi(3).fixed = 0
pi(5).fixed = 1 & pi(7).fixed = 1

P1=MPFITEXPR(ffunc,xt,yt,ey,P,perror=eP,bestnorm=chi2,quiet=1,$
PARINFO=pi,STATUS=status,ERRMSG=errmsg)
if status LE 0 then MESSAGE,'order 2: '+ errmsg,/INFO
chi2_power2 = chi2
p02 = p1

; try order 3  ------------------------------------------------
fpower = 3
if N_ELEMENTS(x) le fpower*2+2 then begin
chi2_power3 = chi2_power1*10. & p03 = FLTARR(8)
chi2_power4 = chi2_power1*10. & p04 = FLTARR(8)
goto,nofit
endif

p[1] = p02[1] & p[0] = p02[0]
p[3] = p02[3] & p[2] = p02[2]
p[5] = -4.     & p[4] = ymx/xmx^p[5]
```

```
pi(0).fixed = 0     & pi(2).fixed = 0
pi(4).fixed = 0     & pi(6).fixed = 1

pi(1).fixed = 0     & pi(3).fixed = 0
pi(5).fixed = 0     & pi(7).fixed = 1
P1=MPFITEXPR(ffunc,xt,yt,ey,P,perror=eP,bestnorm=chi2,quiet=1,$
PARINFO=pi,STATUS=status,ERRMSG=errmsg)
if status LE 0 then MESSAGE,'order 3: '+ errmsg,/INFO
chi2_power3=chi2
p03=p1

; try order 4  ------------------------------------------------
fpower = 4
if N_ELEMENTS(x) le fpower*2+2 then begin
chi2_power4=chi2_power1*10. & p04=FLTARR(8)
goto,nofit
endif
p[1] = p03[1] & p[0] = p03[0]
p[3] = p03[3] & p[2] = p03[2]
p[5] = p03[5] & p[4] = p03[4]
p[7] = -2.2     & p[6]=ymx/xmx^p[7]

pi(0).fixed = 0     & pi(2).fixed = 0
pi(4).fixed = 0     & pi(6).fixed = 0

pi(1).fixed = 0     & pi(3).fixed = 0
pi(5).fixed = 0     & pi(7).fixed = 0

P1 = MPFITEXPR(ffunc, xt, yt, ey, P, perror = eP,$
bestnorm = chi2, quiet = 1,$
PARINFO = pi, STATUS = status, ERRMSG = errmsg)
if status LE 0 then MESSAGE,'order 4: '+ errmsg,/INFO
chi2_power4=chi2
p04=p1

nofit:
```

```
; Get the best fitting function
all_chi2 = [chi2_power1, chi2_power2, chi2_power3, chi2_power4]
q = MIN(all_chi2,qID)
if N_ELEMENTS(qID) gt 1 then qID = qID(0)
if qID eq 0 then P1=P01
if qID eq 1 then P1=P02
if qID eq 2 then P1=P03
if qID eq 3 then P1=P04

; Repeat fit if Chi2 is large (?)
chi2 = all_chi2(qID)

if chi2max ne 0. then begin
if chi2 ge chi2max then begin
a_step=a_step+1
goto,refit
endif
endif



; Set coefficients
p1[0] = p1[0]/ad_factor
p1[2] = p1[2]/ad_factor
p1[4] = p1[4]/ad_factor
p1[6] = p1[6]/ad_factor

end
```

Appendix B

Doppler dimming tool

The following code allows to determine the H I solar wind outflow velocity by applying the Doppler dimming technique to the H I UV Lyα and to the VL pB data simultaneously acquired with the SolO/Metis coronagraph. The tool also permits to obtain 2D outflow velocity maps through a cycle over the polar angle.

In the case of the SolO-PSP quadrature results reported in Chapter 5, a single radial profile has been used, obtained by averaging the data between $\pm$ 2.5° around 3.8° S at the East limb. Then, in this case the cycle over the polar angle has not to be considered.

```
pro wind,rmin,rmax,rad_samp,los,los_samp,los_angle,angles,anh_file
;---------------------------------------------------------------------
;Procedure  WIND
;
;Purpose:
; Apply the Doppler dimming method to the VL pB and
;H I UV Ly-alpha data to determine the H I solar wind
;outflow velocity
;
;
;
;Input:
;
; rmin ; heliocentric distance corresponding to the inner edge
```

```
; of the FoV (Rsun)
;
; rmax ; heliocentric distance corresponding to the outer edge
; of the FoV (Rsun)
;
; rad_samp ; radial sampling (Rsun)
;
; los ; a half of the range of integration along the line
; of sight (Rsun)
;
; los_samp ; sampling along the LOS (Rsun)
;
; los_angle ; numbers of elements for the lLOS integration
; when the MHD model is considered
;
; angles = 360. ; number of angular sectors in which the FoV is
; subdivided
;
; ne_polar ; electron density on the plane of the sky, or datacube
; if the 3D MHD model returned by the PSI is used (cm^-3)
;
; uv_polar ; observed Ly-alpha intensity on the plane of the sky
; (erg cm^-2 s^-1 sr^-1)
;
; te_polar ; electron temperature on the plane of the sky (K)
;
; thi_polar ; H I temperature on the plane of the sky (K)
;
; anh_file ; filename with the log(ionisation fraction) as a
; function of the log(electron temperature), where the CHIANTI
; database is considered
;
; chrom_int  ;chromospheric intensity (erg cm^-2 s^-1 sr^-1)
;
; anis   ; anisotropy coefficient (anis = 1 means isotropy,
; while anis not equal to 1 means anisotropy. For example, anis>1
```

```
; means that the perpendicular coronal H I temperature is greater
; than the parallel one)
;
;Output:
; v_out ; 2D map of H I solar wind outflow velocity
;
;Author:
; M. Dodero, D. Spadaro, R. Ventura, D. Telloni, S. Dolei,
; S. M. Giordano, G. E. Capuano
;
;History:
; Before 2021: developed by M. Dodero, D. Spadaro, R. Ventura,
; D. Telloni, S. Dolei
; 2021: robust procedures and optimisation by S. M. Giordano, G. E. Capuano
;-------------------------------------------------------------------------

step=los_samp*6.96e+10 ; sampling along the line of sight in cm

; radial array on the plane of the sky
dis=findgen((rmax-rmin)/rad_samp+1)*rad_samp+rmin

; distance from the center of the Sun to the outer edge of the
; FoV at a distance from the plane of the sky equal to los (Rsun)
hmax=sqrt(rmax^2.+los^2.)

; heliocentric distance array outside the plane of the sky,
; with the maximum value equal to hmax
h=findgen((hmax-rmin)/rad_samp+2)*rad_samp+rmin

; fix some constants (cgs units)

;+++++++++++++++++++++++++++++++++++++++++++++++++

plancon = 6.626205e-27 ; Planck constant [dine cm s]

; velocity of the electromagnetic radiation in the vacuum [cm s^-1]
```

```
c = 2.997925e10

amh = 1.67352e-24 ; proton mass [g]

bolcon = 1.380626e-16 ; Boltzmann constant [erg K^-1]

alfal = 1.21567e-05  ; wavelength for Ly-alpha line (cm)

; ratio between protons and electrons (0.83 is returned by
;a percentage of helium equal to 10% of the full ionised plasma)
anpsune = 0.833

; Einstein coefficient B12 in cgs units per Angstrom
b12 = 2.02949e19*((alfal^2.)*1e+08)/c

;+++++++++++++++++++++++++++++++++++++++++++++++++

; number of elements in which the longitudinal angular sector of the
; 3D MHD model is subdivided, across the equator and with a step of
; 0.5 degree, which means ± 60 degrees across the plane of the sky
los_angle = 241

if param eq 'MHD_model' then begin

; numbers of elements for LOS integration when the 3D MHD model
; is considered
los_max=n_elements(los_angle)

semi_los_max = (los_max-1)/2.

else begin

semi_los_max = floor(los/los_samp)

; numbers of elements for LOS integration when the cylindrical
; symmetry is assumed
```

```
los_max = 2.*semi_los_max+1.

endelse

readcol, anh_file, telg, rte, format='(d,d)', /silent, /nan, /quick

;telg --> log(electron temperature)

;rte --> log(ionisation fraction)

; define the synthesised H I Ly-alpha intensity
ilya_polar = fltarr(angles,n_elements(dis))

; define the neutral hydrogen outflow velocity on the plane of
; the sky from the first iterative cycle
v_polar = fltarr(angles,n_elements(dis))

; define the array for the final neutral hydrogen outflow
;velocity on the plane of the sky
v_out = make_array(angles,n_elements(dis),value=!values.f_nan)

; define the neutral hydrogen outflow velocity datacube
v_cube = make_array(angles,n_elements(dis),los_max,value=!values.f_nan)

; define the ionisation fraction datacube
anh = fltarr(angles,n_elements(dis),los_max)

; define the neutral hydrogen temperature datacube
thi = fltarr(angles,n_elements(dis),los_max)

; define the electron temperature datacube
tel = fltarr(angles,n_elements(dis),los_max)

; define the array for the fit over the radial velocity found
; from the first cycle.
v_polar_estes = make_array(angles,n_elements(h),value=!values.f_nan)
```

```
; define the array with the Ly-alpha emissivity along the LOS
elya = fltarr(los_max)

; define the array with the heliocentric distance from the center
; of the Sun to a given distance from the POS
rho = fltarr(los_max)

; define the 2D array with the values of the phi_c angle (see text)
phic = fltarr(n_elements(dis),los_max)

; define the 2D array that will take the values of the arcsin(1/rho).
chi = fltarr(n_elements(dis),los_max)

;if the 3D MHD model has to be used,
;set param = 'MHD_model'. Else, use another string
param = 'MHD_model'

; FIRST ITERATIVE PROCESS: the velocity is initially assumed equal
; to zero in the entire corona

; Cycle over the polar angle. The angular sector defined in the cycle
;can be opportunely modified. In this case, for example, the entire FoV
;is analysed (angles = 360). f = 0 represents the West limb,
;going counterclockwise.
for f = 0, angles-1 do begin

; INTEGRATION OVER THE SOLID ANGLE AND ALONG THE LINE OF SIGHT

;+++++++++++++++++++++++++++++++++++++++++++++++++++++++++++++++++++++

for r = 0,n_elements(dis)-1 do begin ; cycle over the radial direction

cycle = 0
loop1:
```

```
; cycle for the integration of the Ly-alpha emissivity along the LOS
for j = 0,los_max-1 do begin

if param eq 'MHD_model' then rho[r,j] = dis[r]*sqrt(1.+$
tan(-los_angle[j]/!radeg)^2.) else rho[j] = sqrt((dis(r))^2.+$
((j-semi_los_max)*los_samp)^2.)

; series of geometrical parameters
;++++++++++++++++++++++++++++++++
beta = atan((kabs*los_samp)/dis(r))
phic[r,j] = !pi/2.-beta
chi[r,j] = asin(1./rho[j])
;++++++++++++++++++++++++++++++++

if param eq 'MHD_model' then dens=ne_polar[f,r,j] $
else dens=interpol(ne_polar[f,*],h,rho[j])

; determination of the electron temperature datacube
tel[f,r,j] = interpol(te_polar[f,*],h,rho[j])

; determination of the H I density datacube
anh[f,r,j] = dens*10.^interpol(rte,telg,alog10(tel[f,r,j]))

; determination of the H I temperature datacube
thi[f,r,j] = interpol(thi_polar[f,*],h,rho[j])

; array with the values of theta angle, as defined in the text,
; as a function of the heliocentric distance
theta = (findgen(round(chi[r,j]*!radeg)+1))/round(chi[r,j]*!radeg)$
*chi[r,j]

; angular step for theta
hth = chi[r,j]/(n_elements(theta)-1)

; define the array which will contain all the contributes that
; returns the emissivity in a given point
```

```
lya_theta = fltarr(n_elements(theta))


; INTEGRATION OVER THE SOLID ANGLE
for k = 0,n_elements(theta)-1 do begin

; scalar product between the unitary vectors n and n'
nnp2 = (cos(phic[r,j]))^2.*(cos(theta[k]))^2.+$
1./2.*(sin(phic[r,j]))^2.*(sin(theta[k]))^2.

; thermal width of the coronal absorption profile
w = (alfal*1e+08/c)*sqrt(2.*bolcon*thi[f,r,j]/amh)*$
sqrt(1./anis*(cos(theta[k]))^2.+(sin(theta[k]))^2.)

; F function
ddc = (1.878/sqrt(w^2.+0.3075^2.)*exp(-(0.01859+$
alfal*1e+08/c*v_polar[f,r]*cos(theta[k]))^2./(w^2.+0.3075^2.))-$
1.188/sqrt(w^2.+0.2390^2.)*exp(-(0.02087+$
alfal*1e+08/c*v_polar[f,r]*cos(theta[k]))^2./(w^2.+0.2390^2.))+$
0.03102/sqrt(w^2.+0.7353^2.)*exp(-(0.02159+$
alfal*1e+08/c*v_polar[f,r]*cos(theta[k]))^2./(w^2.+$
0.7353^2.)))/(1.878-1.188+0.03102)

lya_theta[k] = b12*anpsune*plancon*chrom_int/(2e+00*!pi*alfal)*$
anh[f,r,j]*((11.+3.*nnp2)/12.)*sin(theta[k])*ddc

if k ge 1 and k le n_elements(theta)-2 then $
lya_theta[k] = lya_theta[k]*(3+(-1)^(k+1))

endfor

; INTEGRATION ALONG THE LINE OF SIGHT

; Cavalieri-Simpson integration
elya[j] = hth/3.*total(lya_theta)
```

```
; 2D map with the synthetic H I UV Ly-alpha intensity all
; over the FoV after the first iterative cycle
if j ne 0 then ilya_polar[f,r] = ilya_polar[f,r]+$
(elya[j]+elya[j-1])/2.*dis[r]*abs(tan(-los_angle[j]/!radeg)-$
tan(-los_angle[j-1]/!radeg))*6.96e+10

endfor

;+++++++++++++++++++++++++++++++++++++++++++++++++++++++++++++

; The observed and synthesised intensity are compared, and the
; velocity values are changed until the synthesised and the
; observed intensities satisfactory match
;+++++++++++++++++++++++++++++++++++++++++++
if ilya_polar[f,r] gt uv_polar[f,r] then begin
v_polar[f,r] = v_polar[f,r]+5e+05
cycle = cycle+1
goto,loop1
endif
;+++++++++++++++++++++++++++++++++++++++++++

; procedure to obtain the fit of the radial velocity on the
; plane of the sky estimated from the first cycle
;+++++++++++++++++++++++++++++++++++++++++++

b = reform(v_polar[f,*])

; function chosen to perform the fit
ffunc = 'P[0]+P[1]*alog(x)^0.5'

; number of parameters of the fitting function
nparams = 2

p0 = dblarr(nparams)

ey = sqrt(b)
```

```
; Structure to force some parameters of fitting function
pii = replicate({fixed:0, limited:[0,0], limits:[0.D,0.D]},nparams)

; force pii(1) to > 0.
pii(1).limited(0) = 1 & pii(1).limits(0) = 0.

P1 = MPFITEXPR(ffunc, dis[qa], b, ey, p0, perror = eP,$
bestnorm = chi2, quiet = 1,$
PARINFO = pii, STATUS = status, ERRMSG = errmsg)

; array with the fit on the estimated radial velocity on the
; plane of the sky
v_polar_estes[f,*] = P1[0]+P1[1]*alog(h)^(0.5)

; estension of the estimated radial velocity by using the fit
v_polar_estes[f,qa] = v_polar[f,qa]

;+++++++++++++++++++++++++++++++++++++++++++++

; building of the velocity datacube from the first cycle,
; assuming coronal cylindrical symmetry
for r = 0,n_elements(dis)-1 do $
v_cube[f,r,*] = interpol(v_polar_estes[f,*],h,rho)
endfor

; SECOND ITERATIVE PROCESS: the initial radial velocity follows
; the found trend, then it assumes increasing values along the
; radial direction and along the LOS. ALL THE PROCEDURES ARE THE
; SAME AS THE AFOREMENTIONED, WHERE v_polar[f,r] IS SUBSTITUTED
; WITH v_cube[f,r,j]

; redefine the synthesised H I Ly-alpha intensity array
ilya_polar = fltarr(angles,n_elements(dis))

for f = 0, angles-1 do begin
```

```
for r = 0,n_elements(dis)-1 do begin

loop2:
for j = 0, los_max-1 do begin

theta = (findgen(round(chi[r,j]*!radeg)+1))/round(chi[r,j]*!radeg)$
*chi[r,j]

hth = chi[r,j]/(n_elements(theta)-1)

lya_theta = fltarr(n_elements(theta))

for k = 0,n_elements(theta)-1 do begin

nnp2 = (cos(phic[r,j]))^2.*(cos(theta[k]))^2.+$
1./2.*(sin(phic[r,j]))^2.*(sin(theta[k]))^2.

w = (alfal*1e+08/c)*sqrt(2.*bolcon*thi[f,r,j]/amh)*$
sqrt(1./anis*(cos(theta[k]))^2.+(sin(theta[k]))^2.)

ddc = (1.878/sqrt(w^2.+0.3075^2.)*exp(-(0.01859+$
alfal*1e+08/c*v_cube[f,r,j]*cos(theta[k]))^2./(w^2.+0.3075^2.))-$
1.188/sqrt(w^2.+0.2390^2.)*exp(-(0.02087+$
alfal*1e+08/c*v_cube[f,r,j]*cos(theta[k]))^2./(w^2.+0.2390^2.))+$
0.03102/sqrt(w^2.+0.7353^2.)*exp(-(0.02159+$
alfal*1e+08/c*v_cube[f,r,j]*cos(theta[k]))^2./(w^2.+$
0.7353^2.)))/(1.878-1.188+0.03102)

lya_theta[k] = b12*anpsune*plancon*chrom_int/(2e+00*!pi*alfal)*$
anh[f,r,j]*((11.+3.*nnp2)/12.)*sin(theta[k])*ddc

if k ge 1 and k le n_elements(theta)-2 then $
lya_theta[k] = lya_theta[k]*(3+(-1)^(k+1))

endfor
```

```
elya[j] = hth/3.*total(lya_theta)

; 2D map with the synthetic H I UV Ly-alpha intensity all over
; the FoV after the second iterative cycle
if j ne 0 then ilya_polar[f,r] = ilya_polar[f,r]+$
(elya[j]+elya[j-1])/2.*dis[r]*abs(tan(-los_angle[j]/!radeg)-$
tan(-los_angle[j-1]/!radeg))*6.96e+10

endfor

; The observed and synthesised intensity are compared again
; after the second iterative cycle, and the velocity values
; are changed until the synthesised and the observed intensities
; satisfactory match
;+++++++++++++++++++++++++++++++++++++++++++
if ilya_polar[f,r] lt uv_polar[f,r] then begin
wh = where(v_cube[f,r,*] ge 5e+05,nw)
if nw ne 0 then v_cube[f,r,wh] = v_cube[f,r,wh]-5e+05
if nw eq los_max then goto,loop2
endif
;+++++++++++++++++++++++++++++++++++++++++++

endfor

; 2D map of H I solar wind outflow velocity
v_out[f,*] = v_cube(f,*,semi_los_max)
endfor

; Save the outflow velocity map
save,filename='velovity_map.sav', v_out
end
```